

**UCLA**

**UCLA Electronic Theses and Dissertations**

**Title**

Electrical Detection of Spin Transport in Silicon Two-Dimensional Electron Gas Systems

**Permalink**

<https://escholarship.org/uc/item/1wv7j796>

**Author**

Chang, Li-Te

**Publication Date**

2015

Peer reviewed|Thesis/dissertation

UNIVERSITY OF CALIFORNIA

Los Angeles

Electrical Detection of Spin Transport in Silicon Two-Dimensional Electron Gas Systems

A dissertation submitted in partial satisfaction of the  
requirements for the degree Doctor of Philosophy  
in Electrical Engineering

by

Li-Te Chang

2015

© Copyright by

Li-Te Chang

2015

## ABSTRACT OF THE DISSERTATION

Electrical Detection of Spin Transport in Si Two-Dimensional Electron Gas Systems

by

Li-Te Chang

Doctor of Philosophy in Electrical Engineering

University of California, Los Angeles, 2015

Professor Kang Lung Wang, Chair

Electrical detection of spin transport in a semiconductor (SC) channel is one of the key requirements to realize spintronics devices.<sup>1</sup> Among various SC materials, the high-mobility two-dimensional electron gas (2DEG) confined in a modulation doped quantum well structure (MODQW) is of particular interest for device applications. This is because the high mobility promises for a long spin diffusion length of coherent transport as well as large spin signal for easy sensing.<sup>2</sup> Meanwhile, the effective spin manipulation is achievable either by enhanced Rashba spin-orbit interaction from an asymmetric  $\mathcal{E}$ -field structure,<sup>3,4</sup> or by direct control of discrete density of states (DOS) within the quantum well structure.<sup>5,6</sup> Despite of these merits, very few studies of direct electrical spin injection into 2DEG have been reported so far, mainly because of the difficulty in making reliable ferromagnetic (FM) contacts to the buried 2DEG channel. In literature, only a few reports in Si/SiO<sub>2</sub><sup>6</sup> and III-V matrices<sup>4,7,8</sup> are available up to



now; however, electrical detection of spin transport in the high-mobility 2DEG in a Si/SiGe MODQW has not been reported. To make continuous progress of Si-based spintronics and to take full advantage of current CMOS technology, there is an urgent need to develop Si-based spintronics devices.<sup>9,10</sup>

In this thesis we present two related projects: first is spin injection in Ge; second is spin injection in Si two-dimensional electron gas (2DEG) system. It is the knowledge built up from the Ge project helps us successfully demonstrate electrical spin injection in Si 2DEG in a Si/SiGe MODQW using FM Mn-germanosilicide ( $\text{Mn}(\text{Si}_{0.7}\text{Ge}_{0.3})_x$ ) end contacts, which is a new approach to circumvent the difficulty of etching process adopted for the typical spin valve devices.<sup>4,8</sup> The experiments show that the spin-polarized electrons could be laterally injected into one side of the 2DEG confined at the Si/SiGe interface, and subsequently detected from the other side by the magnetoresistance (MR) of a FM/2DEG/FM spin valve. Most important of all, symmetric resistance steps were clearly observed from a series of FM/2DEG/FM spin valve devices with different channel lengths ( $L_{ch} = 1.5\sim 3.5 \mu\text{m}$ ), by which the spin diffusion length and spin lifetime are calculated to be  $l_{sf} = 4.5 \mu\text{m}$  and  $\tau_s = 16 \text{ ns}$  at 1.9 K, respectively.

The dissertation of Li-Te Chang is approved

Benjamin S. Williams

Hong-Wen Jiang

Kang Lung Wang, Committee Chair

University of California, Los Angeles

2015

This dissertation is dedicated to my family,  
for their unconditional love, encouragement and support

# TABLE OF CONTENTS

<b>LIST OF FIGURES .....</b>	<b>viii</b>
<b>LIST OF TABLES .....</b>	<b>x</b>
<b>LIST OF SYMBOLS AND ACRONYMS .....</b>	<b>xi</b>
<b>ACKNOWLEDGMENTS .....</b>	<b>xiv</b>
<b>VITA.....</b>	<b>xvi</b>
<b>Chapter 1 Introduction.....</b>	<b>1</b>
1.1 Introduction of Semiconductor Technology and Spintronics .....	1
1.2 Review of Electrical Spin Injection and Detection in Semiconductor.....	3
1.3 Spin Relaxation Mechanisms in Semiconductors .....	8
1.4 Dissertation Outline.....	11
<b>Chapter 2 Experimental Techniques.....</b>	<b>12</b>
2.1 Introduction of Experimental Techniques.....	12
2.2 Material Growth using Molecular Beam Epitaxy .....	13
2.3 Material and Surface Analysis Methods .....	15
2.4 Low Temperature Magneto-Transport Measurements System.....	18
2.5 Electrical Detection of Spin Transport in Semiconductor .....	23
<b>Chapter 3 Electrical Spin Injection and Transport in Ge.....</b>	<b>31</b>
3.1 Introduction of Spin Injection in Ge .....	31

3.2 Electrical Spin Injection in $n$ -Ge Using Fe/MgO/ $n^+$ -Ge Tunnel Contact .....	33
3.3 Electrical Spin Injection in $n$ -Ge Using Mn <sub>5</sub> Ge <sub>3</sub> C <sub>0.8</sub> /Al <sub>2</sub> O <sub>3</sub> Tunnel Contact .....	46
3.4 Limit of the Traditional Approach .....	58
<b>Chapter 4 Electrical Detection of Spin Transport in Si 2DEG Systems .....</b>	<b>60</b>
4.1 Introduction of the Spin Injection into Semiconductor-based 2DEG System .....	60
4.2 MBE Growth of the Sb $\delta$ -doped Si/SiGe MODQW .....	62
4.3 Device Fabrication for the Si/SiGe MODQW .....	68
4.4 Structure Characterization of the Si/SiGe MODQW and Mn(Si <sub>0.7</sub> Ge <sub>0.3</sub> ) <sub>x</sub> .....	73
4.5 Ferromagnetic Property of the Mn(Si <sub>0.7</sub> Ge <sub>0.3</sub> ) <sub>x</sub> .....	77
4.6 Electrical Transport Characterization for the Si/SiGe MODQW Devices.....	80
4.7 Electrical Spin Injection, Transportation, and Detection in the Si 2DEG System.....	85
<b>Chapter 5 Summary.....</b>	<b>93</b>
5.1 Conclusion.....	93
5.2 Outlook.....	94
<b>Appendices .....</b>	<b>96</b>
Appendix A. PPMS System Status Table .....	96
Appendix B. Fe/MgO/ $n^+$ -Ge Device Fabrication Process .....	98
Appendix C. Mn <sub>5</sub> Ge <sub>3</sub> C <sub>0.8</sub> /Al <sub>2</sub> O <sub>3</sub> / $n^+$ -Ge Device Fabrication Process .....	99
Appendix D. Mn(Si <sub>0.7</sub> Ge <sub>0.3</sub> ) <sub>x</sub> Device Fabrication Process .....	100
<b>References .....</b>	<b>103</b>

# LIST OF FIGURES

<b>Figure 1-1.</b> Two-channels circuit model for the FM/SC/FM spin valve device. ....	7
<b>Figure 2-1.</b> Schematic diagram of the SiGe MBE system at IHT. ....	14
<b>Figure 2-2.</b> Schematics of the low temperature magneto-transport measurements system. ....	20
<b>Figure 2-3.</b> The LabVIEW block diagram used to query PPMS information. ....	22
<b>Figure 2-4.</b> Schematic diagrams of the 3T Hanle measurements. ....	26
<b>Figure 2-5.</b> Schematic diagrams of the nonlocal Hanle and nonlocal spin valve measurements. ....	28
<b>Figure 3-1.</b> Electrical spin injection in Ge using Fe/MgO/ $n^+$ -Ge tunneling contact. ....	36
<b>Figure 3-2.</b> Spin lifetime as a function of bias voltage in the modulation-doped $n$ -Ge at 10 K. ....	39
<b>Figure 3-3.</b> Spin lifetime as a function of temperature in the $n$ -Ge. ....	45
<b>Figure 3-4.</b> $\text{Mn}_5\text{Ge}_3\text{C}_{0.8}$ device structure and contact properties. ....	48
<b>Figure 3-5.</b> Structure characterization of the $\text{Mn}_5\text{Ge}_3\text{C}_{0.8}/\text{Al}_2\text{O}_3/n^+$ -Ge contact. ....	50
<b>Figure 3-6.</b> 3T Hanle and inverted Hanle effect measurements at 4 K. ....	56
<b>Figure 3-7.</b> Temperature-dependent Hanle effect measurements and extracted spin lifetime. ....	57
<b>Figure 4-1.</b> Material developments for the Sb $\delta$ -doped Si/SiGe MODQW on Si (111) ....	65
<b>Figure 4-2.</b> Hall mobilities as a function of temperature for the six samples A4051-A4200. ....	67
<b>Figure 4-3.</b> Schematics of the Si/SiGe MODQW device structure and the contact process. ....	70
<b>Figure 4-4.</b> Effects of (100) and (111) crystal orientation on the contact properties. ....	71
<b>Figure 4-5.</b> Structure characterization of Si/SiGe MODQW and $\text{Mn}(\text{Si}_{0.7}\text{Ge}_{0.3})_x$ . ....	75
<b>Figure 4-6.</b> Anomalous Hall effect measurements of a single $\text{Mn}(\text{Si}_{0.7}\text{Ge}_{0.3})_x$ contact. ....	78
<b>Figure 4-7.</b> TLM and Hall measurements of the Si/SiGe MODQW. ....	84

<b>Figure 4-8.</b> Nonlocal and local FM/2DEG/FM spin valve measurements.....	87
<b>Figure 4-9.</b> Energy band diagrams of the FM/2DEG/FM spin valve with (a) nonlocal and (b) four-terminal setups.....	88
<b>Figure 4-10.</b> MR curves of the FM/2DEG/FM spin valves. ....	91
<b>Figure 4-11.</b> The spin-dependent resistance as a function of channel length at 1.9 K.....	92
<b>Figure 5-1.</b> Proposal of Si 2DEG-based spin logic device.....	95

# LIST OF TABLES

<b>Table 1-1.</b> Spin-orbit splitting energy for different semiconductors <sup>36,37</sup> .....	10
<b>Table 2-1.</b> Summary of material and surface analysis techniques <sup>38,39</sup> .....	16
<b>Table 2-2.</b> List of instruments and the related functions .....	21
<b>Table 2-3.</b> Summary of electrical detection techniques for spin transport in semiconductors.....	29
<b>Table 4-1.</b> Substrate temperature during MBE growth for the Sb $\delta$ -doped Si/SiGe MODQW ...	66



# LIST OF SYMBOLS AND ACRONYMS

1D/2D/3D	One-/Two-/Three-Dimensional
2DEG	Two-Dimensional Electron Gas
3-T/4-T	Three-/Four-Terminal
AES	Auger Electron Spectroscopy
AFM	Atomic Force Microscopy
AHE	Anomalous Hall Effect
ALD	Atomic Layer Deposition
AMR	Anisotropy Magnetoresistance
CMOS	Complementary Metal-Oxide-Semiconductor
DMS	Diluted Magnetic Semiconductor
EBL	Electron-Beam Lithography
EDAX	Energy dispersive analysis
EDS	Energy-Dispersive Spectrum
FCC	Face-Centered Cubic
FET	Field-Effect Transistor

FFT	Fast Fourier Transform
FIB	Focused-Ion Beam
FinFET	Fin Field Effect Transistor
FM	Ferromagnet/Ferromagnetic metal
FTIR	Fourier Transform Infrared Spectroscopy
HF	Hydrofluoric Acid
HRTEM	High-Resolution Transmission Electron Microscopy
HRS	High Resistance State
ITRS	International Road Map for Semiconductors
IPA	Isopropyl Alcohol
LPCVD	Low-Pressure Chemical Vapor Deposition
LRS	Low Resistance State
MBE	Molecular Beam Epitaxy
MOSFET	Metal-Oxide-Semiconductor Field-Effect Transistor
MR	Magnetoresistance
MTJ	Magnetic Tunnel Junction
PMMA	Polymethyl Methacrylate

PPMS	Physical Property Measurement System
RA	Resistance-Area
Raman	Raman Vibrational Spectroscopy
REED	Reflection High Energy Electron Diffraction
RBS	Rutherford Backscattering Spectroscopy
RTA	Rapid Thermal Anneal
SC	Semiconductor
SEM	Scanning Electron Microscopy
SIMS	Secondary Ion Mass Spectrometry
SOI	Spin Orbit Interaction
SpinFET	Spin Field-Effect-Transistor
STM	Scanning Tunneling Microscopy
$T_c$	Curie Temperature
TEM	Transmission Electron Microscopy
XPS	X-ray Photoelectron Spectroscopy

# ACKNOWLEDGMENTS

It has been six years since I joined DRL. I have received numerous help from many people here to make this project possible. I would like to first thank my supervisor, Professor Kang L. Wang, for his guidance and support in both academic and daily life, for leading me into this research topic of spintronics, for guiding me to overcome difficulties, for challenging me to continuously improve myself, and for inspiring me to be a worldwide researcher by personal example.

I would also like to acknowledge Professor Robert N. Candler, Professor Benjamin S. Williams, and Professor Hong-Wen Jiang for serving as my doctoral committee members and giving me insightful comments and advices that greatly help me improve my work.

I am deeply thankful to my outstanding collaborators for their indispensable support and contribution to my research work. In particular, I acknowledge Professor Jörg Schulze's group (Inga Anita Fischer, Michael Oehme) for high quality MBE material growth, Professor Lih-Juann Chen's group (Chiu-Yen Wang) for substantial TEM analysis, Professor Roland K. Kawakami's group (Wei Han, Patrick M. Odenthal) for Fe/MgO/ $n^+$ -Ge tunnel junction growth.

It's been my honor to work with many talented colleagues in DRL and UCLA. In particular, I have been working very closely with Jianshi Tang and Yi Zhou, who have helped me tremendously in every aspect of my research work, including fabrication process, device measurements, data analysis, and manuscript writing. Also, I enjoy the inspiring discussion and collaboration with the MBE/TI group (Faxian Xiu, Liang He, Tianxia Nei, Yabin Fan, Murong Lang, Xufeng Kou, Xiaowei Jiang, Koichi Murata, and Siguang Ma), carbon group (Minsheng

Wang, Caifu Zeng, Mei Xue, Carlos Torres, and Aryan Navabi), and many other colleagues including Wangjun Jiang, Guoqiang Yu, Pramey Upadhyaya, Yung-Chen Lin, Yu Chen, Wan-Ching Hsu. I also own my gratitude to a brilliant undergraduate student, Jodi Loo, who I have tutored, for her great help in the Ge project.

I acknowledge the technical support from the clean room staffs (Joe Zendejas, Hoc Ngo, Huynh Do, Wilson Lin, Max Ho, Brain Matthew, Tom Lee, and Steve Franz) in UCLA Nanoelectronics Research Facility. I also acknowledge Ignacio Martini and Adam Stieg in the California NanoSystem Institute for their thorough training and assistance. I also thank Professor Yong Chen for granting me access to the e-beam writer.

Last but not least, I would like to express my deepest love and special gratitude to my family for their unconditional love, encouragement, and support.

# VITA

## Education

- 2011-2015 **Graduate Student Researcher in Electrical Engineering**  
University of California, Los Angeles, USA
- 2009-2011 **M.S. in Electrical Engineering**  
University of California, Los Angeles, USA
- 2004-2008 **B.S. in Electrophysics**  
National Chiao Tung University, Hsinchu, Taiwan ROC

## Selected Publications

- F. Xiu, L. He, Y. Wang, L. Cheng, **L.-T. Chang**, M. Lang, G. Huang, X. Kou, Y. Zhou, X. Jiang, Z. Chen, J. Zou, A. Shailos, and K. L. Wang, “Manipulating surface states in topological insulator nanoribbons,” *Nat Nano*, 6, 216 (2011)
- Y. Zhou, W. Han, **L.-T. Chang**, F. Xiu, M. Wang, M. Oehme, I. A. Fischer, J. Schulze, R. K. Kawakami, and K. L. Wang, “Electrical spin injection and transport in germanium,” *Physical Review B*, 84, 125323 (2011)
- L.-T. Chang**, W. Han, Y. Zhou, J. Tang, I. A. Fischer, M. Oehme, J. Schulze, R. K. Kawakami, and K. L. Wang, “Comparison of spin lifetimes in  $n$ -Ge characterized between three-terminal and four-terminal nonlocal Hanle measurements,” *Semiconductor Science and Technology*, 28, 015018 (2013)
- I. A. Fischer, J. Gebauer, E. Rolseth, P. Winkel, **L.-T. Chang**, K. L. Wang, C. Sürgers, and J. Schulze, “Ferromagnetic  $Mn_5Ge_3C_{0.8}$  contacts on Ge: work function and specific contact resistivity,” *Semiconductor Science and Technology*, 28, 125002 (2013)
- W. Jiang, P. Upadhyaya, Y. Fan, J. Zhao, M. Wang, **L.-T. Chang**, M. Lang, K. L. Wong, M. Lewis, Y.-T. Lin, J. Tang, S. Cherepov, X. Zhou, Y. Tserkovnyak, R. N. Schwartz, and K. L. Wang, “Direct Imaging of Thermally Driven Domain Wall Motion in Magnetic Insulators,” *Physical Review Letters*, 110, 177202 (2013)

J. Tang, C.-Y. Wang, **L.-T. Chang**, Y. Fan, T. Nie, M. Chan, W. Jiang, Y.-T. Chen, H.-J. Yang, H.-Y. Tuan, L.-J. Chen, and K. L. Wang, “Electrical Spin Injection and Detection in  $\text{Mn}_5\text{Ge}_3/\text{Ge}/\text{Mn}_5\text{Ge}_3$  Nanowire Transistors,” *Nano Letters*, 13, 4036 (2013)

**L.-T. Chang**, C.-Y. Wang, J. Tang, T. Nie, W. Jiang, C.-P. Chu, S. Arafin, L. He, M. Afsal, L.-J. Chen, and K. L. Wang, “Electric-Field Control of Ferromagnetism in Mn-Doped ZnO Nanowires,” *Nano Letters*, 14, 1823 (2014)

Y. Fan, P. Upadhyaya, X. Kou, M. Lang, S. Takei, Z. Wang, J. Tang, L. He, **L.-T. Chang**, M. Montazeri, G. Yu, W. Jiang, T. Nie, R. N. Schwartz, Y. Tserkovnyak, and K. L. Wang, “Magnetization switching through giant spin-orbit torque in a magnetically doped topological insulator heterostructure,” *Nat Mater*, 13, 699 (2014)

I. A. Fischer<sup>//</sup>, **L.-T. Chang**<sup>//</sup>, C. Sürgers, E. Rolseth, S. Reiter, S. Stefanov, S. Chiussi, J. Tang, K. L. Wang, and J. Schulze, “Hanle-effect measurements of spin injection from  $\text{Mn}_5\text{Ge}_3\text{C}_{0.8}/\text{Al}_2\text{O}_3$ -contacts into degenerately doped Ge channels on Si,” *Applied Physics Letters*, 105, 222408 (2014)

J. Tang, **L.-T. Chang**, X. Kou, K. Murata, E. S. Choi, M. Lang, Y. Fan, Y. Jiang, M. Montazeri, W. Jiang, Y. Wang, L. He, and K. L. Wang, “Electrical Detection of Spin-Polarized Surface States Conduction in  $(\text{Bi}_{0.53}\text{Sb}_{0.47})_2\text{Te}_3$  Topological Insulator,” *Nano Letters*, 14, 5423 (2014)

G. Yu, P. Upadhyaya, Y. Fan, J. G. Alzate, W. Jiang, K. L. Wong, S. Takei, S. A. Bender, **L.-T. Chang**, Y. Jiang, M. Lang, J. Tang, Y. Wang, Y. Tserkovnyak, P. K. Amiri, and K. L. Wang, “Switching of perpendicular magnetization by spin-orbit torques in the absence of external magnetic fields,” *Nat Nano*, 9, 548 (2014)

### Conference Presentations

**L.-T. Chang**, K. L. Wang, “Electrical Spin Injection and Transport in Germanium”, *INC8*, Tsukuba, Japan, 2012

I. A. Fischer, **L. -T. Chang**, C. Sürgers, S. Chiussi, K. L. Wang, and J. Schulze, “Spin Accumulation in n-Ge on Si with Sputtered  $\text{Mn}_5\text{Ge}_3\text{C}_{0.8}$ -Contacts”, *ISTDM*, Singapore, 2014

**L.-T. Chang**, K. L. Wang, “Electrical Detection of Spin Transport in Si Two-Dimensional Electron Gas Systems”, *INC11*, Fukuoka, Japan, 2015

# Chapter 1 Introduction

## 1.1 Introduction of Semiconductor Technology and Spintronics

This project was motivated by critical challenges facing the continuous scaling of CMOS technology. In 1965 Dr. Gordon Moore published the article, *Cramming more components into integrated circuits*,<sup>11</sup> on *Electronics Magazine*, predicting that the number of transistors on a single chip will increase by twice as much every two years. This became known as the famous Moore's Law, followed by the entire semiconductor industry as a development guideline for tens of years. Early on, the scaling of transistors was driven by the improvements of photolithography. Recently, the scaling relied on the implementation of new materials, such as strained silicon,<sup>12,13</sup> high- $\kappa$  dielectric,<sup>14,15</sup> and metal gate.<sup>13</sup> Strained silicon provided improvements in mobility and current-drive that electrons could transport 70 % faster comparing to normal silicon;<sup>12</sup> high- $\kappa$  dielectric and metal gates increased the device performance without the associated problem of leakage current.<sup>14</sup> More recently, while the scaling approached to 20 nm, power consumption resulting from leakage current became a major problem.

To further scale the transistor dimension as well as power consumption, the state-of-art solution is to change to an innovative devices structure, *i.e.* tri-gate transistors or multiple gate transistors, which is a variation of FinFET<sup>16,17</sup> with a fully depleted channel. By replacing the traditional planar transistor structure with a three-dimensional (3D) channel, the gate electrode



pinches the fin-shape channel on two sides and on top, so that the transistor could be turned off effectively even at sub-20 nm dimension. For the past 50 years, the semiconductor industries have worked out many creative solutions to pursue Moore's Law. For the next decade, the performance scaling will likely be not only at transistor level, but also at interconnect and 3D architecture.

The 2013 International Technology Roadmap of Semiconductors (ITRS)<sup>18</sup> highlights key challenging needs as the increase in functionality, the decrease in power dissipation, and low manufacturing variability. In addition to the physical scaling that follows the Moore's Law, ITRS proposed a new trend called "More-than-Moore", aiming to increase the devices values by integrating more functionalities that do not necessarily scale according to the Moore's Law. Different functionalities could be integrated on the same chip to cover a wide range of applications, such as MEMS, analog circuit, high power driver, biochips, and spintronics.

Among the various applications, spintronics utilize electron spins as new degrees of freedom for information process. It is noted that the memory device<sup>19</sup> is currently the most successful spintronics application that could beat the CMOS technology. Because digital information is stored as magnetization orientation, it enables the creation of novel electronic devices with ultrahigh density (4-8 area in  $F^2$ ), low power consumption ( $< 10$  fJ/bit), and nonvolatile storage.<sup>19</sup> In addition to the memory devices, another interesting application is spin field-effect-transistors (spinFETs) that exploit the spin-dependent transport of charge carriers. In specifically, electrical detection of spin transport in semiconductor channel is the first requirement to realize spinFETs. Therefore, we present a systematic study towards electrical detection of spin transport in Si two-dimensional electron gas (2DEG) in this dissertation.

## 1.2 Review of Electrical Spin Injection and Detection in Semiconductor

Prior work on spintronics devices has shown that when current flows through a ferromagnetic (FM) metal into an ordinary metal, electrons preserve their spin polarization and transport into the ordinary metal,<sup>20-23</sup> because the density-of-states (DOS) at Fermi level is spin-asymmetric in the FM metal. This concept resulted in the first proposal of spin field-effect-transistors (SpinFETs) by Datta and Das<sup>3</sup> in 1990. It also aroused people's interests in the topic of electrical detection and manipulation of spin transport in semiconductor channel over the last two decades.

In 1985, Johnson and Silsbee<sup>20-22</sup> was the first to experimentally report the electrical spin injection into paramagnetic metal films. The spin polarization in a non-ferromagnetic metal was recognized by the Hanle effect, which also allows the determination of spin lifetime. Though the device operation yielded only a small change of output voltage due to its all-metal construction, these works introduced a refreshing idea at that time to generate spin polarization in a non-ferromagnetic metal. In 1990, Datta and Das<sup>3</sup> proposed an impressive device structure to electrically inject spin-polarized electrons into a high-mobility two-dimensional electron gas (2DEG) channel confined at InGaAs/InAlAs interface, and more importantly to modulate the spin polarization using a gate voltage through the Rashba effect. This idea was experimentally demonstrated by Koo<sup>4</sup> in 2009. Although we have known that the Datta-Das type SpinFET has the similar problem of power consumption as CMOS structure because the spin transport is still associated with the charge transport, this proposal has triggered lots of research efforts in electrical spin injection and detection in GaAs,<sup>24,25</sup> Si,<sup>26-29</sup> and Ge.<sup>30-32</sup>

Comparing to non-ferromagnetic metal, it is more challenging for electrical spin injection and detection into a diffusive semiconductor, because the impedance mismatch between ferromagnetic metal and semiconductor prohibits spin injection in the diffusive transport regime.<sup>33,34</sup> The problem could be explained using a two-channels circuit model (see **Figure 1-1**). The typical device consists of a semiconductor (SC) channel layer sandwiched by two ferromagnetic metal (FM) layers, in which the FM layers exhibit a spin-dependent conductivity and the SC layer carries equal parts of spin-up and spin-down electrons. If we neglect the spin-flip process between the two channels, the device could be simplified as a two-channel parallel circuit: one is for majority spin, the other is for minority spin. In the absence of spin scattering, the resistances of the two spin channels in one FM could be formulated as:<sup>33</sup>

$$R_{FM}^{\uparrow} = \frac{2R_{FM}}{1-\beta} \quad \text{and} \quad R_{FM}^{\downarrow} = \frac{2R_{FM}}{1+\beta} \quad (1-1)$$

where  $\beta = (\sigma^{\uparrow} - \sigma^{\downarrow}) / (\sigma^{\uparrow} + \sigma^{\downarrow})$  is the spin polarization defined by spin dependent conductivities  $\sigma^{\uparrow\downarrow}$ . To further simplify the model for a qualitative analysis, we assume the two spin channels in SM are equal ( $R_{SC}^{\uparrow} = R_{SC}^{\downarrow} = 2R_{SC}$ ), and we have either  $R_{FM1}^{\uparrow} = R_{FM2}^{\uparrow}$  and  $R_{FM1}^{\downarrow} = R_{FM2}^{\downarrow}$  for parallel magnetization configuration, or  $R_{FM1}^{\uparrow} = R_{FM2}^{\downarrow}$  and  $R_{FM1}^{\downarrow} = R_{FM2}^{\uparrow}$  for antiparallel magnetization. As a result, the change in resistance between the parallel and antiparallel magnetization configuration could be calculated as:<sup>33</sup>

$$TMR \equiv \frac{R_{AP} - R_P}{R_P} = \frac{\beta^2}{1-\beta^2} \frac{R_{FM}^2}{R_{SC}^2} \frac{4}{4 \frac{R_{FM}^2}{R_{SC}^2} + 2 \frac{R_{FM}}{R_{SC}} + (1-\beta^2)} \quad (1-2)$$

It is important to notice that the TMR is proportional to  $(R_{FM}/R_{SC})^2$ , and  $R_{FM}/R_{SC}$  is typically of the order of  $10^{-4}$  or smaller (*e.g.*  $\rho_{Ge} = 1 \Omega \cdot \text{m}$ , and  $\rho_{Fe} = 0.1 \mu\Omega \cdot \text{m}$ ). Therefore, the AMR of a typical SC/FM/SC spin valve is too small to detect; in other words, the magnetoresistance (MR) is independent on the magnetization of the FM layers, but is dominated by the spin-independent SC layer.

For the past decades, the common solution to increase the TMR ratio is to insert a tunnel oxide or to build a sharp Schottky barrier between the FM and SC layers.<sup>2,34</sup> There are two milestones in the experimental demonstrations of electrical spin injection and detection in semiconductor thin film. In 2007, Lou<sup>25</sup> demonstrated electrical detection of spin transport in GaAs using a sharp Fe/GaAs Schottky contact. He showed a series of nonlocal spin valve and nonlocal Hanle measurements, which provide detailed quantitative information about spin injection and transport in these Fe/GaAs devices. Two years later, in 2009, Dash<sup>28</sup> demonstrated electrical creation of spin polarization in Si at room temperature, in which the three-terminals Hanle curves were observed in Si up to 300 K. Although the trustworthiness of three-terminals Hanle measurements is always under discussion<sup>35</sup> that the measured Hanle curves might result from the suspicious signal of FM contact, this work indeed aroused people's attention in spintronics application in room temperature.

In addition to these milestones, our group also has major contributions to the area of electrical spin injection and detection in semiconductor. Zhou<sup>30</sup> demonstrated first spin injection in Ge in 2011. I was involved in this work by building up a data acquisition system for low temperature magneto-transport measurements. In 2014, we continued the Ge work and replaced the traditional FM metal (*i.e.* Fe) with  $\text{Mn}_5\text{Ge}_3\text{C}_{0.8}$ ,<sup>32</sup> which can be grown epitaxially on Ge

(111) to effectively avoid the formation of interface defects and hence improve the spin injection/detection efficiency. Finally, I would like to highlight the work of electrical detection of spin transport in Si two-dimensional electron gas (2DEG) system. This is the project that I independently lead for the last three years. We demonstrated electrical spin injection and transport in the 2DEG using FM/2DEG/FM structure, particularly for the first time in a Si/SiGe MODQW system. Being different from the traditional approaches, we developed high-quality  $\text{Mn}(\text{Si}_{0.7}\text{Ge}_{0.3})_x$  end contact to the buried 2DEG in a Si/SiGe MODQW using CMOS-compatible processes. In addition, we extracted the spin diffusion length and lifetime  $l_{sf} = 4.5 \mu\text{m}$  and  $\tau_s = 16 \text{ ns}$  at 1.9 K, respectively. Our findings in the Si/SiGe MODQW may spur further work on semiconductor-based heterostructures that integrate high-mobility channel with magnetic contacts, and may potentially lead to the innovation of novel spintronics devices.

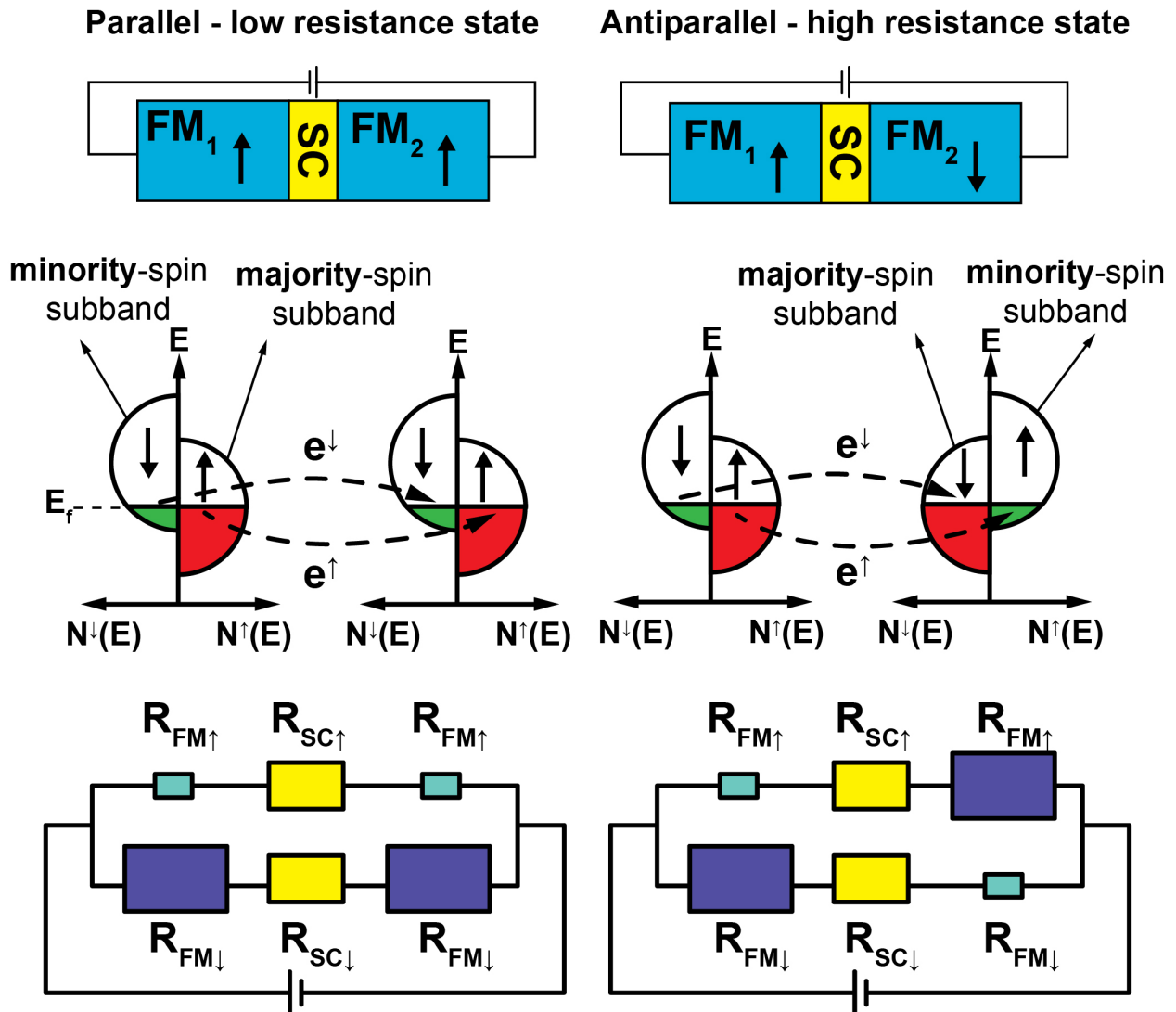


**Figure 1-1.** Two-channels circuit model for the FM/SC/FM spin valve device. (Upper) The FM/SC/FM spin valve devices under parallel and antiparallel magnetic configuration. (Middle) Schematic illustration of electron tunneling in FM/SC/FM tunnel junction. Dashed lines depict the spin-conserved tunneling. (Lower) Schematic circuit diagram of the two-channel model. The actual sizes of the resistors were chosen to indicate the higher and lower resistances of the spin-up and spin-down channels, respectively.

### 1.3 Spin Relaxation Mechanisms in Semiconductors

There are four spin relaxation mechanisms of conduction electrons for semiconductors: Elliott-Yafet, D'yakonov-Perel', Bir-Aronov-Pikus, and hyperfine-interaction mechanism.<sup>1</sup> The Elliott-Yafet mechanism explains spin relaxation in solids possessing center of symmetry (e.g. Si, Ge), in which the Bloch function of electron wave is an admixture of the opposite spin states due to spin-orbit coupling (SOC) induced by ions:

$$\begin{aligned}\Psi_{\bar{k}\uparrow}(\bar{r}) &= \left[ a_{\bar{k}}(\bar{r})|\uparrow\rangle + b_{\bar{k}}(\bar{r})|\downarrow\rangle \right] \cdot e^{i\bar{k}\cdot\bar{r}} \\ \Psi_{\bar{k}\downarrow}(\bar{r}) &= \left[ a_{-\bar{k}}^*(\bar{r})|\uparrow\rangle - b_{-\bar{k}}^*(\bar{r})|\downarrow\rangle \right] \cdot e^{i\bar{k}\cdot\bar{r}}\end{aligned}\tag{1-3}$$

where  $|\uparrow\rangle$  and  $|\downarrow\rangle$  are the Pauli spin-up and spin-down states,  $a_{\bar{k}}(\bar{r})$  and  $b_{\bar{k}}(\bar{r})$  are the complex lattice-periodic coefficients on the radius vector  $\bar{r}$ . Thus every scattering event has chance to cause spin flip process, and the spin relaxation is closely related to the momentum relaxation. On the contrary, the D'yakonov-Perel' mechanism is for the solids without center of symmetry (e.g. GaAs). Spin dephasing occurs because the itinerary electrons feel an effective magnetic field resulting from the lack of inversion and SOC:

$$H(\bar{k}) = \frac{1}{2} \hbar \sigma \cdot \bar{\Omega}(\bar{k})\tag{1-4}$$

where  $\sigma$  are the Pauli matrices,  $\bar{\Omega}(\bar{k})$  represents electron precession with Larmor frequency. This field changes to a random direction once the electron scatters to a different momentum states. The Bir-Aronov-Pikus mechanism is related to  $p$ -doped semiconductors that the electron-hole exchange interaction causes a fluctuating local magnetic field and electron spin flipping.

Last, the hyperfine interaction dominates the semiconductor heterostructures with a nuclear magnetic moment, such as modulation doped quantum well structure (MDQWS).

In particular for Elliot-Yafet mechanism that is dominant in Si and Ge, the relation between spin relaxation time and momentum relaxation time in non-degenerate semiconductors could be expressed as:<sup>1</sup>

$$\frac{1}{\tau_s(E_k)} = A \left( \frac{\Delta_{so}}{E_g + \Delta_{so}} \right)^2 \left( \frac{E_k}{E_g} \right)^2 \frac{1}{\tau_p(E_k)} \quad (1-4)$$

where  $\tau_p(E_k)$  is the momentum scattering at energy  $E_k$ ,  $\Delta_{so}$  is the spin-orbit splitting of the valence band (see **Table 1-1**), and  $E_g$  is the energy gap. The numerical factor  $A$  depends on the dominant scattering mechanism. For the temperature dependence of spin relaxation time, the thermal averaging leads to a substitution of thermal energy  $k_B T$  for  $E_k$ , which leads to  $1/\tau_s(T) \propto T^2/\tau_p(T)$ . If the momentum scattering is dominated by ionized impurity scattering ( $\tau_p \propto T^{3/2}$ ) at low temperature, the temperature dependence could be simplified as:

$$\frac{1}{\tau_s(T)} \propto \frac{T^2}{\tau_p(T)} \propto T^{1/2} \quad (1-5)$$

For degenerate semiconductor, such as heavily-doped Ge, the temperature dependence of  $1/\tau_s$  is directly proportional to  $1/\tau_p$  because  $E_k = E_F$ . The temperature dependence follows:<sup>30</sup>

$$\frac{1}{\tau_s(T)} \propto \frac{1}{\tau_p(T)} = \frac{\lambda_1}{\tau_L} + \frac{\lambda_2}{\tau_I} = \lambda_1 T^{1.64} + \lambda_2 T^{-1.2} \quad (1-6)$$

where  $1/\tau_L \propto T^{1.64}$  and  $1/\tau_I \propto T^{-1.2}$  are phonon scattering rate and ionized impurity scattering rate, respectively, and  $\lambda_1$  and  $\lambda_2$  are two fitting coefficients.



**Table 1-1.** Spin-orbit splitting energy for different semiconductors<sup>36,37</sup>

<b>Semiconductors</b>	<b>Energy gap (eV)</b>	<b>Spin-orbit splitting energy (eV)</b>
<b>Si</b>	1.12	0.044
<b>Ge</b>	0.66	0.29
<b>GaAs</b>	1.53	0.35
<b>InAs</b>	0.43	0.41
<b>InSb</b>	0.23	0.82
<b>InP</b>	1.41	0.14
<b>GaP</b>	2.4	0.094

## 1.4 Dissertation Outline

This dissertation will be organized into two related projects: first is spin injection in Ge; second is spin injection in Si two-dimensional electron gas (2DEG) system. It is the knowledge built up from the Ge project help us successful demonstrate electrical spin injection in Si 2DEG. In Chapter 2, we will first describe the experimental techniques used in these projects, including a brief introduction of material growth using molecular beam epitaxy (MBE), a summary of material and surface analysis methods, a setup of low temperature magneto-transport measurements system, and a summary of electrical detection techniques for spin transport in semiconductors. In Chapter 3, we will demonstrate electrical spin injection and detection into Ge using Fe/MgO/ $n^+$ -Ge and  $\text{Mn}_5\text{Ge}_3\text{C}_{0.8}/\text{Al}_2\text{O}_3/n^+$ -Ge tunnel contact. In these studies, we present the contact engineering for spin injection into Ge thin film. However, we also show you the limitation of the traditional approach for the semiconductor thin film system. In Chapter 4, we will present a comprehensive development process of spin injection into Si 2DEG system, including material growth, structure analysis, device fabrication, and device characterization. The successful of Si 2DEG system might provide a breakthrough in the semiconductor thin film system. Finally, a brief discussion and conclusion will be given in Chapter 5, followed by an outlook of future work.

# Chapter 2 Experimental Techniques

## 2.1 Introduction of Experimental Techniques

Electrical spin injection and detection in semiconductor is an interesting topic in the scope of spintronics. It takes tremendous efforts in material growth, device fabrication, device characterization, and physics analysis. In this chapter, I will describe the experimental techniques used in this project, including material growth by Molecular Beam Epitaxy (MBE), various material and surface analysis techniques, low-temperature magneto-transport measurements, and electrical detection of spin transport in semiconductor.

The starting materials used in these experiments are modulation-doped Ge structures and Sb  $\delta$ -doped Si/SiGe modulation doped quantum well structures. These materials are grown by Professor Jörg Schulze's group in the Institut für Halbleitertechnik (IHT), Universität Stuttgart. Except for MBE growth, I carried out the device design, fabrication, and characterization. In particular, the spin injection and detection experiments were done at low temperature (1.9 to 100 K) with a low-temperature magneto-transport measurements system that we built up at Device Research Laboratory under the supervision of Professor Kang L. Wang. I will describe the system integration with a LabVIEW data acquisition program. Finally, I summarize the electrical detection techniques for spin transport in semiconductor.

## 2.2 Material Growth using Molecular Beam Epitaxy

The MBE system at IHT is from the company ATOMIKA. It consists of a transfer system, a loading chamber, and a growth chamber (see **Figure 2-1**). The system allows the epitaxial growth on a 150 mm diameter substrate or a 100 mm diameter substrates in a carrier ring. For this MBE system, two major growth materials are Silicon (Si) and Germanium (Ge) that are evaporated from the electron beam evaporator. Two doping sources are antimony (Sb) and boron (B) that are evaporated from the effusion cells. It is noted that Sb is the group VI materials, so it provides additional electrons as *n*-type doping; on the contrary, B is the group III materials, so it provides additional holes as *p*-type doping in the group IV materials (Si and Ge). During the growth, substrate is heated up by a graphite filament, and it is electrically grounded to avoid accumulated charges and associated damage due to accelerated Si and Ge atoms.

To preserve a high-quality and consistent material growth, the *in-situ* analyses are provided by a pyrometer and two quadrupole mass spectrometers (QMS). The pyrometer monitors the substrate's temperature in the range of 550 ~ 1010 °C, and the QMS monitors the vacuum in the growth chamber as well as check the Si and Ge flux. Meanwhile, it is a programmable control system from Eurotherm (FICS 10A) to control substrate temperature, effusion cell temperature, and Si and Ge flux. All the growth parameters and material sequence design are setup before the growth, as shown in **Table 4-1**. This procedure allows a better persistence and reproducibility of the material growth, because the subjective influence from the operator could be prevented during the growth.

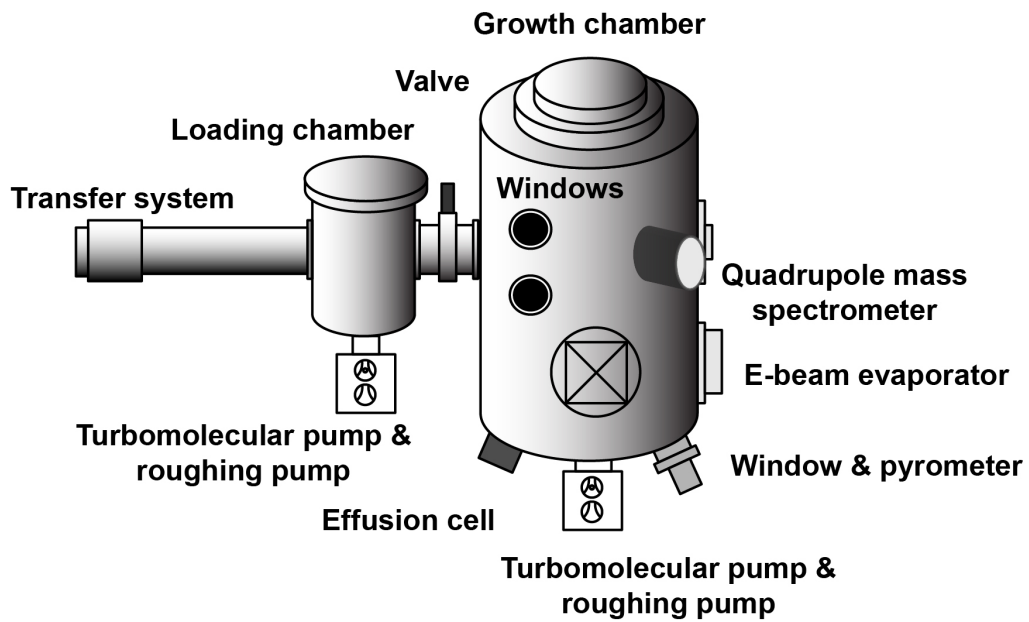


**Figure 2-1.** Schematic diagram of the SiGe MBE system at IHT. (Upper) Picture of the SiGe MBE system at IHT. (Lower) Schematic diagram of the transfer system, loading chamber, and growth chamber.

## 2.3 Material and Surface Analysis Methods

**Table 2-1** is a summary of surface analysis methods that used for material and device developments. The table is first organized by the basic mechanism (incident excitation, and emitted response), followed by the main purpose (type of information) and the technical specification (detection limit, lateral resolution, and depth resolution). For example, scanning electron microscopy (SEM) provides magnified surface image. Its working mechanism is to scan material surface with a focused *electron* beam, and reproduce the surface image based on the reflected secondary *electron*, which contains surface information such as the conductivity contrast and surface topography. Therefore, in **Table 2-1**, the incident excitation of SEM is *electron*; the emitted response is also *electron*; the lateral resolution is about 1 nm. On the other hand, X-ray photoelectron spectroscopy (XPS) provides the analysis of elemental composition. Its working mechanism is to shine an X-ray (photons) onto the sample, and detect the excited photoelectrons, whose energy is proportional to the elemental binding energy. The spectrum of the photoelectrons provides the elemental composition of the material surface. In this case, the incident excitation of XPS is *photon (X-ray)*; the emitted response is *electron*; the detection limit is  $10^{19}$ - $10^{20}$  atoms/cm<sup>3</sup>; the lateral resolution is 10-1000  $\mu\text{m}$ ; the depth resolution is 2 nm. It is noted XPS could also provide the depth profile with the help of plasma etching.

**Table 2-1.** Summary of material and surface analysis techniques<sup>38,39</sup>

Techniques	Incident Excitation	Emitted Response	Type of Information*	Detection Limit** (atm./cm <sup>3</sup> )	Lateral Resolution	Depth Resolution
<b>AES</b>						
Auger electron spectroscopy	electron	electron	elem/chem	10 <sup>19</sup> -10 <sup>20</sup>	100 μm	2 nm
<b>SEM</b>						
Scanning electron microscopy	electron	electron	surface image	-	1 nm	-
<b>TEM</b>						
Transmission electron microscopy	electron	electron	surface image & crystal struct.	-	sub-nm	-
<b>RHEED</b>						
Reflection high energy electron diffraction	electron	electron	crystal struct.	-	0.1-1000 μm	2 nm
<b>EDAX</b>						
Energy dispersive analysis of X-ray	electron	photon (X-ray)	elem	10 <sup>19</sup> -10 <sup>20</sup>	1 μm	1 μm
<b>SIMS</b>						
secondary ion mass spectrometry	ion	ion	elem	10 <sup>14</sup> -10 <sup>18</sup>	1 μm	1-30 nm

<b>RBS</b>						
Rutherford backscattering spectroscopy	ion	ion	elem	$10^{19}$ - $10^{20}$	0.1 cm	20 nm
<b>XPS</b>						
X-ray photoelectron spectroscopy	photon (X-ray)	electron	elem/chem	$10^{19}$ - $10^{20}$	10-1000 $\mu\text{m}$	2 nm
<b>Raman</b>						
Raman vibrational spectroscopy	photon (X-ray)	photon (X-ray)	molecule	$10^{19}$	1 $\mu\text{m}$	1–10 $\mu\text{m}$
<b>STM</b>						
Scanning tunneling microscopy	$\mathcal{E}$ -field	electron	surface roughness	-	0.1 nm	0.01 nm
<b>AFM</b>						
Atomic force microscopy	$\mathcal{E}$ -field	electron	surface roughness	-	30 nm	0.1 nm

\*elem: elemental composition, chem: chemical composition; \*\*Detection limit depends on element to be detected.



## 2.4 Low Temperature Magneto-Transport Measurements System

Low-temperature magneto-transport measurements are the major characterization used to study the physics of spin transportation in 2DEG. This system consists of a cryostat, various external instruments, and a LabVIEW data acquisition program (see **Figure 2-2**). The experiment could be carried out at the base temperature 1.9 K and the largest magnetic field of  $\pm 9$  Tesla. The sample is mounted at the bottom of the cryostat, and connected to the external electronics instruments that are controlled by a LabVIEW data acquisition program. Because this program integrates the cryostat and all of the external instruments, it could modulate all the parameters in one setup, such as the source-drain bias voltage, gate bias voltage, temperature, and magnetic field. Most importantly, this system is able to perform continuous magneto-transport measurements. Once setup, the LabVIEW program collects data day and night, hence it takes full advantage of liquid helium and time.

The left part of **Figure 2-2** is a commercial cryostat called Physical Property Measurement System (PPMS) from Quantum Design. It provides a fast access of low temperature (1.9 K) and high magnetic field ( $\pm 9$  Tesla). The sample cooling is achieved by pumping the liquid helium into the PPMS probe through an impedance tube at the probe-end. In this way, the sample temperature could be controlled accurately *via* adjusting the helium flow rate in the impedance tube. In addition, by passing a large current ( $\sim 8.6$  A at 1 Tesla) through the superconducting magnet that merges inside the liquid helium, a large magnetic field could be created at the sample space. Furthermore, while a superconductor switch bypasses the magnet current into a

closed superconducting loop, the magnet could be operated in the “persistent” mode to minimize helium consumption.

In experiments, the sample is mounted at bottom of the PPMS probe with an accurate-controlled temperature and magnetic field. The sample wirings are extended upwards to the probe head, where a hand-made interface box collects all the wiring and serves as a connection bridge to various external instruments (center part of **Figure 2-2**), in which the typical functions of each instrument are summarized in **Table 2-2**. Finally, every instrument and computer are interconnected by GPIB cables, and all parameter could be collected by a LabVIEW data acquisition program (right part of **Figure 2-2**). For example, **Figure 2-3** shows a LabVIEW block diagram to query PPMS information, in which every command is built by a graphic and connected by a wire to form a sequence. It provides a user-friendly interface between computer and external instruments. The program remotely controls the instruments via the GPIB (IEEE-488) interfaces, so that it could simultaneously send commands to each one and link them together. With the help of data acquisition program and flexible connection, it is easy to perform innovative design of magneto-transport measurements.

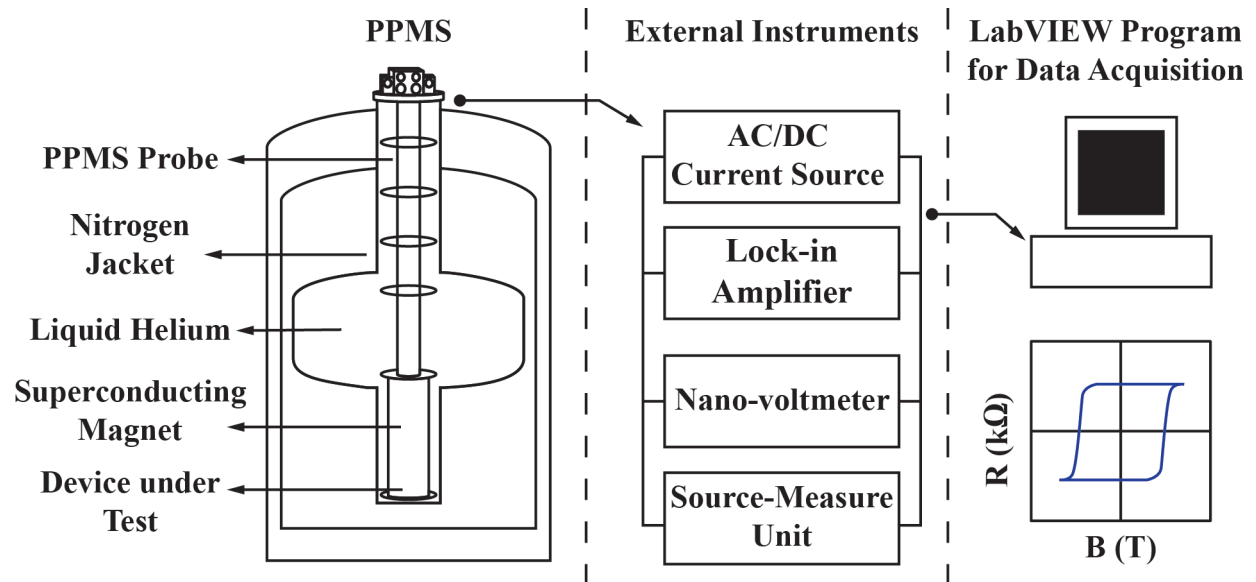


**Figure 2-2.** Schematics of the low temperature magneto-transport measurements system. The sample is loaded at the bottom of the PPMS probe (left). The sample wirings are extended upwards to the probe-head, where a hand-made interface box collects all the wiring and serves as a connection bridge to various external instruments (center) for magneto-transport measurements. The PPMS and external instruments are integrated together by a LabVIEW program (right) for data acquisition.

**Table 2-2.** List of instruments and the related functions

<b>Company</b>	<b>Model</b>	<b>Function</b>
<b>Quantum Design</b>	QD 6000	Temperature and field control system
<b>Keithley</b>	KE 6221	AC/DC current source
<b>Keithley</b>	KE 2182	Nano-voltmeter
<b>Keithley</b>	KE 2636	Source measure unit
<b>Stanford Research Systems</b>	SR 830	Lock-in preamplifier
<b>Stanford Research Systems</b>	SR 560	Voltage preamplifier
<b>Stanford Research Systems</b>	SR 570	Current preamplifier

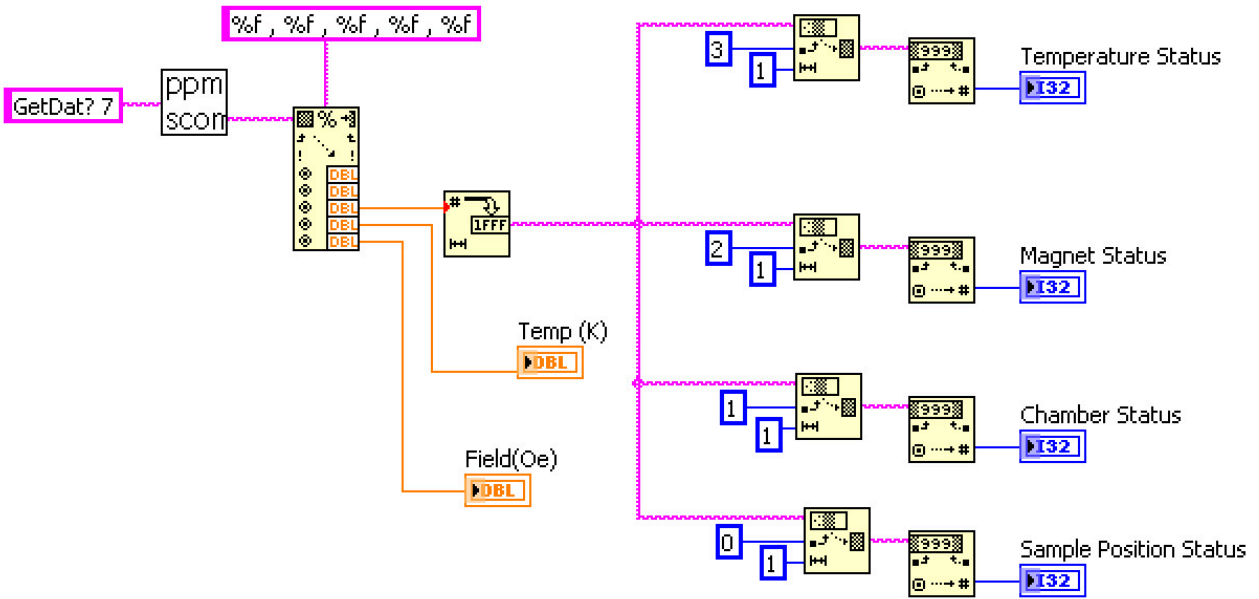


**Figure 2-3.** The LabVIEW block diagram used to query PPMS information. This block diagram is based on a basic driver, “ppmscomm.dll”, provide by Quantum Design.<sup>40</sup> It serves as a GPIB communication interface between the PPMS and computer. To query the PPMS information, the GPIB command is *Getdat\$ 7*, and the returned information would be in the format of *7, x, x, x, x*. The first number corresponds to the *Getdat* number; the second number corresponds to the time stamp; the third number corresponds to the PPMS status; the forth number corresponds to the temperature; the fifth number corresponds to the field. For the third number, once converted to the format of Hexadecimal, **Appendix A** shows the status table for the status of temperature, magnet, chamber, and sample position, respectively.

## 2.5 Electrical Detection of Spin Transport in Semiconductor

Electrical spin injection and detection in semiconductor is one of the essential requirements to realize functional spintronics devices. In this section, I will use spin injection in Ge as examples and review different approaches of electrical spin detection, including three-terminal (3T) Hanle, 3T inverted Hanle, four-terminal (4T) nonlocal Hanle, and 4T nonlocal spin valve measurements. In the end, **Table 2-3** is a summary of the electrical detection techniques for spin transport in semiconductor channel.

For electrical methods, 3T and 4T nonlocal schemes are two major approaches used to study spin transport. The advantages of 3T Hanle techniques include the simplicity of both device fabrication and the ability to extract spin lifetime. However, since the same contact is used for both spin injection and detection, care must be taken to distinguish the desired signals attributed to the spin injection and transport in the semiconductor from anomalous signals due to anisotropic magnetoresistance (AMR),<sup>41</sup> surface roughness,<sup>42</sup> or localized states at the interface.<sup>43</sup> On the other hand, 4T nonlocal techniques show that the nonlocal voltage signal depends on the relative magnetization orientations of the injector and detector.<sup>25,27,30</sup> It is conventionally used to avoid the above-mentioned spurious signal<sup>41-43</sup> because the charge current is separated from the spin diffusion path into the detector terminal. However, the spacing between the injector and detector has to be comparable to the spin diffusion length, which is usually in the range of sub-micron meters.

**Figure 2-4(a)** shows the typical schematics of the 3T device structure and the circuit setup of 3T Hanle measurements. **Figure 2-4(b)** shows an energy band diagram of the active contact

under reverse bias, in which spin accumulation ( $\mu^\uparrow > \mu^\downarrow$ ) is generated in Ge channel by passing currents through a Fe/MgO/ $n^+$ -Ge tunnel contact. The spin polarization voltage ( $V_{3T}$ ) is linearly proportional to the spin accumulation given by  $\Delta V = \Delta\mu \times \gamma / 2e$ , where  $\gamma$  is the tunneling spin polarization of the contact, and  $\Delta\mu = \mu^\uparrow - \mu^\downarrow$  is the difference between the electrochemical potentials of spin-up and spin-down electrons. To detect spin accumulation using Hanle effect, the spin polarization voltage could be de-polarized by applying a transverse magnetic field ( $B_z$ ), which induces spin precession around the magnetic field direction at the Larmor frequency<sup>20,28</sup> ( $\omega_L = g\mu_B B_z / \hbar$ , where  $g = 1.6$  is the Landé  $g$ -factor for Ge,  $\mu_B$  is the Bohr magneton, and  $\hbar$  is the reduced Planck constant). As a result, the 3T Hanle voltage could be modeled by a Lorentzian function:<sup>28</sup>

$$\Delta V_{3T}(B) = \Delta V_{3T, B=0} / \left[ 1 + (\omega_L \tau_s)^2 \right] \quad (2-1)$$

It is important to noted that spin lifetime could be extracted when Hanle voltage reduces to the half of the maximum value:

$$\Delta V_{3T}(B_{1/2}) = \frac{1}{2} \cdot \Delta V_{3T, B=0} \quad (2-2)$$

$$\omega_L = 1/\tau_s = (g\mu_B B_{1/2}) / \hbar \quad (2-3)$$

$$\tau_s = \hbar / (g\mu_B B_{1/2}) \quad (2-4)$$

As shown in **Figure 2-4(c)**, the 3T Hanle curve at 4 K is well fitted by **Equation 2-1**. In particular, the extracted spin lifetime  $\tau_s$  at 4 K is 900 ps.

The 3T Hanle curve indicates a dephase process of spin polarization while spin-polarized electrons precess at the Larmor<sup>28</sup> frequency around a transvers ( $B_z$ ) magnetic field. On the contrary, the 3T inverted Hanle effect is an opposite process that spin polarization is increased by an in-plane magnetic field ( $B_y$ ). The appearance of the 3T inverted Hanle effect is a consequence of spatially inhomogeneous magnetostatic stray field that arises from the finite roughness at the FM/oxide interface. The stray fields cause intrinsic spin precession near the interface, so the spin polarization is suppressed even without an external field. By sweeping an in-plan magnetic field ( $B_y$ ), the injected electron spins could be re-aligned towards the easy-axis of the FM contact, and the spin polarization finally saturates at a large field ( $\sim 1$  Tesla).<sup>42</sup> Consequently, the coexistence of 3T Hanle and 3T inverted Hanle curves are currently regarded as a strong evidence of spin accumulation in semiconductor channel.



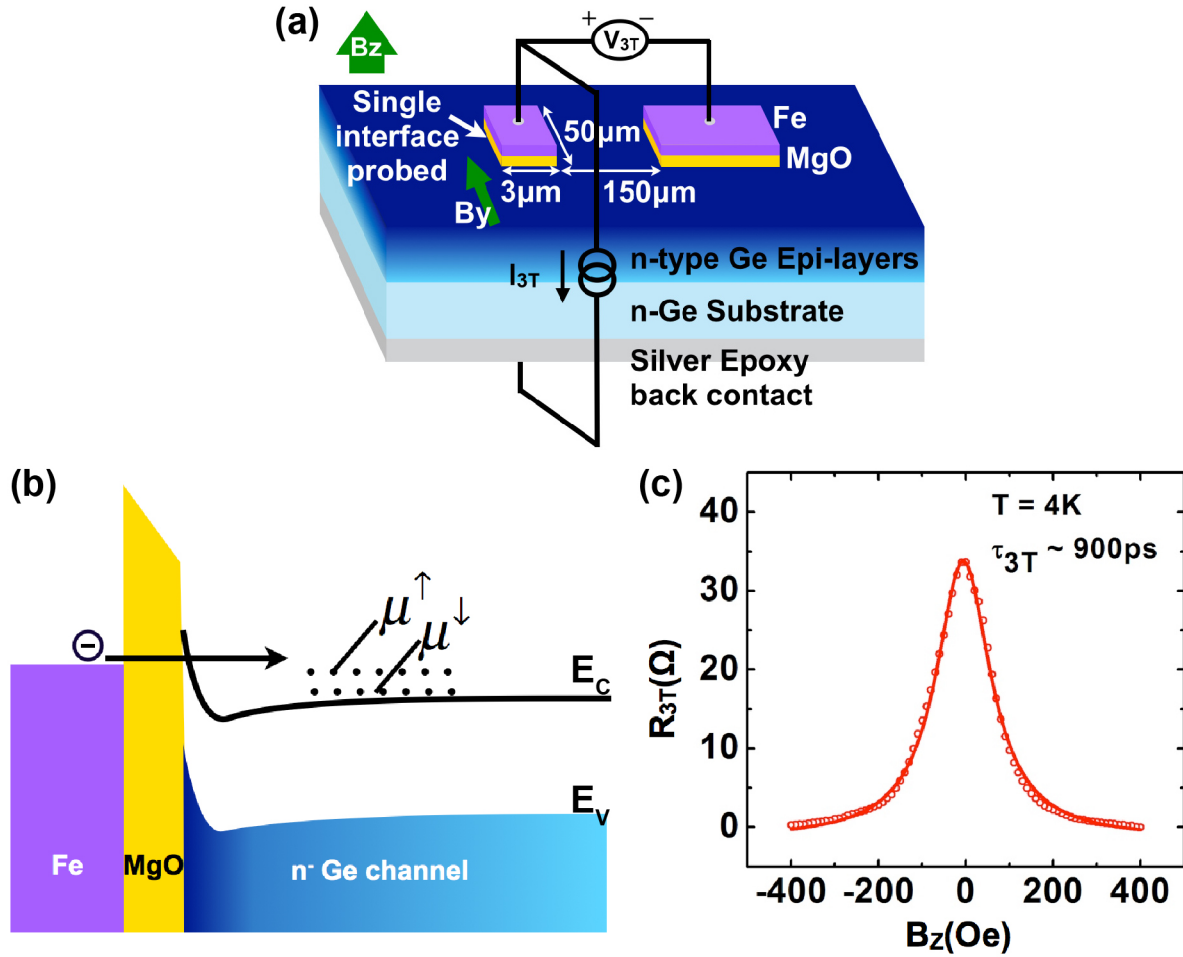


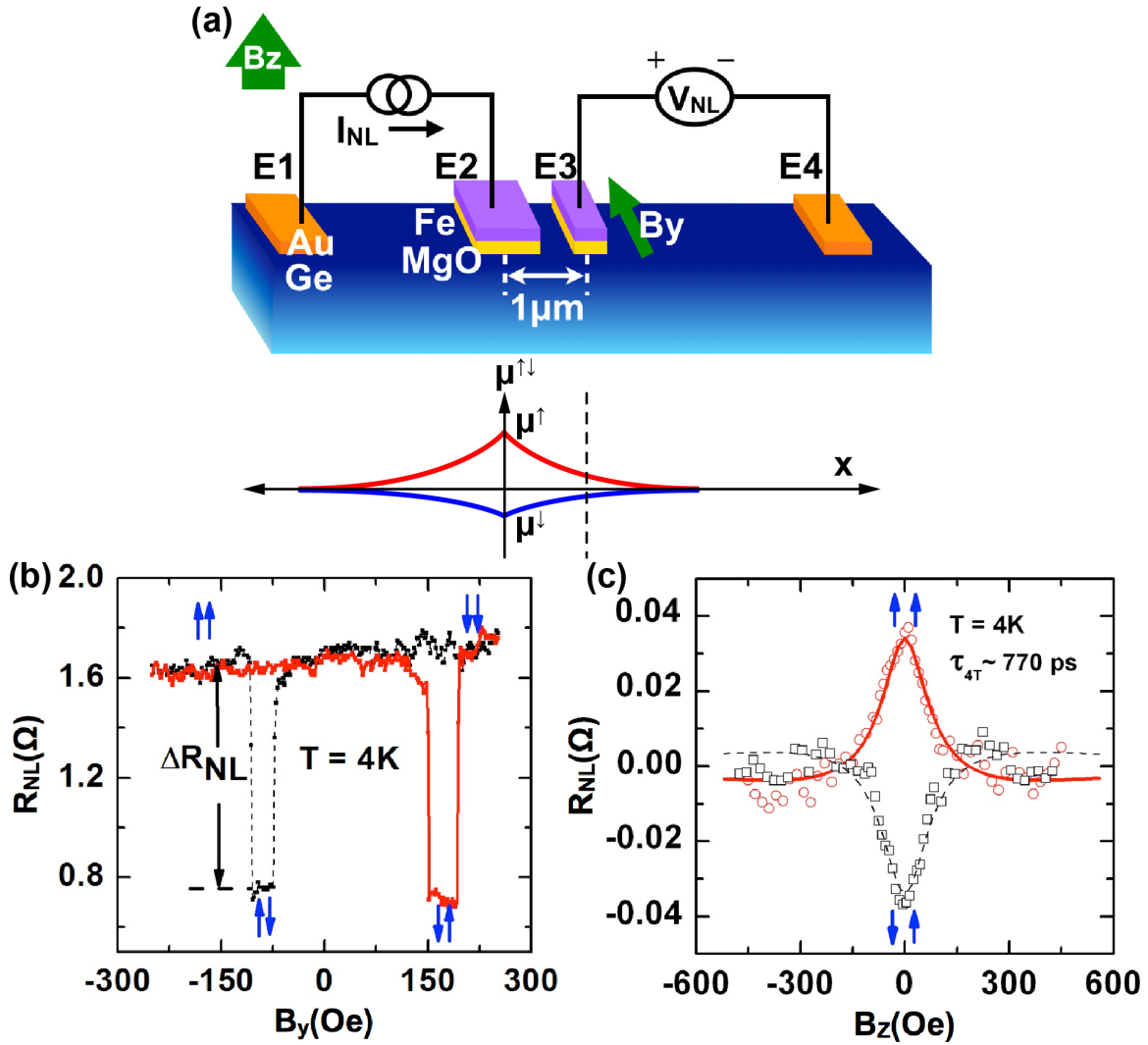
**Figure 2-4.** Schematic diagrams of the 3T Hanle measurements. (a) Schematics of the 3T device structure and the measurements scheme. The size of the active contact is  $3 \times 50 \mu\text{m}^2$ . (b) Energy band profile of the active contact under reverse bias at 4 K. (c) The MR curve of 3T Hanle measurements at 4 K, in which the Lorentzian fitting provides a spin lifetime of  $\tau_{3T} = 900 \text{ ps}$ .

**Figure 2-5(a)** is a schematic diagram of the 4T device structure and the nonlocal measurements scheme. The energy band diagram of the spin injector (E2) is similar to that of **Figure 2-4(b)**. Once applying a reverse bias voltage (current) on the spin injector, the spin-polarized electrons are vertically injected into the Ge channel, and laterally diffuse toward outside non-FM electrode (E1) and spin detector (E3) due to the gradient of spin-dependent electrochemical potentials, as shown in the lower inset of **Figure 2-5(a)**. As a result, the spin detector measures a nonlocal voltage ( $V_{NL}$ ) that is proportional to the projection of the spin accumulation in the Ge channel onto its magnetization direction; furthermore,  $V_{NL}$  changes sign when the magnetization orientations of spin injector and detector switch from parallel to antiparallel configurations. **Figure 2-5(b)** shows 4T nonlocal spin valve measurements at 4T while sweeping field along the in-plane direction ( $B_y$ ), where the nonlocal resistance ( $R_{NL}$ ) is defined as the nonlocal voltage ( $V_{NL}$ ) divided by the AC modulation current ( $I_{AC}$ ), and the blue arrows indicate the magnetization orientation of the injector and detector.

**Figure 2-5(c)** shows 4T nonlocal Hanle measurements at 4 K, in which a small transverse field ( $B_z$ ) is applied to induce the spin precession by the Hanle effect.<sup>20,28</sup> The solid (dashed) lines were fitting based on the one-dimensional (1-D) spin drift-diffusion model:<sup>30</sup>

$$V_{NL} \propto \pm \int_0^{\infty} \frac{1}{\sqrt{4\pi Dt}} \exp\left[-\frac{L^2}{4Dt}\right] \cos(\omega_L t) \exp\left(-\frac{t}{\tau_s}\right) dt \quad (2-5)$$

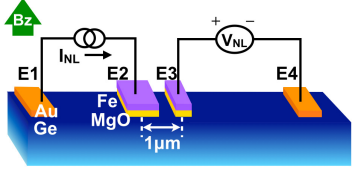
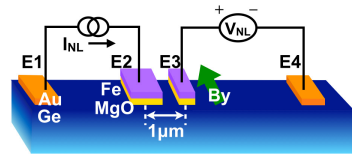
In the above equation, + (-) sign is for the parallel (antiparallel) magnetization configuration,  $D$  is the diffusion constant,  $\omega_L$  is the Larmor frequency as defined above. A spin lifetime of 770 ps at 4 K was extracted by fitting the data with **Equation 2-5**.



**Figure 2-5.** Schematic diagrams of the nonlocal Hanle and nonlocal spin valve measurements. (a) Schematics of the device structure and the nonlocal measurements scheme. The lower inset shows the lateral distribution of spin-dependent electrochemical potential. (b) MR curves of the nonlocal spin valve measurements at 4 K with a DC bias current of  $-20\ \mu\text{A}$  and an AC modulation current of  $-10\ \mu\text{A}$ . (c) MR curves of the nonlocal Hanle measurements at 4 K with a DC injection current of  $-130\ \mu\text{A}$ . The extracted spin lifetime is  $\tau_{4T} = 770\text{ ps}$ . For both curves, the blue arrows indicate the magnetization orientation of E2 and E3.

**Table 2-3.** Summary of electrical detection techniques for spin transport in semiconductors

Setup	Local	
	3T Hanle	3T inverted Hanle
Schematics		
Spin injection	<ul style="list-style-type: none"> <li>Spin accumulation (<math>\Delta\mu = \mu^\uparrow - \mu^\downarrow</math>) in SC channel is built under the spin injector by passing a current through a FM tunnel contact.</li> </ul>	
Spin detection	<ul style="list-style-type: none"> <li>Spin polarization voltage is proportional to the spin accumulation as:                     <math display="block">\Delta V_{3T} = \Delta\mu \times \gamma / 2e</math> </li> </ul>	
	<ul style="list-style-type: none"> <li>Apply transverse field (<math>B_z</math>) to induce spin precession and spin dephasing (Hanle effect).</li> <li>Extract spin lifetime using Lorentzian fitting.</li> </ul> $\Delta V_{3T}(B) = \frac{\Delta V_0}{1 + (\omega_L \tau_s)^2}, \tau_s = \frac{\hbar}{g\mu_B B_{1/2}}$	<ul style="list-style-type: none"> <li>Stray field from surface roughness induce additional spin relaxation at FM/SC interface.</li> <li>Apply in-plan field (<math>B_y</math>) to enhance spin polarization.</li> </ul>
Advantage	<ul style="list-style-type: none"> <li>Device fabrication and spin lifetime extraction are relatively easy.</li> </ul>	
Disadvantage	<ul style="list-style-type: none"> <li>Suspicious signals are easily involved in the measured signal.</li> </ul>	

Setup	Nonlocal	
	4T Hanle	4T spin valve
Schematics		
Spin injection	<ul style="list-style-type: none"> <li>Spin accumulation (<math>\Delta\mu = \mu^\uparrow - \mu^\downarrow</math>) in SC channel is built under the spin injector by passing a current through a FM tunnel contact.</li> <li>Spin accumulation laterally diffuses in channel towards the spin detector.</li> </ul>	
Spin detection	<ul style="list-style-type: none"> <li><math>V_{NL}</math> is proportional to the projection of spin accumulation onto the magnetization orientation of the spin detector (E3).</li> </ul>	
	<ul style="list-style-type: none"> <li>Apply transverse field (<math>B_z</math>) to induce spin precession and spin dephasing (Hanle effect)</li> <li>Extract spin lifetime using 1-D spin drift-diffusion model:  <math display="block">V_{NL} \propto \pm \int_0^\infty \frac{1}{\sqrt{4\pi Dt}} \exp(-L^2/4Dt) \times \cos(\omega_L t) \times \exp(-t/\tau_s) dt</math> </li> </ul>	<ul style="list-style-type: none"> <li>Apply in-plan field (<math>B_y</math>) to build parallel and antiparallel magnetization configuration between the spin injector (E2) and the spin detector (E3).</li> </ul>
Advantage	<ul style="list-style-type: none"> <li>Promising transport measurements by avoiding suspicious signal with nonlocal setup.</li> </ul>	
Disadvantage	<ul style="list-style-type: none"> <li>Device fabrication is more complex due to the smaller dimension.</li> <li>Spin polarization voltage is smaller to detect after lateral transport.</li> </ul>	

# Chapter 3 Electrical Spin Injection and Transport in Ge

## 3.1 Introduction of Spin Injection in Ge

During the last decades, a continuous downscaling of CMOS field-effect-transistor dimensions has led to an increase in device performance and efficiency.<sup>18</sup> With gate lengths of currently 14 nm in production, this downscaling is gradually reaching the end. The alternative device concepts that make use of spin polarization as state variables (spintronics) are being increasingly investigated as potential candidates for logic devices. The current spin polarization in a semiconductor (SC) can be defined as  $P_{J,SC} = (J_{\uparrow} - J_{\downarrow}) / (J_{\uparrow} + J_{\downarrow})$ , where  $J_{\uparrow}$  and  $J_{\downarrow}$  are the current densities for spin-up and spin-down electrons, respectively. They describe the asymmetry of majority and minority spin currents in the semiconductor. The prototypical spin-polarized field-effect-transistor (FET) was proposed by Datta and Das<sup>3</sup> in 1990, which was followed by numerous concepts for spintronic devices.<sup>44-47</sup> In these concepts, there are two essential achievements to realize functional devices: one is the electrical detection of spin transport in SC channel. The other is the effective manipulation of spin-polarized currents.

Ever since the earlier developments of electrical spin injection in Si,<sup>26,28,29</sup> Ge has been investigated as another promising candidate for CMOS-compatible spintronics. Because of the crystal inversion symmetry of Si and Ge, the spin relaxation of conduction electrons are dominated by Elliott-Yafet mechanism<sup>1</sup> that the spin relaxation time is proportional to the momentum relaxation time. Therefore, the higher electron mobility of Ge promises a longer spin

diffusion length. On the other hand, as shown in **Table 1-1**, the spin orbital interaction (SOI) of Ge (0.29 eV) is between that of Si (0.044 eV) and GaAs (0.35 eV), so it is approachable to combine the techniques of electrical spin injection in Ge<sup>30,31</sup> and spin Hall/inversed spin Hall effects in Ge<sup>48,49</sup> for device applications.

In **Chapter 3**, I will present two systematic works of electrical spin injection in Ge using different contact materials: one is Fe/MgO/ $n^+$ -Ge tunnel contact, and another is Mn<sub>5</sub>Ge<sub>3</sub>C<sub>0.8</sub>/Al<sub>2</sub>O<sub>3</sub>/ $n^+$ -Ge tunnel contact. The former is a conventional structure used by Si<sup>29,50</sup> and Graphene,<sup>51-55</sup> and the later is an innovative structure that replaces the ferromagnetic metal by the ferromagnetic semiconductor (Mn<sub>5</sub>Ge<sub>3</sub>C<sub>0.8</sub>), which holds great potential to build a high quality Schottky contact for device application.

### 3.2 Electrical Spin Injection in *n*-Ge Using Fe/MgO/*n*<sup>+</sup>-Ge Tunnel Contact

This section reported the electrical detection of spin injection in *n*-Ge using single-crystalline Fe/MgO/*n*<sup>+</sup>-Ge tunnel junction, and compared the temperature dependence of spin lifetime in *n*-Ge characterized by three-terminal (3T) and four-terminal (4T) Hanle measurements. **Figure 3-1(a)** shows the schematic of the 3T device structure and the measurements setup (see device fabrication in **Appendix A**). A DC bias voltage ( $V_b = -5 \sim +2$  V) coupled with an AC modulation voltage ( $V_{AC} = 0.1$  V) was applied to the active contact ( $3 \times 50 \mu\text{m}^2$ ) to create spin polarization in the Ge channel. The 3T spin polarization voltage is linearly proportional to the spin accumulation given by  $\Delta V = \Delta\mu \times \gamma / 2e$ , where  $\gamma$  is the tunneling spin polarization of the Fe/MgO interface, and  $\Delta\mu = \mu^\uparrow - \mu^\downarrow$  is the difference between the electrochemical potentials of spin-up and spin-down electrons. By applying a transverse magnetic field, the spin polarization voltage decreases due to the Hanle effect, in which the spin precesses around the magnetic field direction at the Larmor frequency<sup>20,28</sup> ( $\omega_L = g\mu_B B_z / \hbar$ , where  $g = 1.6$  is the Landé  $g$ -factor for Ge,  $\mu_B$  is the Bohr magneton and  $\hbar$  is the reduced Planck constant). The 3T Hanle resistance ( $R_{3T} = \Delta V_{3T} / I_{AC}$ ) is defined as the Hanle voltage divided by the AC modulation current, which is calculated from the differential resistance of the spin injection circuit at each  $V_b$  by a separate scan, and it could be modeled by a Lorentzian function:<sup>28</sup>

$$\Delta R_{3T}(B) = \Delta R_{3T} / \left[ 1 + (\omega_L \tau_s)^2 \right] \quad (3-1)$$



As shown in **Figure 3-1(b)**, the 3T Hanle curve at 4 K was well fitted by **Equation 3-1**, and in particular, the extracted spin lifetime  $\tau_s$  at 4 K is 900 ps.

Deriving from the standard model of spin diffusion and relaxation, the spin injection theory<sup>34,56-58</sup> predicts that when the spin transport along a lateral channel in the diffusive regime, the occurrence of an appreciable magnetoresistance (MR) is directly related to an upper threshold value of the spin resistance-area (RA) product at a single ferromagnet (FM)/semiconductor (SC) interface. In the case when the spin diffusion length  $l_{sf}$  is shorter than contact width  $W$  but longer than channel thickness  $w$ , *i.e.*, ( $W \gg l_{sf} \gg w$ ), the spin RA product is  $R_s \cdot A = \gamma^2 \rho l_{sf}^2 / w \approx 6 \times 10^6 \Omega \cdot \mu\text{m}^2$ , where the tunnel spin polarization of Fe/MgO interface is  $\gamma \approx 0.5$ ,<sup>59</sup> the Ge resistivity is  $\rho \approx 1 \Omega \cdot \text{m}$  with a doping concentration of  $1 \times 10^{16} \text{ cm}^{-3}$ , and the spin diffusion length is  $l_{sf} = 600 \text{ nm}$  at 4 K as calculated from the  $\tau_{3T}$  in **Figure 3-1(b)**. In our case, the 3T spin RA product at zero bias was estimated to be  $R_{3T} \cdot A \approx 5 \times 10^4 \Omega \cdot \mu\text{m}^2$  at 4 K. The predicted upper limit of the RA product is two order of magnitude larger than that of our 3T devices RA, suggesting that the spin accumulation is likely to occur in the Ge channel. Otherwise, the extracted RA product would be much larger than the upper limit if the spins are trapped in the localized interface states.<sup>43</sup>

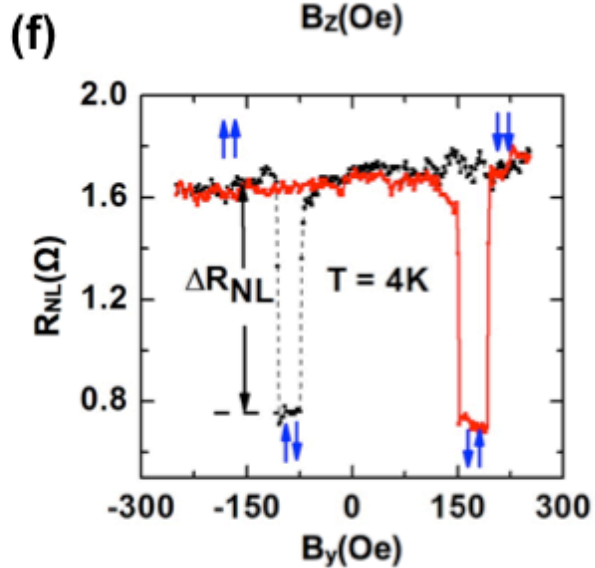
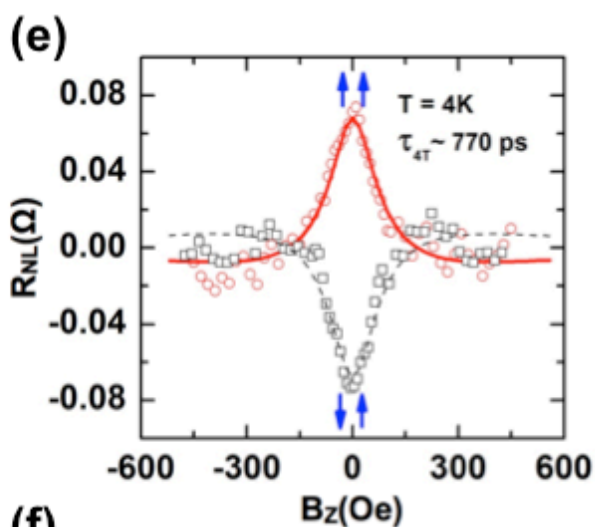
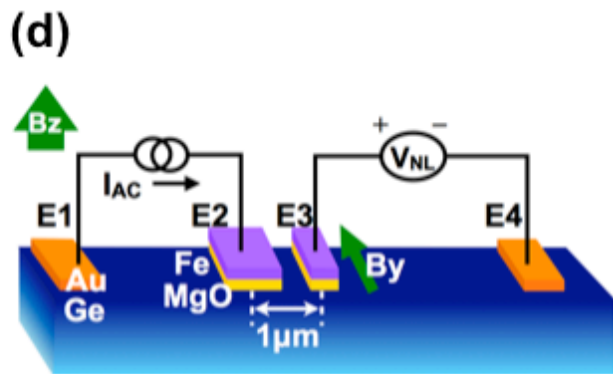
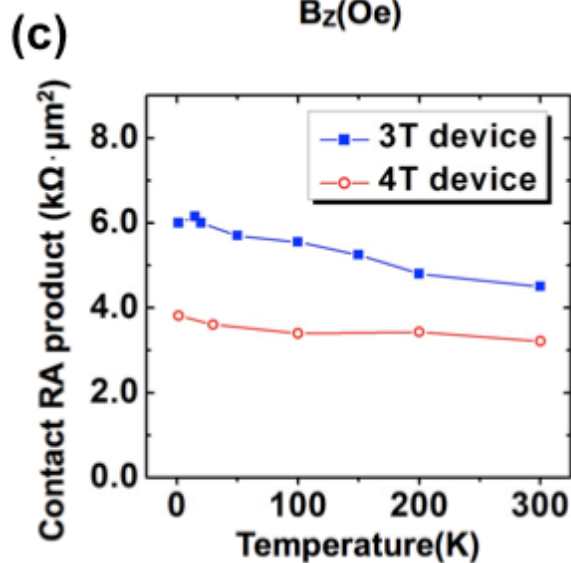
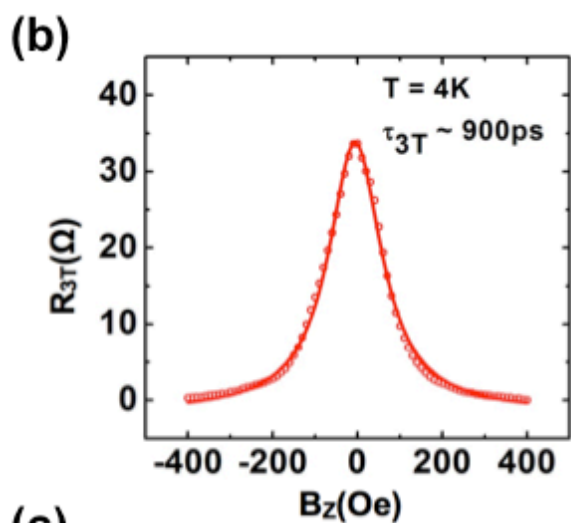
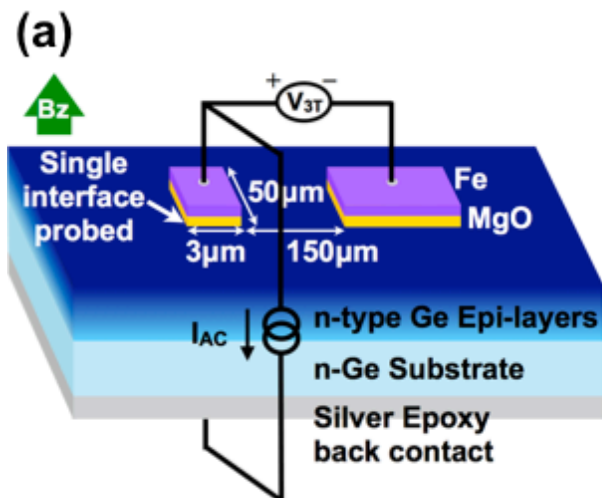
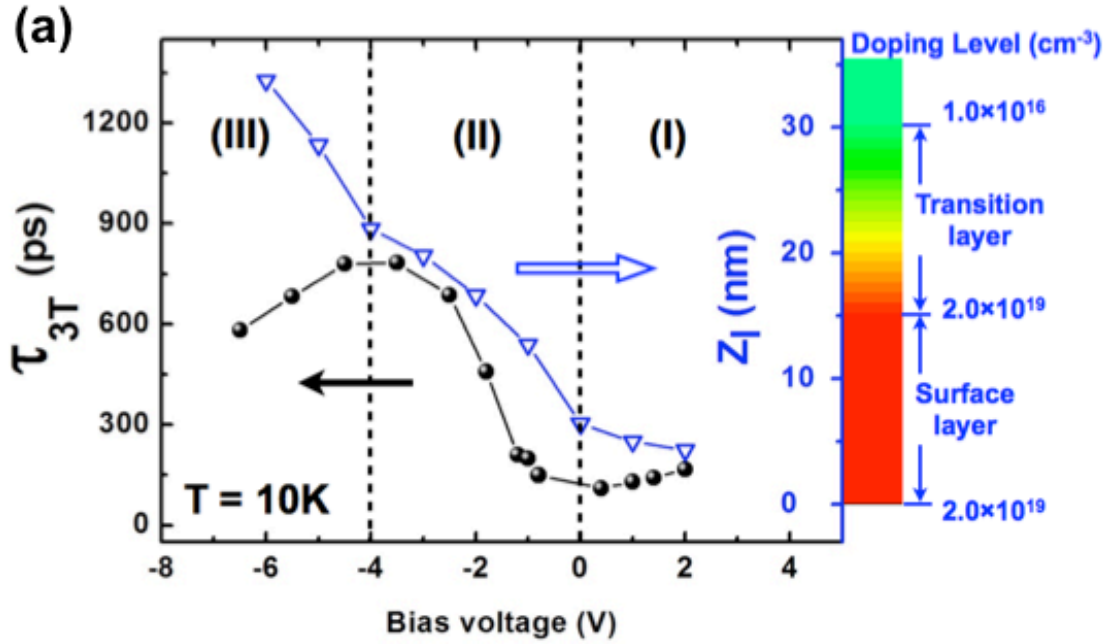


**Figure 3-1.** Electrical spin injection in Ge using Fe/MgO/ $n^+$ -Ge tunneling contact. (a) Schematics of the 3T device structure and the measurements scheme. The size of the active contact is  $3 \times 50 \mu\text{m}^2$ . (b) Resistance ( $R_{3T}$ ) from 3T Hanle measurements at 4 K. The extracted  $\tau_{3T}$  is 900 ps. (c) The temperature dependence of the contact resistance-area (RA) product of 3T and 4T devices,<sup>30</sup> respectively. (d) Schematics of 4T device structure and the nonlocal measurements scheme. The center-to-center distance between the spin injector (E2) and detector (E3) is  $1 \mu\text{m}$ . (e) Nonlocal resistance ( $R_{NL}$ ) from the 4T nonlocal Hanle measurements at 4 K with a DC injection current of  $-130 \mu\text{A}$ . The extracted  $\tau_{4T}$  is 770 ps. The red circle and black square symbols are for the signal measured when the spin injector (E2) and detector (E3) are in parallel or antiparallel configurations, respectively. The blue arrows indicate the magnetization orientations of the spin injector and detector. (f) 4T nonlocal spin valve measured at 4 K with a DC injection current of  $-20 \mu\text{A}$  and an AC modulation current of  $-10 \mu\text{A}$ . Figures (d), (e) and (f) are adopted from our previous work.<sup>30</sup>

For the 4T device, **Figure 3-1(d)** is the schematic diagram of the device structure and nonlocal measurements scheme (see device fabrication in **Appendix A**). **Figure 3-1(e)** shows 4T nonlocal Hanle measurements at 4 K, where the nonlocal resistance ( $R_{NL}$ ) is defined as the nonlocal voltage ( $V_{NL}$ ) divided by the AC modulation current ( $I_{AC}$ ), and the blue arrows indicate the magnetization directions of the injector and detector. The solid (dashed) lines were fitting based on the 1-D spin drift-diffusion model:<sup>30</sup>

$$R_{NL} \propto \pm \int_0^{\infty} \frac{1}{\sqrt{4\pi Dt}} \exp\left[-\frac{L^2}{4Dt}\right] \cos(\omega_L t) \times \exp\left(-\frac{t}{\tau_{4T}}\right) dt \quad (3-2)$$

In the above equation, + (-) sign is for the parallel (antiparallel) magnetization configuration,  $D$  is the diffusion constant,  $\omega_L$  is the Larmor frequency as defined above. A spin lifetime of 770 ps at 4 K was obtained by fitting the Hanle curves with **Equation 3-2**. The results from 3T and 4T nonlocal Hanle measurements turned out to be close at 4 K, which is consistent with the previous study on spin lifetimes in Si using 3T and 4T measurements.<sup>60</sup> **Figure 3-1(f)** shows the nonlocal spin valve signal at 4 K. By applying an in-plane magnetic field ( $B_y$ ),  $V_{NL}$  depends on the relative magnetization orientations of the injector and detector, as a direct indication of the spin current injected into the Ge channel. Since the 3T and 4T nonlocal Hanle curves were measured from different devices, it is necessary to assess the junction properties of two devices. As shown in **Figure 3-1(c)**, the contact RA products for both devices were close and exhibited the same temperature dependence (slight increase as the temperature decreases), which indicate that the junction properties for 3T and 4T nonlocal Hanle devices are similar.



—  $E_c$  (eV) —  $E_v$  (eV) ·····  $n_e$  ( $\text{cm}^{-3}$ ) ·····  $N_D$  ( $\text{cm}^{-3}$ )

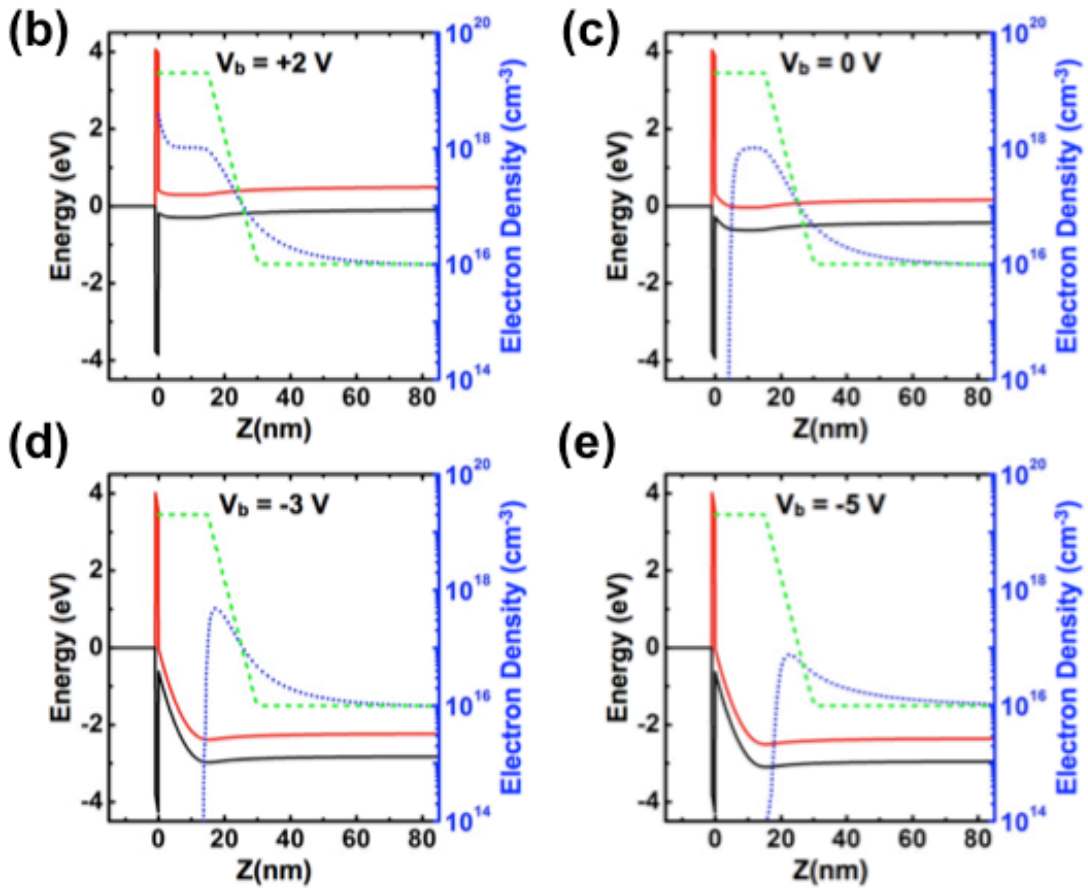


**Figure 3-2.** Spin lifetime as a function of bias voltage in the modulation-doped  $n$ -Ge at 10 K. (a) The left  $Y$ -axis shows the bias dependence of  $\tau_{3T}$  (solid circle), and the right  $Y$ -axis shows the bias dependence of the average penetration depth,  $Z_I$  (open triangle) extracted from the device simulation at 10 K. The inset color bar shows the corresponding doping level of the Ge sample. Starting from the MgO/Ge interface, the 15 nm surface layer has  $n = 2 \times 10^{19} \text{ cm}^{-3}$ , followed by the 15 nm transition layer with the doping level from  $n = 2 \times 10^{19}$  to  $1 \times 10^{16} \text{ cm}^{-3}$ . (b), (c), (d), and (e) The left  $Y$ -axes show the simulated band diagram (solid line), and the right  $Y$ -axes show the spatial distribution of electron density (dot line) under different bias voltages  $V_b = +2, 0, -3$  and  $-5 \text{ V}$ , respectively, where  $E_C$  ( $E_V$ ) stands for the conduction (valence) band edge, and  $n_e$  ( $N_D$ ) stands for the electron (dopant) density, respectively.

Before comparing the temperature dependence of  $\tau_{3T}$  and  $\tau_{4T}$ , we investigated the bias dependence of  $\tau_{3T}$ . In **Figure 3-2(a)**, the left (right)  $Y$ -axis shows  $\tau_{3T}(Z_I)$  as a function of the bias voltage at 10 K, respectively. Here the average penetration depth ( $Z_I$ ) is determined by the spatial distribution of electron density:

$$Z_I \equiv \int_0^L z \times n_e(z) dz / \int_0^L n_e(z) dz \quad (3-3)$$

where  $L$  is defined from the position of back contact, and  $n_e(z)$  is the electron density obtained from a self consistent device simulator, Sentaurus Device, using Fermi-Dirac statistics model, nonlocal tunneling model, and incomplete ionization model at 10 K. In addition, the inset color bar shows the corresponding doping level of a 15 nm surface layer ( $n = 2 \times 10^{19} \text{ cm}^{-3}$ ), followed by a 15 nm transition layer with the doping level from  $n = 2 \times 10^{19}$  to  $1 \times 10^{16} \text{ cm}^{-3}$ . The position of spin accumulation should consider both electric field distribution and spin drift-diffusion equation,<sup>61</sup> but the complete device simulation is beyond the scope of this section, so we only simulated the electric field distribution here. The real position of spin accumulation should be offset  $Z_I$  towards the low doped region. **Figure 3-2(b-e)** illustrated the simulated band diagrams (left  $Y$ -axes, solid line) and electron density (right  $Y$ -axes, dot line) under different bias voltages ( $V_b = +2, 0, -3$  and  $-5$  V), in which  $E_C$  ( $E_V$ ) stands for the conduction (valence) band edge, and  $n_e$  ( $N_D$ ) stands for the electron (dopant) density, respectively. According to the bias dependence of  $\tau_{3T}$ , **Figure 3-2(a)** can be roughly divided into three regions: region (I) stands for the forward bias region ( $V_b > 0$  V in **Figure 3-2(b)**), where  $Z_I$  is reduced to be within the uniformly heavily-doped ( $n = 2 \times 10^{19} \text{ cm}^{-3}$ ) surface layer. In this region,  $\tau_{3T}$  is relatively small ( $\sim 200$  ps) due to the

severe ionized impurity scattering, and it is not sensitive to the forward bias voltage because most of the electrons are accumulated within the uniformly doped surface layer. Region (II) stands for the moderate reverse bias region ( $-4 \text{ V} < V_b < 0 \text{ V}$  in **Figure 3-2(d)**), in which  $Z_I$  gradually increases with the bias voltage and extends from the heavily-doped surface layer into the transition layer. It is clear to see that  $\tau_{3T}$  increases with the bias voltage because spin-polarized electrons are more easily injected into the relatively low-doped region ( $n = 2 \times 10^{19}$  to  $1 \times 10^{16} \text{ cm}^{-3}$ ). Region (III) stands for the large reverse bias region ( $V_b < -4 \text{ V}$  in **Figure 3-2(e)**), where  $Z_I$  keeps increasing but  $\tau_{3T}$  starts to drop with increasing reverse bias. The possible causes might attribute to spin-drift-based mechanism,<sup>62</sup> thermalization process,<sup>63</sup> or phonon emission process.<sup>64</sup>

Finally we studied the temperature-dependences of  $\tau_{3T}$  and  $\tau_{4T}$ . Because the bias voltage in the 3T scheme was applied across the whole sample rather than mainly on the tunneling junction, the 3T bias voltage is usually much larger than that in the 4T scheme. To compare  $\tau_{3T}$  and  $\tau_{4T}$  under the similar bias condition, we chose the specific bias voltage with about the same current density. **Figure 3-3(a)** shows 3T Hanle resistance peaks measured at different temperatures (1.5 ~ 50 K) with a DC bias voltage of -3.5 V, or equivalently an injection current density of  $-20 \mu\text{A} / \mu\text{m}^2$ , and **Figure 3-3(b)** shows 4T Hanle resistance peaks in the same temperature range with a DC bias voltage of -0.2 V, or equivalently an injection current density of  $-26 \mu\text{A} / \mu\text{m}^2$ . In addition, 3T and 4T Hanle curves (open circle) are well fitted by **Equation 3-**



1 and 3-2 (solid line), respectively. The extracted  $\tau_{3T}$  (blue solid square) and  $\tau_{4T}$  (red open circle) were plotted as a function of temperature in **Figure 3-3(c)**.

$$1/\tau_s = \lambda/\tau_L = \lambda \cdot T^{1.66}, \text{ or } \tau_s = \lambda^{-1} \cdot T^{-1.66} \quad (3-4)$$

where  $\lambda$  is a constant, and the temperature dependence of  $T^{1.66}$  for  $1/\tau_L$  is based on the experimental result.<sup>65</sup> The power-law fitting of the temperature dependence of our measured spin lifetimes shows that  $\tau_s \propto T^{-1.9}$  for both 3T Hanle and 4T nonlocal Hanle measurements, which is in good agreement with the theoretical prediction. For comparison, Sasaki's results<sup>60</sup> of 3T and 4T spin injection into Si are re-plotted as the inset of **Figure 3-3(c)**, in which the  $\tau_{3T}$  and  $\tau_{4T}$  behave very similar in the whole temperature range between 8 K and 100 K. Although our measured  $\tau_{3T}$  and  $\tau_{4T}$  at high temperature ( $T > 50$  K) show similar temperature dependence of  $\tau_s \propto T^{-1.9}$  due to phonon scattering,  $\tau_{3T}$  starts to drop from a lower temperature than  $\tau_{4T}$ , which might be attributed to additional scattering mechanisms. The possible reasons for such a difference at the high temperature regime are discussed in the following. The active contact in the 3T geometry acts as both the injector and detector, while the detector in the 4T geometry is separated from the injector. Since the spin signal is measured under the detector, the electric field and current density is inevitably much higher for 3T than that for 4T. When the temperature increases and the carrier density becomes high, carrier collisions act as an important scattering mechanism<sup>66</sup> contributing to the increased momentum scattering in the 3T geometry.

In summary, we compared 3T and 4T methods to characterize the temperature dependence of spin lifetimes in  $n$ -Ge. At the low temperature regime ( $T \leq 10$  K),  $\tau_{3T}$  and  $\tau_{4T}$  behave very similar; however, the difference between  $\tau_{3T}$  and  $\tau_{4T}$  shows up in the high temperature regime ( $T > 10$  K). The results show that both methods are useful to extract the spin lifetime, but  $\tau_{3T}$  is more easily affected by the accompanied the charge current and electric field at the high temperature regime ( $T > 10$  K).

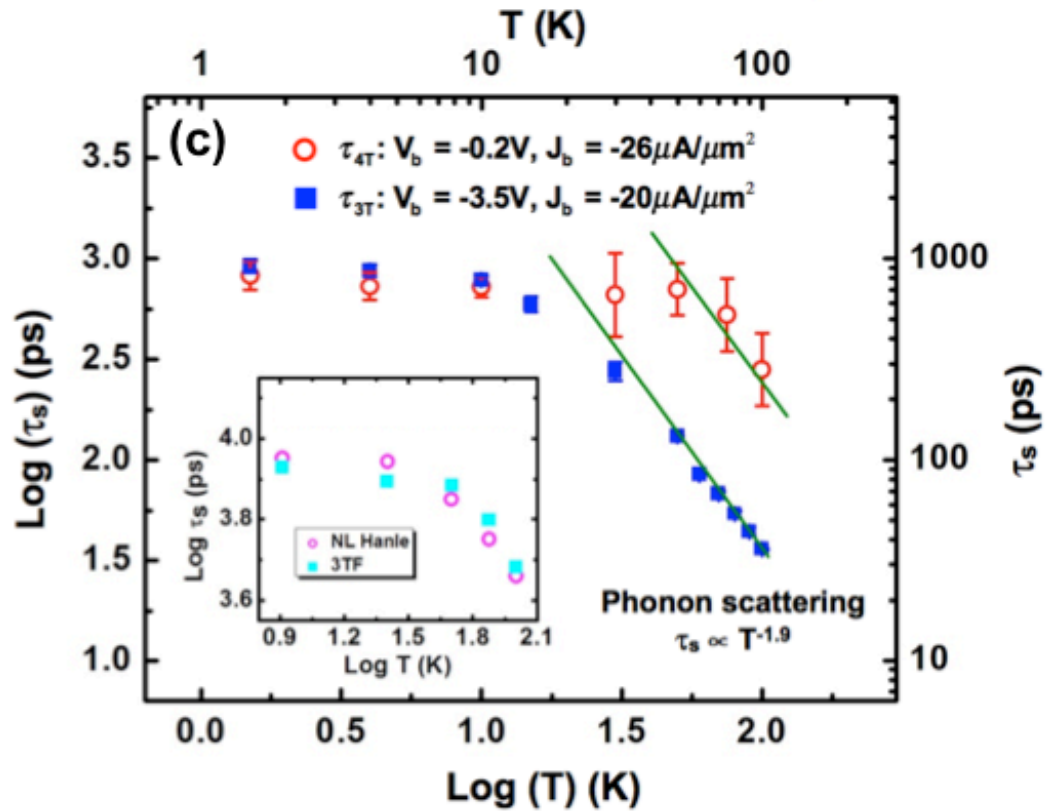
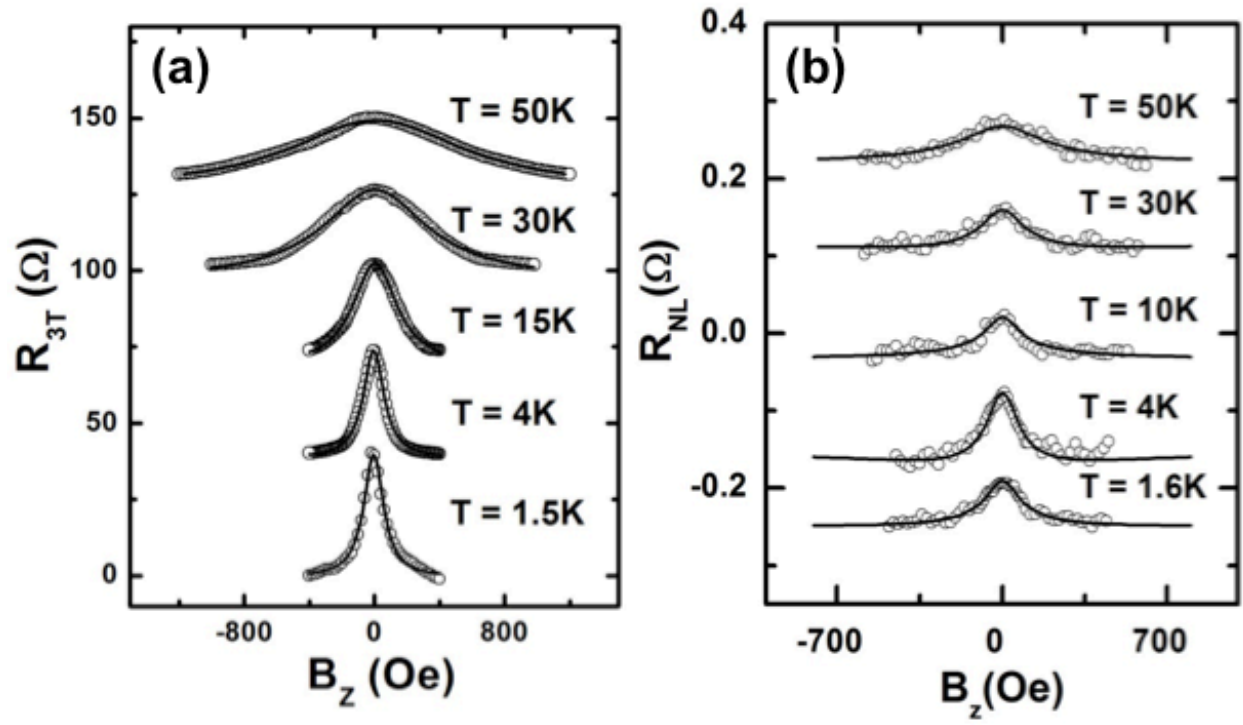


**Figure 3-3.** Spin lifetime as a function of temperature in the *n*-Ge. (a) and (b) Temperature dependences of 3T (  $V_b = -3.5$  V,  $J_b = -20$   $\mu\text{A}/\mu\text{m}^2$  ) and 4T nonlocal Hanle (  $V_b = -0.2$  V,  $J_b = -26$   $\mu\text{A}/\mu\text{m}^2$  ) measurements at different temperatures (1.5 ~ 50 K), respectively. The 3T Hanle curves are well-fitted by the Lorentzian shape (**Equation 3-1**), and the 4T nonlocal Hanle curves are fitted by the 1-D spin drift-diffusion model (**Equation 3-2**). (c) Temperature dependences of  $\tau_{3T}$  and  $\tau_{4T}$  under close range of bias current density. At low temperature ( $T < 10$  K),  $\tau_{3T}$  and  $\tau_{4T}$  behave very similar; at  $T > 10$  K, the fitting shows that  $\tau_{3T}$  and  $\tau_{4T}$  have similar phonon scattering behavior ( $\tau_s \propto T^{-1.9}$ ) but  $\tau_{3T}$  starts to drop at lower temperature. The inset shows the temperature dependent spin lifetime adopted from Sasaki's work.<sup>60</sup>

### 3.3 Electrical Spin Injection in *n*-Ge Using Mn<sub>5</sub>Ge<sub>3</sub>C<sub>0.8</sub>/Al<sub>2</sub>O<sub>3</sub> Tunnel Contact

This section reported electrical spin injection and detection in degenerately doped *n*-Ge channel using Mn<sub>5</sub>Ge<sub>3</sub>C<sub>0.8</sub>/Al<sub>2</sub>O<sub>3</sub>/*n*<sup>+</sup>-Ge tunnel contact. The whole structure is integrated on a Si wafer for CMOS compatibility. From 3T Hanle-effect measurements, we observed a spin accumulation up to 10 K. The spin lifetime is extracted to be 38 ps at 4 K using Lorentzian fitting, and the spin diffusion length is estimated to be 367 nm due to the high diffusion coefficient ( $D = 37.5 \text{ cm}^2/\text{s}$ ) of the highly doped Ge channel. Though spin injection into Ge has previously been shown for devices fabricated on Ge substrates, the integration of such Ge channels on Si substrates holds great potential for future CMOS-compatible SiGe-based spintronics devices.

To demonstrate spin injection into a semiconductor channel, the conductivity mismatch problem<sup>33,34</sup> can be solved by inserting a thin oxide layer between the ferromagnetic metal and the semiconductor channel. For example, spin injection was demonstrated in Ge by using tunnel contacts<sup>30,31,67</sup> and Schottky contacts.<sup>68</sup> In addition to traditional ferromagnetic metals (such as Fe, Co and Ni<sub>0.8</sub>Fe<sub>0.2</sub>), Mn<sub>5</sub>Ge<sub>3</sub> is a ferromagnet (FM) with a Curie temperature ( $T_c$ ) of 296 K,<sup>69</sup> and the  $T_c$  could be further enhanced by C-doping (Mn<sub>5</sub>Ge<sub>3</sub>C<sub>x</sub>) up to 450 K.<sup>70-72</sup> More importantly, Mn<sub>5</sub>Ge<sub>3</sub>C<sub>x</sub> has a negligible conductivity mismatch with highly doped Ge,<sup>73</sup> and it can be grown epitaxially on Ge (111),<sup>72</sup> which is helpful to avoid the formation of interface defects and hence improve the spin injection/detection efficiency. These favorable properties make it particularly interesting as a contact material for spin injection into Ge.

The three-terminal measurements setup and the cross section of the active contact area are shown schematically in **Figures 3-4(a)** and **(b)**. The device fabrication process is attached in **Appendix B**. In the experiment, the temperature-dependent three-terminal Hanle-effect measurements were carried out in a Quantum Design physical property measurements system (PPMS). A DC current was applied between contact 2 and 3 with a Keithley 6221 DC/AC current source, and the voltage difference  $V_{12}$  was measured between contact 2 and 1 with a Keithley 2182 nanovoltmeter. Temperature-dependent  $I$ - $V$  measurements between two adjacent  $\text{Mn}_5\text{Ge}_3\text{C}_{0.8}/\text{Al}_2\text{O}_3/n^+$ -Ge tunnel contacts (contact 1 and 2) are shown in **Figure 3-4(c)**, in which the inset shows the temperature dependence of the normalized zero-bias resistance  $R_0(T)/R_0(300\text{K})$ . The moderate temperature dependence suggests the total current consists of both tunneling and leakage components for a large active contact ( $98 \times 198 \mu\text{m}^2$ ). **Figure 3-4(d)** shows a simulated conduction band diagram of the  $\text{Mn}_5\text{Ge}_3\text{C}_{0.8}/\text{Al}_2\text{O}_3/n^+$ -Ge tunnel contact at 10 K under zero bias, which is obtained by solving the Poisson and Schrödinger equations self-consistently in one dimension.<sup>74</sup> The sharp tunneling barrier and a well-defined potential reservoir in the conduction band of  $n^+$ -Ge near the  $\text{Al}_2\text{O}_3/n^+$ -Ge interface are two essential features for efficient spin injection and detection.<sup>75</sup>

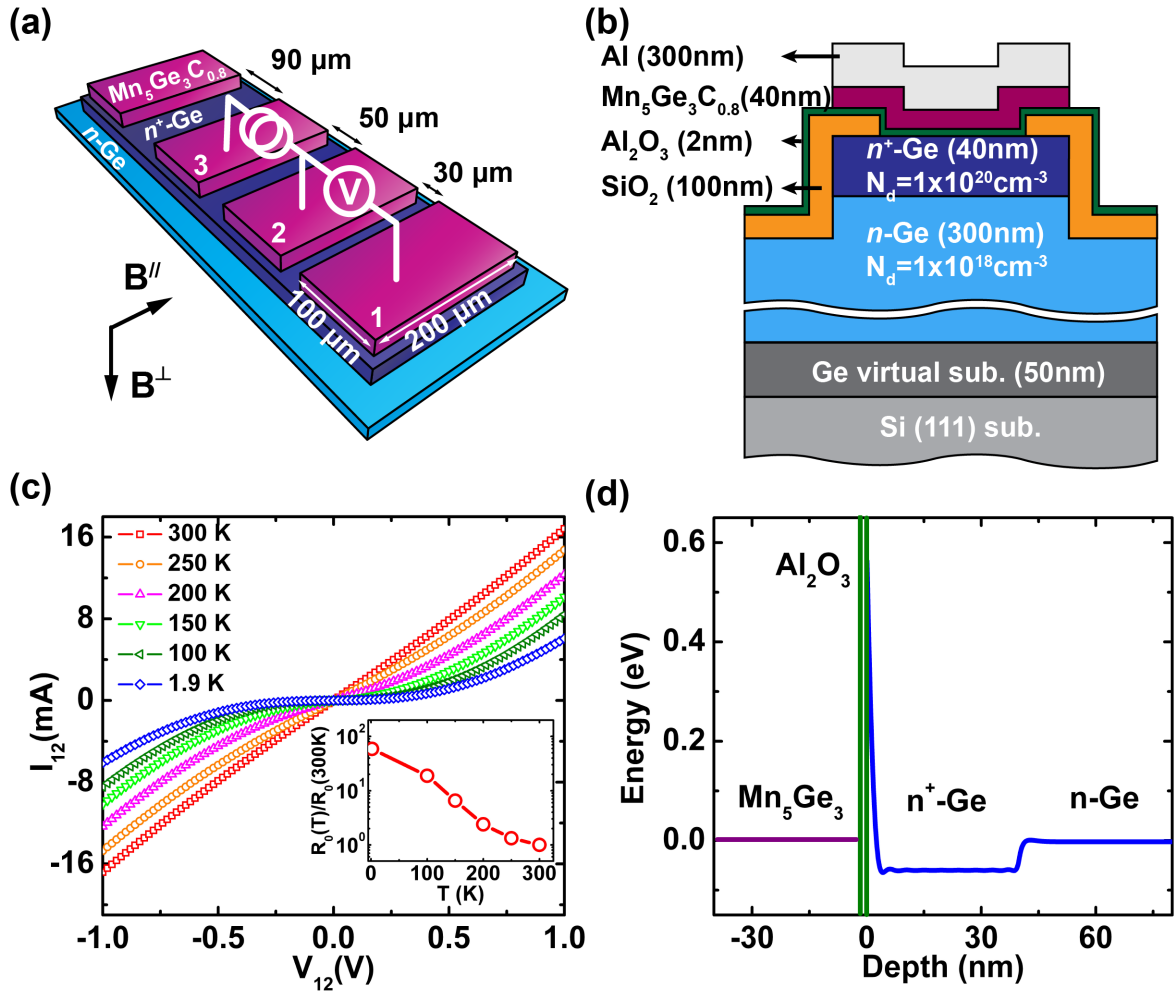


**Figure 3-4.**  $\text{Mn}_5\text{Ge}_3\text{C}_{0.8}$  device structure and contact properties. (a) Schematic illustration of device structure and measurements setup, where the arrows indicate the magnetic field in the perpendicular ( $B^{\perp}$ ) and parallel ( $B^{\parallel}$ ) direction. (b) Cross section structure of the  $\text{Mn}_5\text{Ge}_3\text{C}_{0.8}/\text{Al}_2\text{O}_3/n^+\text{-Ge}$  tunneling contact. (c) Temperature dependent  $I$ - $V$  measurements between contacts 1 and 2. The inset shows the temperature dependence of the normalized zero-biased resistance. (d) Simulated conduction band profile under zero bias at 10 K.

High-resolution transmission electron microscopy (HRTEM) was used to characterize the  $\text{Mn}_5\text{Ge}_3\text{C}_{0.8}/\text{Al}_2\text{O}_3/n^+$ -Ge junction. Material intermixing can occur at the  $\text{Mn}_5\text{Ge}_3\text{C}_{0.8}/n^+$ -Ge interface if  $\text{Mn}_5\text{Ge}_3\text{C}_{0.8}$  is directly sputtered on top of a Ge layer, as can be seen in **Figure 3-5(a)**. To ensure material separation and enhance spin polarization, an  $\text{Al}_2\text{O}_3$  tunneling oxide was inserted at the interface,<sup>76</sup> as shown in **Figure 3-5(b)**. Atomic force microscopy (AFM) on a reference sample without the Al/ $\text{Mn}_5\text{Ge}_3\text{C}_{0.8}$ -metallization was used to measure the roughness of the  $\text{Al}_2\text{O}_3$  surface in order to obtain information on the  $\text{Mn}_5\text{Ge}_3\text{C}_{0.8}/\text{Al}_2\text{O}_3$  interface. **Figure 3-5(c)** shows an AFM image of the surface of the  $\text{Al}_2\text{O}_3$  tunneling oxide with a square area of  $500 \times 500 \text{ nm}^2$ , and **Figure 3-5(d)** shows a cross-sectional height profile along the corresponding double heads arrow. We obtained a root-mean-square (rms) roughness of 0.2 nm with a correlation length of 30 nm, which is comparable to the results obtained in Dash's work<sup>42</sup> and suggests a reduced spin accumulation as well as spin lifetime from the effects of local magnetostatic fields.



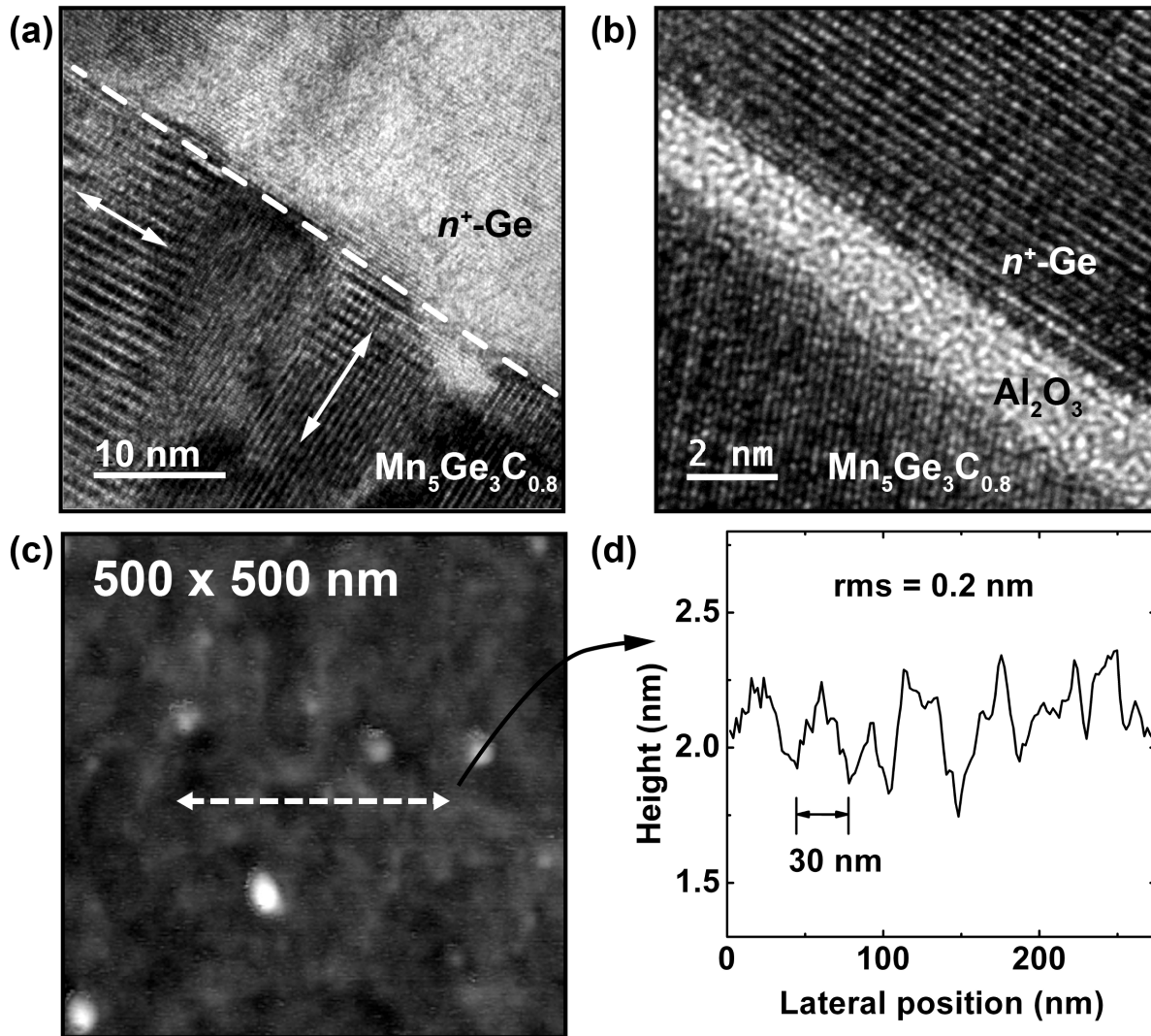


**Figure 3-5.** Structure characterization of the  $\text{Mn}_5\text{Ge}_3\text{C}_{0.8}/\text{Al}_2\text{O}_3/n^+\text{-Ge}$  contact. (a) High-resolution TEM image of a  $\text{Mn}_5\text{Ge}_3\text{C}_{0.8}/n^+\text{-Ge}$  contact. Arrows indicate two different orientations of crystal planes. (b) High-resolution TEM image at the interface of a  $\text{Mn}_5\text{Ge}_3\text{C}_{0.8}/\text{Al}_2\text{O}_3/n^+\text{-Ge}$  (111) tunneling contact. (c) AFM image of the  $\text{Al}_2\text{O}_3$  surface prior to metal electrode deposition. (d) Cross-sectional height profile along the dashed line in (c).

**Figures 3-6(a)** and **(b)** show voltage signals originating from the Hanle and the inverted Hanle effect while the magnetic field was applied perpendicularly ( $B^\perp$ ) to the  $\text{Mn}_5\text{Ge}_3\text{C}_{0.8}/\text{Al}_2\text{O}_3/\text{Ge}$ -interface or parallel ( $B^\parallel$ ) to the direction of the long axis of the  $\text{Mn}_5\text{Ge}_3\text{C}_{0.8}$  electrodes, respectively. Those measurements were performed at 4 K under various spin injection and extraction conditions. The Hanle curve indicates a dephasing process of spin polarization while spin-polarized electrons precess at a Larmor<sup>28</sup> frequency around a transvers (perpendicular) magnetic field. It strongly suggests that spin-polarized electrons are accumulated in the Ge channel.<sup>42</sup> On the contrary, the appearance of the inverted Hanle effect is a consequence of spatially inhomogeneous magnetostatic stray-fields that arise from the finite roughness of the  $\text{Mn}_5\text{Ge}_3\text{C}_{0.8}/\text{Al}_2\text{O}_3$ -interface, which enhance incoherent spin precession and reduce spin polarization. In the inverted Hanle effect, an in-plane magnetic field aligns the conduction electron spins in the semiconductor channel, and therefore reduces the diminishing effect of spin precession at interface and restores spin polarization.<sup>42</sup>

The qualitatively most notable features about our measurements are the signs of the Hanle and inverted Hanle signals under spin injection ( $I < 0$ ) and extraction ( $I > 0$ ) conditions. The measured signals  $\Delta V_{Hanle}$  are determined by  $\Delta V_{Hanle} \propto P_i \times P_d \times I$ , where  $P_i$  and  $P_d$  are the spin polarization for spin injector and spin detector, respectively. In the present case,  $P_i$  and  $P_d$  have the same sign, so  $\Delta V_{Hanle}$  should be positive for spin extraction conditions and negative for spin injection, but the present samples show the opposite trends in **Figure 3-6(a)**. Sign inversion of  $\Delta V_{Hanle}$  has been observed in three-terminal devices for different electrode materials using

Schottky as well as tunneling contacts, and the sign has been reported to change under different applied bias and temperature.<sup>77-79</sup>

As shown in **Figure 3-6(c)**, the Hanle ( $\Delta V_{Hanle}$ ) and the inverted Hanle ( $\Delta V_{inv.Hanle}$ ) curves change sign at different values of the applied bias. Two main mechanisms have been discussed for the inversion of spin polarization at an FM/oxide/SC interface: one is tunneling via interfacial resonant states,<sup>80-82</sup> and another is tunneling from bound states into a heavily doped SC surface layer, from which minority-spin states are preferentially extracted.<sup>75,83</sup> Those mechanisms can be responsible for the sign change of the Hanle and the inverted Hanle curves under different bias conditions in our system. Since the  $Mn_5Ge_3C_{0.8}$  contact is polycrystalline, the orientation of magnetization is not perfectly aligned in all crystal grains. As a result, even a magnetic field aligned parallel to the  $Mn_5Ge_3C_{0.8}/Al_2O_3/n^+-Ge$ -interface can induce spin precession and reduce spin accumulation. On the other hand, the band structure of our devices might play an important role. The simulation results of the conduction band profile shown in **Figure 3-4(d)** indicate that the itinerant electrons are localized in the potential reservoir close to the semiconductor surface, and so spin injection can be expected to occur predominantly into the bound states.<sup>83</sup>

It is also noted that, depending on the orientation between an external magnetic field and material interfaces, the density of states inside a quantum well are affected accordingly: a perpendicular magnetic field increases the energy of Landau levels ( $\Delta E_{Landau} = \hbar\omega_c = \hbar eB/m$ ), whereas a parallel field lifts the spin degeneracy due to Zeeman splitting ( $\Delta E_{Zeeman} = g\mu_B B$ ). The influence of Landau levels and Zeeman splitting might also affect the sign of the Hanle and inverted Hanle curves. In this case, the sign of spin polarization should be sensitive to the variation of channel thickness as quantum confinement plays a more important role.<sup>75</sup> Future

experiments are required to explore the physical origins of the sign change of the Hanle as well as the inverted Hanle signal. In particular, the influence of a thickness variation of the highly doped surface Ge layer could be investigated, and spin injection from polycrystalline and single-crystalline  $\text{Mn}_5\text{Ge}_3\text{C}_x$  contacts could be compared.

**Figure 3-7(a)** shows the Hanle signal and the related Lorentzian fitting at 2 K. The amplitude of the Hanle signal decreases with increasing temperature, as shown in **Figure 3-7(b)**, and no Hanle signal is observed for temperatures above 10 K. We extract the spin lifetime  $\tau_s$  by fitting the data with Lorentzian curves according to:

$$\Delta V = \frac{\Delta V_0}{1 + (\omega_L \tau_s)^2} = \frac{\Delta V_0}{1 + \left( B \frac{\tau_s g \mu_B}{\hbar} \right)^2} = \frac{\Delta V_0}{1 + \left( \frac{B}{\Delta B} \right)^2} \quad (3-5)$$

where  $\omega_L = g\mu_B B / \hbar$  is the Larmor frequency,  $\mu_B$  is the Bohr magneton,  $g = 1.6$  is the Landé factor,<sup>30</sup> and  $\hbar = h / 2\pi$  ( $h$ : Planck constant). Spin accumulation is reduced by 50% at the point where  $B = \Delta B = \hbar / g\mu_B \tau_s$ , i.e., we can obtain the spin lifetime from the full width at half maximum  $\Delta B$ . The temperature dependent spin lifetimes below 10 K are shown in **Figure 3-7(c)**. We find that the spin lifetime of 38 ps at 10 K from our sample is comparable to that of 35 ps at 10 K reported in Jain's work,<sup>84</sup> in which the spin injection was investigated in a three terminal geometry using a Co/permalloy/ $\text{Al}_2\text{O}_3/n^+$ -Ge tunnel contact. Because the magnetostatic stray-fields from surface roughness induces artificial broadening of the Hanle peaks,<sup>42</sup> the spin lifetime extracted from the width of the Hanle signal has to be taken as a lower bound.

Considering about spin relaxation in Ge, the Elliott-Yafet mechanism can be expected to dominate the spin transport in  $n$ -Ge.<sup>30</sup> In a degenerately doped group- $IV$  system, the Elliott-Yafet spin relaxation time is proportional to the momentum relaxation time  $\tau_{EF} \propto \tau_p^{-1}$ , and the momentum relaxation time could be further extracted from the Hall measurements:

$$\mu_e(T) = q\tau_p(T) / m_{e,Ge}^* \quad (3-6)$$

where  $\mu_e$  is Hall mobility,  $q$  is electron charge, and  $m_{e,Ge}^*$  is the effective electron mass in Ge. For our samples,  $\tau_p$  is weakly dependent on the temperature while  $T < 10$  K (see **Figure 3-7(c)**), because the Hall mobility is almost constant with  $\mu_e(T) \sim 400 \text{ cm}^2 / \text{V} \cdot \text{s}$  for  $T < 10$  K, as shown in the inset of **Figure 3-7(c)**. Consequently, the weak temperature dependence of spin lifetime is consistent with measurements of the Hall mobility for  $T < 10$  K. The reason that spin injection is only possible at very low temperatures can have two reasons. On the one hand, the high concentration of dopants can induce significant ionized impurity scattering particularly at low temperatures. On the other hand, the threading dislocations in the Ge channel can suppress spin lifetimes at all temperatures.

Furthermore, the spin diffusion length could be estimated from the spin lifetime  $l_{sf} = \sqrt{D(T)\tau_s}$ , where  $D(T)$  is the temperature-dependent electron diffusion coefficient. In our degenerately doped Ge,  $D(T)$  could be estimated from Hall mobility according to:<sup>85</sup>

$$D(T) = \frac{2}{3q} (E_F - E_C) \cdot \mu_e(T) \quad (3-7)$$

where we approximate

$$E_F - E_C = \frac{1}{m_{e,Ge}^*} \left( \frac{3 \pi^2 \hbar^3}{2 \sqrt{2}} N_D \right)^{2/3} = 142.8 \text{ meV} \quad (3-8)$$

at  $T = 0$  K, using  $N_D = 1 \times 10^{20} \text{ cm}^{-3}$  and  $m_{e,Ge}^* = 0.55 m_{e,0}$ . Taking into account the Hall mobility data in the inset of **Figure 3-7(c)**, we obtain a temperature-dependent diffusion coefficient of  $D = 37.5 \text{ cm}^2/\text{s}$  for electrons in the  $n^+$ -Ge layer and a corresponding spin diffusion length of  $l_{sf} = 397 \text{ nm}$  at  $T = 2$  K. This result suggests that, even though the spin lifetime is only tens-of-ps, the spin-diffusion length is sufficiently large for device applications from the benefit of large diffusion coefficient in the Ge channel.

To sum up, we experimentally observed a Hanle signal in a  $\text{Mn}_5\text{Ge}_3\text{C}_{0.8}/\text{Al}_2\text{O}_3/n^+$ -Ge-system on a Si (111) wafer, indicating that spin injection can be achieved in degenerately doped Ge channels that are integrated on Si wafer. For future spintronic device applications, this provides the possibility of using high-mobility Ge channels in a CMOS-compatible process flow. Although the spin lifetimes are low (38 ps at 10 K), Hall measurements let us conclude that spin transport in these channels is possible over distances larger than 100 nm, *i.e.* on length scales that are relevant for future device operation. Although the spin signal is only observable at low temperature ( $T < 10$  K), we expect to increase this temperature in future experiments by adjusting the doping concentration and improving the Ge layer quality.

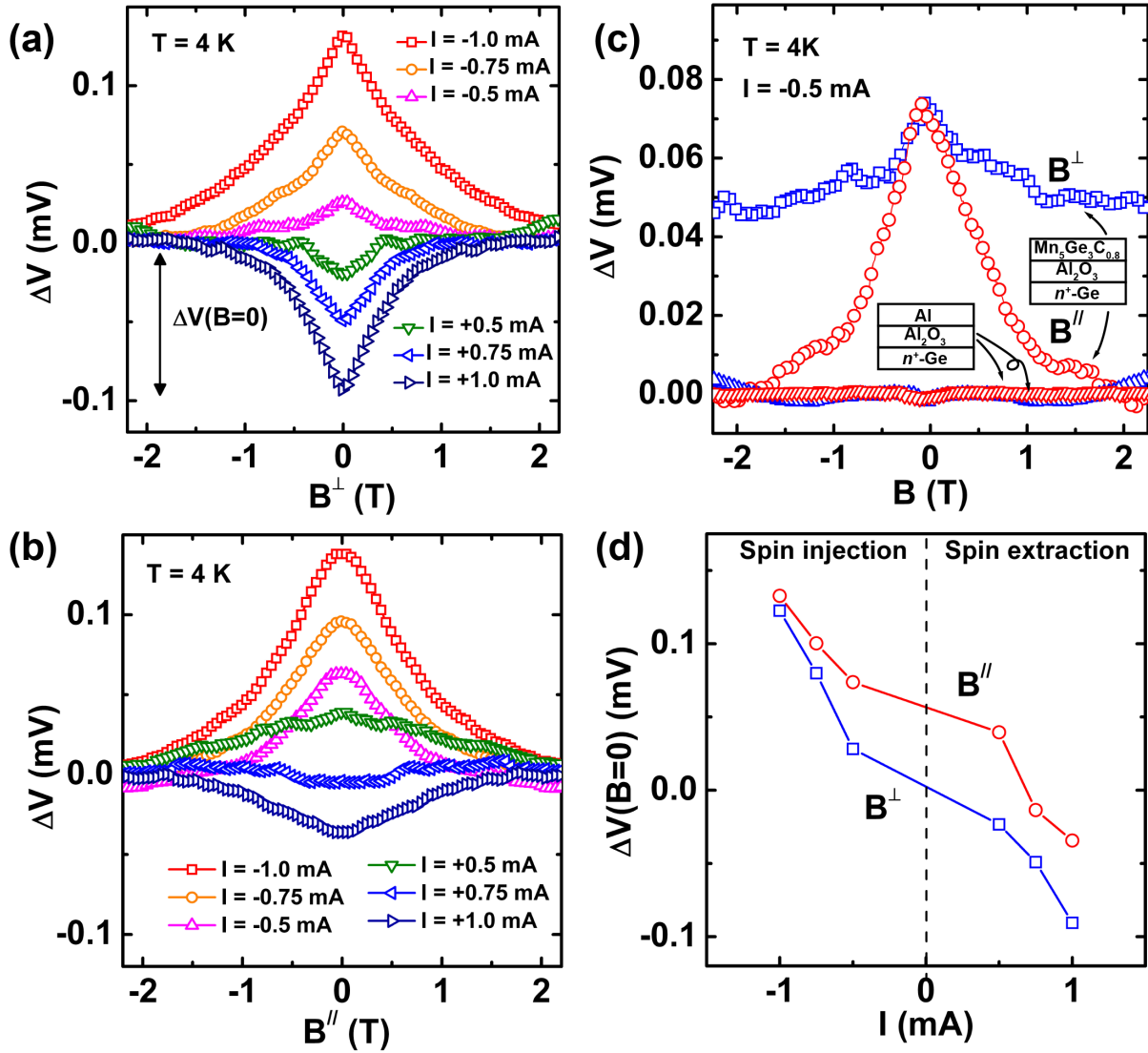


**Figure 3-6.** 3T Hanle and inverted Hanle effect measurements at 4 K. Measured voltage signals  $\Delta V$  under the magnetic fields (a)  $B^\perp$  and (b)  $B^\parallel$  at  $T = 4$  K for various spin injection and extraction conditions. (c)  $\Delta V$  at  $T = 4$  K and  $I = -0.5$  mA of  $\text{Mn}_5\text{Ge}_3\text{C}_{0.8}/\text{Al}_2\text{O}_3/n^+\text{-Ge}$  and of the  $\text{Al}/\text{Al}_2\text{O}_3/n^+\text{-Ge}$  reference sample. (d) Peak voltage  $\Delta V(B=0)$  as a function of the applied current.

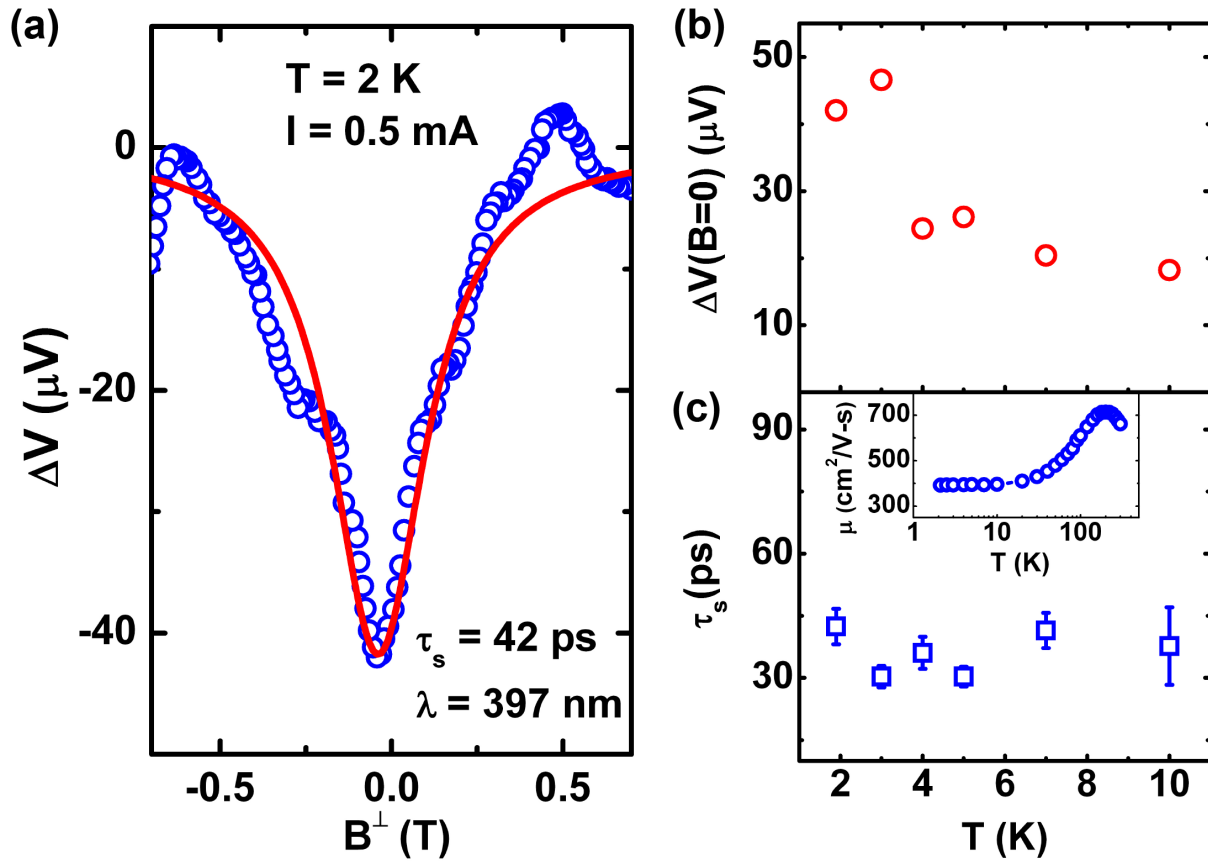


**Figure 3-7.** Temperature-dependent Hanle effect measurements and extracted spin lifetime. (a) Hanle signal at  $T = 2\text{ K}$  and  $I = 0.5\text{ mA}$  with Lorentzian fit (red line) to the data. (b) Peak voltage as a function of temperature. (c) Spin lifetime extracted from Lorentzian fitting for temperatures between  $2\text{ K}$  and  $10\text{ K}$ . The inset shows the temperature-dependent Hall mobility of the same  $n^+$ -Ge sample in a semi-logarithmic plot.



### 3.4 Limit of the Traditional Approach

Since Schmidt<sup>33</sup> and Fert<sup>34</sup> pointed out the fundamental obstacle for electrical spin injection from a FM into a diffusive semiconductor (SC), extensive efforts have focused on the electrical detection of spin transport in GaAs,<sup>24,25</sup> Si,<sup>26,28,29</sup> and Ge.<sup>30</sup> In order to overcome conductivity mismatch problem<sup>33,34</sup> and rebuild the spin polarization at the FM/SC interface, one of the solutions is to fabricate a high quality tunnel contact by inserting an oxide between the FM and the SC. In particular, as shown in **Figure 3-4(d)**, the typical layer sequence of a tunnel contact for efficient spin injection is designed as:

FM/oxide/heavily doped surface layer/lightly doped channel layer

where the FM is used as spin aligner,<sup>20</sup> the oxide alleviates Fermi-level pinning problem<sup>86</sup> and increase spin injection efficiency,<sup>2</sup> the heavily doped surface layer leads to a sharp depletion region and thus reduce contact resistance,<sup>87</sup> and the lightly doped channel layer provides a potential reservoir for spin accumulation with minimal ionized impurity scattering.<sup>75</sup>

For this multiple layers structure, the most critical part is a high quality tunnel oxide that possesses the following characteristics:<sup>88</sup> a uniform and well-controlled thickness, a minimal defect and trapped charge density, a good compatibility between the ferromagnetic metal and the SC channel, a minimal diffusion between the surrounding material at the temperature of device fabrication processing, and an optimized resistance-area product for efficient spin injection and detection efficiency. These requirements of the tunnel oxide increase the challenges of device fabrication. In addition, a common problem for the tunnel contact is a relatively large contact resistance-area product, which causes large power consumption and limits the device application.

Although an alternative is to build a reverse-biased FM Schottky contact,<sup>89-91</sup> care must be taken during device fabrication to prevent material intermixing and compound formation.

On the other hand, both FM tunnel and FM Schottky contacts require a heavily doped surface layer to reduce the contact resistance, but high density of ionized impurities cause significant ionized impurity scattering<sup>66</sup> that is unfavorable for spin transport.<sup>57</sup> As a result, for spin injection devices that built on a SC thin film, it is challenging to achieve a low contact resistance and a high-mobility channel at the same time. To overcome this problem, the high-mobility two-dimensional electron gas (2DEG) confined in a modulation doped quantum well structure (MODQW) might provides a major breakthrough in this area, because it possess a high-mobility channel as well as a high carrier density.

# Chapter 4 Electrical Detection of Spin Transport in Si

## 2DEG Systems

### 4.1 Introduction of the Spin Injection into Semiconductor-based 2DEG System

Electrical detection of spin transport in a semiconductor (SC) channel is one of the key requirements to realize spintronics devices.<sup>1</sup> Among various SC materials, the high-mobility two-dimensional electron gas (2DEG) confined in a modulation doped quantum well structure (MODQW) is of particular interest for device applications. This is because the high mobility promises for a long spin diffusion length of coherent transport as well as large spin signal for easy sensing.<sup>2</sup> Meanwhile, the effective spin manipulation is achievable either by enhanced Rashba spin-orbit interaction from an asymmetric  $\mathcal{E}$ -field structure,<sup>3,4</sup> or by direct control of discrete density of states (DOS) within the quantum well structure.<sup>5,6</sup> Despite of these merits, very few studies of direct electrical spin injection into 2DEG have been reported so far, mainly because of the difficulty in making reliable ferromagnetic (FM) contacts to the buried 2DEG channel. Only recently, Oltcher *et al.*<sup>8</sup> reported electrical spin injection into a high-mobility 2DEG channel confined at an (Al,Ga)As/GaAs interface. They showed a giant spin signal while the device dimensions were comparable to the mean free path ( $l_{mfp}$ ), and claimed that such a huge signal, which greatly exceeds the expectations from the standard spin drift-diffusion model,<sup>33,34,92</sup> was due to spin transport in the ballistic regime.

For the last decade, although there have been successful demonstrations of electrical spin injection into thin films of GaAs,<sup>24,25</sup> Si,<sup>26,28,60</sup> and Ge,<sup>30</sup> using tunnel contacts to overcome the conductivity mismatch problem,<sup>33,34,92</sup> it is still challenging to fabricate a reliable FM tunnel contact to the buried 2DEG in MODQW. In literature, only a few reports in Si/SiO<sub>2</sub><sup>6</sup> and III-V matrices<sup>4,7,8</sup> are available up to now; however, electrical detection of spin transport in the high-mobility 2DEG in a Si/SiGe MODQW has not been reported. To make continuous progress of Si-based spintronics and to take full advantage of current CMOS technology, there is an urgent need to develop Si-based spintronics devices.<sup>9,10</sup> In this chapter we demonstrate electrical detection of spin transport in the 2DEG in a Si/SiGe MODQW using FM Mn-germanosilicide (Mn(Si<sub>0.7</sub>Ge<sub>0.3</sub>)<sub>x</sub>) end contacts, which is a new approach to circumvent the difficulty of etching process adopted for the typical spin valve devices.<sup>4,8</sup> The experiments show that the spin-polarized electrons could be laterally injected into one side of the 2DEG confined at the Si/SiGe interface, and subsequently detected from the other side by the magnetoresistance (MR) of a FM/2DEG/FM spin valve. In what follows, we present a comprehensive material and device analysis, including TEM characterization of the Mn(Si<sub>0.7</sub>Ge<sub>0.3</sub>)<sub>x</sub> end contact, anomalous Hall effect (AHE) measurements of a single FM Mn(Si<sub>0.7</sub>Ge<sub>0.3</sub>)<sub>x</sub> contact, temperature-dependent contact resistance-area (RA) product of the Mn(Si<sub>0.7</sub>Ge<sub>0.3</sub>)<sub>x</sub> end contact, and low-temperature Hall measurements of the Si/SiGe MODQW. Most important of all, symmetric resistance steps were clearly observed from a series of FM/2DEG/FM spin valve devices with different channel lengths ( $L_{ch} = 1.5\sim 3.5 \mu\text{m}$ ), by which the spin diffusion length and spin lifetime are calculated to be  $l_{sf} = 4.5 \mu\text{m}$  and  $\tau_s = 16 \text{ ns}$  at 1.9 K, respectively.

## 4.2 MBE Growth of the Sb $\delta$ -doped Si/SiGe MODQW

Experiments were carried out starting from a Sb  $\delta$ -doped Si/SiGe MODQW. **Figure 4-1(a)** shows the cross section of the layer sequence. The whole structure was grown by solid-source molecular beam epitaxy (MBE) on a Si (111) substrate.<sup>93,94</sup> Firstly, an initial Si layer with a thickness of 50 nm was grown as the starting layer to cover remaining surface contaminants, followed by the growth of a 50 nm-thick Si<sub>0.95</sub>Ge<sub>0.05</sub> layer. Then the Ge content was linearly increased to 30% in a 1.5  $\mu$ m-thick graded buffer layer in order to accommodate the lattice mismatch between the substrate and Si<sub>0.7</sub>Ge<sub>0.3</sub>, and thus enable the subsequent growth of high-quality layers. On top of this buffer layer, a 500 nm-thick Si<sub>0.7</sub>Ge<sub>0.3</sub> layer was grown, followed by a 10 nm-thick strained Si layer (Si channel). After that, another 5 nm-thick Si<sub>0.7</sub>Ge<sub>0.3</sub> layer was grown to separate the doping region from the Si channel. The Sb  $\delta$ -doping and the final 45 nm-thick Si<sub>0.7</sub>Ge<sub>0.3</sub> layer was achieved by a pre-established technique, *i.e.* 1/20 monolayer of Sb was deposited prior to the overgrowth of Si<sub>0.7</sub>Ge<sub>0.3</sub>. **Figure 4-1(b)** shows the simulated conduction band diagram (lower axis) as well as carrier density (upper axis), in which the 2DEG is located in the quantum well inside the Si channel layer. As shown in **Fig. 4-1(c)**, the depth profiles of the Sb concentration (left axis) and Si, Ge composition (right axis) were confirmed by secondary ion mass spectrometry (SIMS) that was carried out by Evans Analytical Group. Besides, these data were used to simulate the conduction band diagram in **Fig. 4-1(b)** by solving the one-dimensional Poisson and Schrödinger equations self-consistently along the Z-axis.<sup>74</sup> It is important to note that the Sb  $\delta$ -doping was intentionally used to increase the 2DEG carrier concentration<sup>95,96</sup> in order to reduce contact resistance as well as minimize conductivity

mismatch problem<sup>33,34,92</sup>; however, the  $\delta$ -doping also induced a parasitic channel in the Si/SiGe MODQW. Therefore, its contribution to transport measurements will be carefully considered in the following characterizations.

We had successfully grown high-quality Si/SiGe MODQW on Si (100) substrate<sup>94</sup> that the Hall mobility at 4 K reaches as high as  $100,000 \text{ cm}^2 \text{ V}^{-1} \text{ s}^{-1}$ ; however, since the surface potential of Si (111) substrate is different from Si (100), the MBE growth protocols should be modified for the growth on a Si (111) substrate. **Table 4-1** summarizes the MBE growth protocols for six samples (A4051-4200), in which the substrate temperatures are gradually increased from A4051 to A4200. **Figures 4-1(d)** and **(e)** show high-resolution TEM images of the two selected samples A4053 and A4200. It is noted that the sharp contrast among the different layer in A4200 suggests that the defect densities are significantly suppressed at higher substrate temperature. To further confirm the transport properties, low temperature Hall measurements were carried out for the six Si/SiGe MODQW samples. **Figure 4-2** shows Hall mobility as a function of temperature for A4051, A4052, A4053, A4197, A4198, and A4200. It is important to see that the mobilities of the first sets of samples (A4051, A4052, and A4053) drop at low temperature ( $T < 100 \text{ K}$ ). It is a standard bulk-property that the Sb-doped layer dominates the carrier transport in Si/SiGe MODQW, and therefore the mobility is limited by the ionized impurity scattering at low temperature. On the contrary, the mobilities of the last sets of samples (A4197, A4198, and A4200) continue to increase at low temperature ( $T < 100 \text{ K}$ ). It is a standard 2DEG-property that the high-mobility 2DEG dominates the carrier transport in Si/SiGe MODQW, in which the channel is separated from the ionized dopants by the spacer layer, and therefore the ionized

impurity scattering is significantly minimized. In the following sections, we will focus on sample A4200 for all of the device fabrication and characterization.

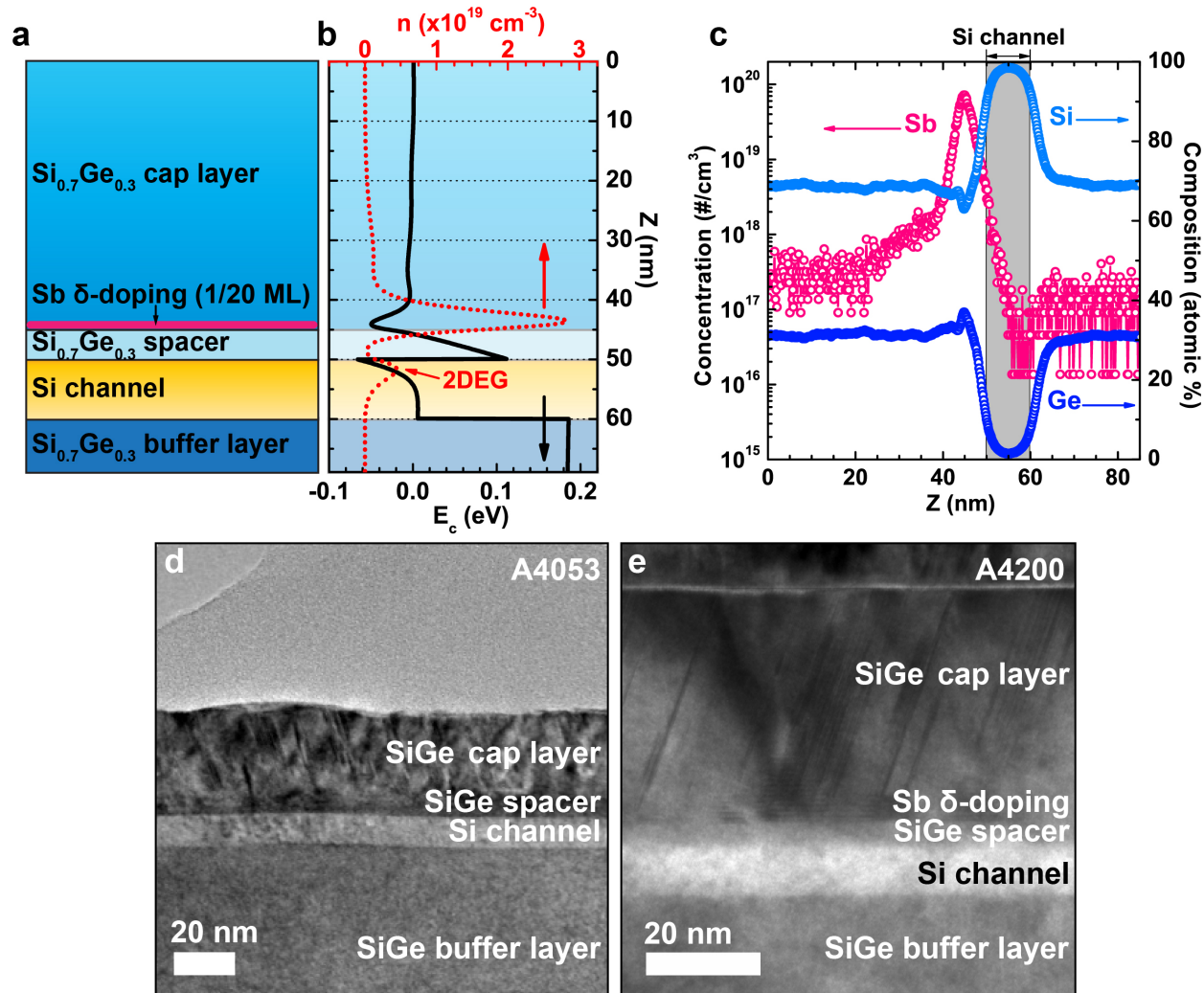


**Figure 4-1.** Material developments for the Sb  $\delta$ -doped Si/SiGe MODQW on Si (111) (a) Cross section of the Sb  $\delta$ -doped Si/SiGe MODQW structure. (b) The simulated conduction band diagram (lower axis) and carrier density (upper axis) at 1.9 K. (c) SIMS spectra of Sb concentration (left axis), and Si, Ge composition (right axis), respectively. It is noted that the SIMS detection limit of Sb concentration is about  $1 \times 10^{17} \text{ cm}^{-3}$ , so the real Sb concentration in the SiGe cap layer and the SiGe buffer layer could be much lower. (d) High-resolution TEM images of the as-grown A4053. (e) High-resolution TEM images of the as-grown A4200.



**Table 4-1.** Substrate temperature during MBE growth for the Sb  $\delta$ -doped Si/SiGe MODQW

<b>Sample #</b>	<b>A4051</b>	<b>A4052</b>	<b>A4053</b>	<b>A4197</b>	<b>A4198</b>	<b>A4200</b>
<b>Si<sub>0.7</sub>Ge<sub>0.3</sub> Cap layer</b>	330 °C	330 °C	330 °C	380 °C	400 °C	400 °C
<b>Sb <math>\delta</math>-doping layer</b>	330 °C	330 °C	330 °C	380 °C	400 °C	400 °C
<b>Si<sub>0.7</sub>Ge<sub>0.3</sub> Spacer layer</b>	620 °C	640 °C	660 °C	660 °C	660 °C	680 °C
<b>Si Channel layer</b>	620 °C	640 °C	660 °C	660 °C	660 °C	680 °C
<b>Si<sub>0.7</sub>Ge<sub>0.3</sub> Buffer layer</b>	620 °C	640 °C	660 °C	660 °C	660 °C	680 °C

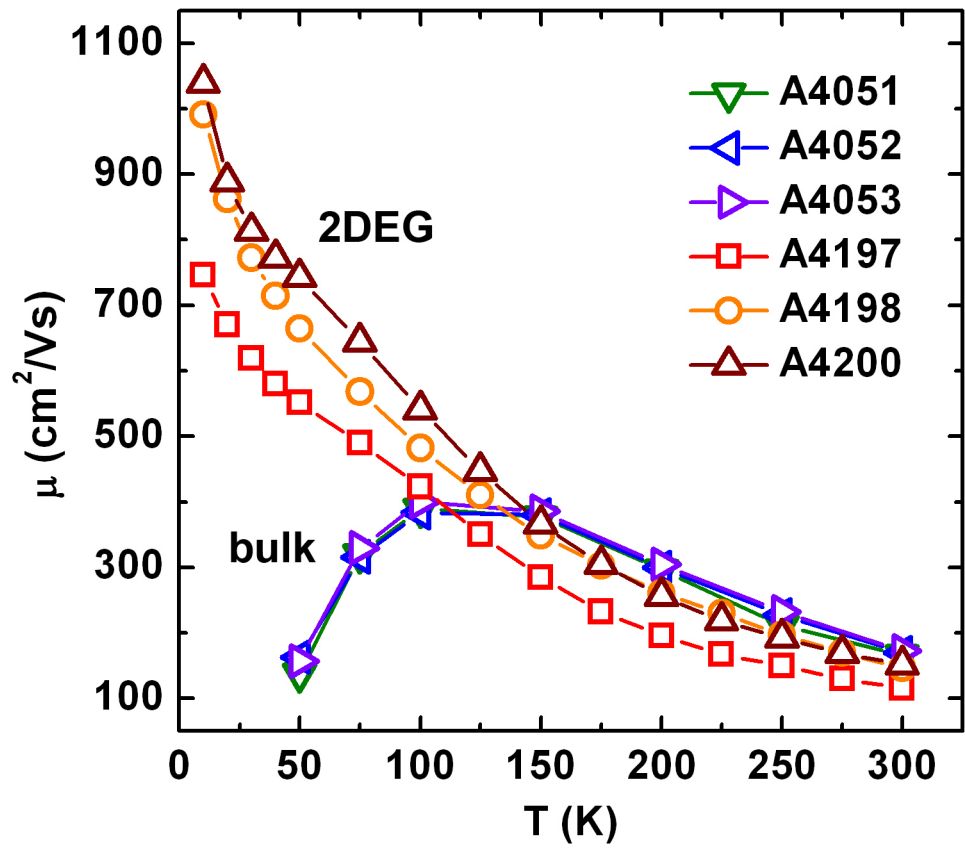


**Figure 4-2.** Hall mobilities as a function of temperature for the six samples A4051-A4200.

### 4.3 Device Fabrication for the Si/SiGe MODQW

**Figure 4-3(a)** shows a typical device image, in which a 100 nm-thick SiO<sub>2</sub> layer fully covers the mesa and substrate except for five open windows for Mn(Si<sub>0.7</sub>Ge<sub>0.3</sub>)<sub>x</sub> contacts. Five pairs of Ti/Au electrodes are connected to the upper (1-5) and lower (10-6) ends of Mn(Si<sub>0.7</sub>Ge<sub>0.3</sub>)<sub>x</sub> contacts for magneto-transport measurements. **Figure 4-3(b)** illustrates the configuration for spin transport measurements: by flowing a current between contacts 2 and 5, spin-polarized electrons are laterally injected into the 2DEG from the FM Mn(Si<sub>0.7</sub>Ge<sub>0.3</sub>)<sub>x</sub> end contact, and the voltage is sensed between contacts 3 and 4. Though the parasitic channel from the Sb  $\delta$ -doping contributes to the background signal in the MR, the spin polarization in the parasitic channel is randomized before reaching the contact 4, because of the severe spin relaxation from high density of ionized impurity charge.<sup>31,57,88</sup> The spin diffusion length was reported to be about 190 nm when the doping level was as high as  $3 \times 10^{19} \text{ cm}^{-3}$  in Si<sup>57,88</sup>, which is much shorter than the channel length of 1.5  $\mu\text{m}$  in our device. Consequently, in this case, the MR of the FM/2DEG/FM spin valve between contacts 3 and 4 could be measured using a standard four-terminal setup.

Because quantum confinement in the Si/SiGe MODQW is sensitive to the surface potential of the SiGe cap layers, the 2DEG could be depleted after destructive etching process adopted in the previous approaches.<sup>4,8</sup> To protect the high-mobility 2DEG channel during device fabrication, we developed a Mn solid-state reaction process<sup>97,98</sup> for the Si/SiGe MODQW, aiming to fabricate FM Mn(Si<sub>0.7</sub>Ge<sub>0.3</sub>)<sub>x</sub> end contacts to the 2DEG. The device fabrication started with a mesa isolation (80 nm-height) by a reactive ion etching (RIE), and then a 100 nm-thick SiO<sub>2</sub> layer was deposited using plasma-enhanced chemical vapor deposition (PECVD) to

passivate the surface. The contact windows (sizes of  $10 \times 20$  and  $5 \times 20 \mu\text{m}^2$ ) were patterned by photolithography (PL) and structured by RIE and wet chemical etching. After removing all the photoresist residual (PR), a 150 nm-thick Mn layer was deposited on the patterned sample with e-beam evaporation, immediately followed by rapid thermal annealing (RTA) at 360 °C for 2 minutes. During the annealing,  $\text{Mn}(\text{Si}_{0.7}\text{Ge}_{0.3})_x$  only formed inside the contact windows, while other regions were protected by the 100 nm-thick  $\text{SiO}_2$  mask. The remaining unreacted Mn layer was removed by wet etching (see also **Fig. 4-3(c)**). Finally, metallization was accomplished by metal deposition of Ti/Au (50/100 nm) to connect electrodes into the  $\text{Mn}(\text{Si}_{0.7}\text{Ge}_{0.3})_x$  contact windows. In the above process flow, the most critical step is the rapid thermal annealing that drives Mn to diffuse into the SiGe cap layer, in which the annealing temperature should be chosen carefully so as to form FM  $\text{Mn}(\text{Si}_{0.7}\text{Ge}_{0.3})_x$  contact<sup>97,98</sup> but not to affect the doping profile of the Si/SiGe MODQW. Also, rather than using a Si (100) substrate, the (111) crystal orientation is chosen to improve the crystallinity of the formed  $\text{Mn}(\text{Si}_{0.7}\text{Ge}_{0.3})_x$  upon annealing.<sup>32,99</sup> Previously we show that the formed  $\text{Mn}_5\text{Ge}_3$  on a Si (111) substrate behaves like a ferromagnetic “bad metal”, whose conductivity is comparable to that of highly doped Ge;<sup>32,73</sup> accordingly, we do not expect a serious conductivity mismatch at the  $\text{Mn}(\text{Si}_{0.7}\text{Ge}_{0.3})_x/\text{Si}$  interface. By measuring two devices on Si (100) and (111) substrates with  $\text{Mn}(\text{Si}_{0.7}\text{Ge}_{0.3})_x$  end contacts with transfer length method (TLM), **Fig. S2** shows that the RA product of the device on Si (111) substrate at 10 K is almost two orders of magnitude smaller than that on Si (100) substrate.

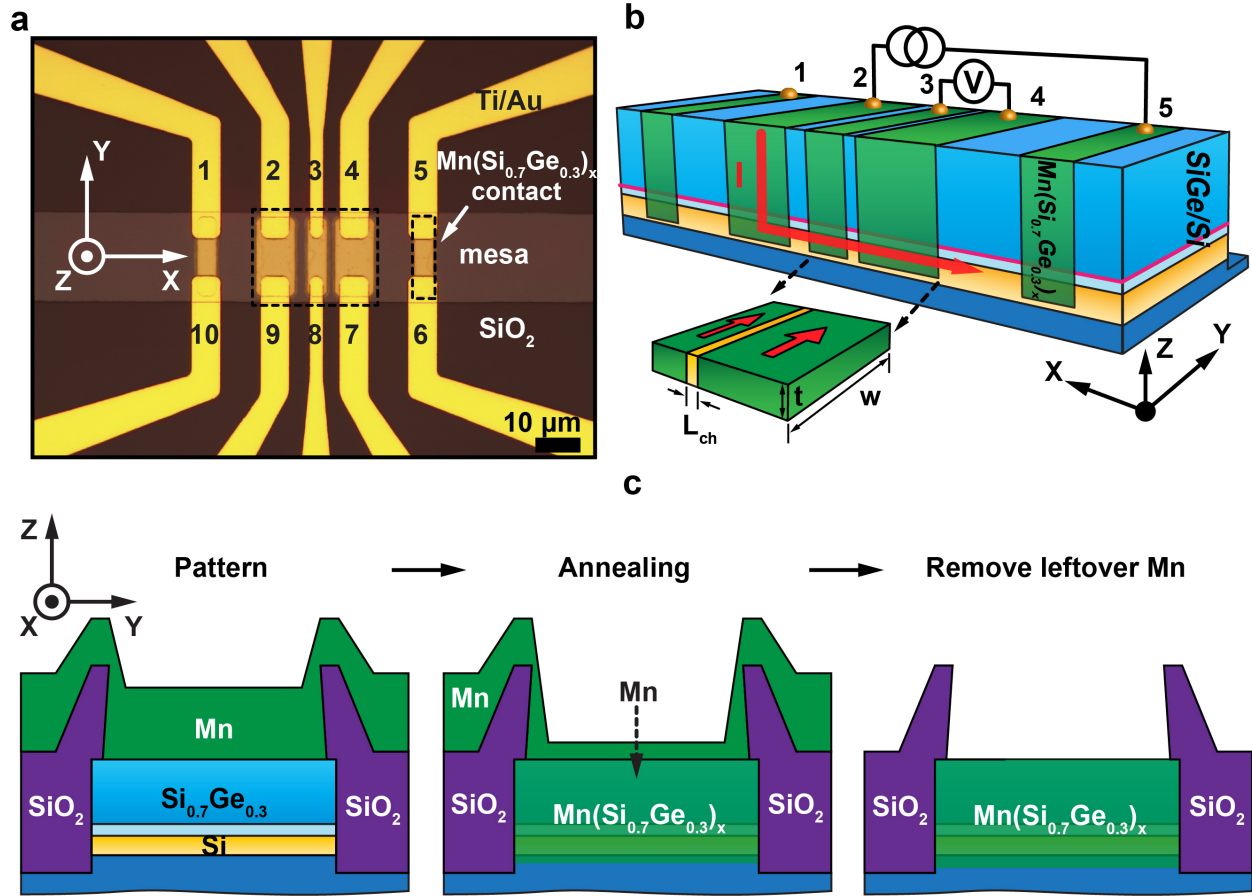


**Figure 4-3.** Schematics of the Si/SiGe MODQW device structure and the contact process. (a) Optical microscope (OM) image of a typical fabricated device, where various dash rectangles highlight the position of FM  $\text{Mn}(\text{Si}_{0.7}\text{Ge}_{0.3})_x$  contacts. (b) Schematics of the measurements configuration for electrical detection of spin transport in the 2DEG. The MR of the FM/2DEG/FM spin valve with a channel length ( $L_{ch}$ ) could be obtained using a standard four-terminal setup. (c) Reactive ion etching (RIE) and wet chemical etching are used to pattern  $\text{SiO}_2$  contact window, followed by Mn deposition (left). During rapid thermal annealing, Mn diffuses into the Si/SiGe modulation doped quantum well structure (MODQW) and forms  $\text{Mn}(\text{Si}_{0.7}\text{Ge}_{0.3})_x$  (middle). Leftover Mn is removed by wet chemical etching. The clean  $\text{Mn}(\text{Si}_{0.7}\text{Ge}_{0.3})_x$  surface is

ready for final metallization and transport measurements (right). It is important to note that surface cleaning before Mn deposition is the most critical step, since oxide residual could block Mn diffusion.

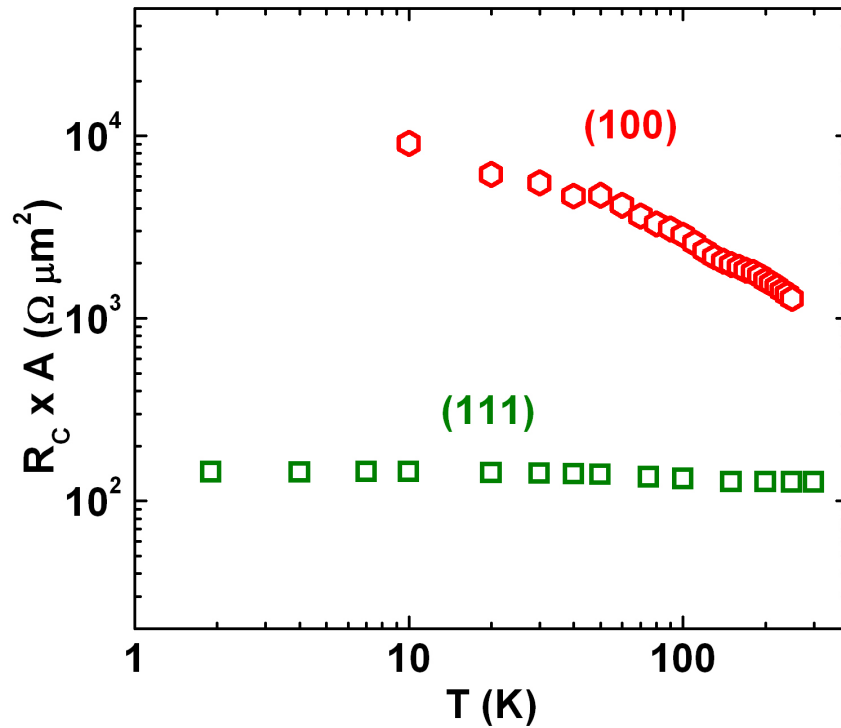


**Figure 4-4.** Effects of (100) and (111) crystal orientation on the contact properties. Comparison of  $\text{Mn}(\text{Si}_{0.7}\text{Ge}_{0.3})_x$  side contact resistance area products (RA) as a function of temperature between two devices measured with a transfer length method (TLM): the red diamonds are measured from the TLM device on Si (100) substrate, and the green squares are from the TLM device on Si (111), respectively. It is clear to see that the RA product of the TLM device on Si (111) substrate is smaller by at least one order of magnitude than that on Si (100) in the entire

temperature range of  $T = 10\sim 300$  K. The weak temperature dependence also suggests the formed  $\text{Mn}(\text{Si}_{0.7}\text{Ge}_{0.3})_x$  yields a sharp Schottky contact to the Si/SiGe MODQW.

#### 4.4 Structure Characterization of the Si/SiGe MODQW and Mn(Si<sub>0.7</sub>Ge<sub>0.3</sub>)<sub>x</sub>

**Figure 4-5** exhibits the structural characterization of the Si/SiGe MODQW and Mn(Si<sub>0.7</sub>Ge<sub>0.3</sub>)<sub>x</sub> contacts. A field-emission TEM (JEM-3000F), operated at 300 kV with a point-to-point resolution of 0.17 nm, was used to obtain the epitaxial relationships. **Figure 4-5(a)** shows a high-resolution TEM image of an as-grown Si/SiGe MODQW, in which the sharp contrast among the SiGe cap layer, SiGe spacer, Si channel, and SiGe buffer layer confirms the high quality heterostructure. **Figure 4-5(b)** shows a low-magnification TEM image on a specific device. Considering the high temperature annealing process during device fabrication may affect the Si/SiGe MODQW, the TEM sample is directly cut from a device using a focused ion beam (FIB) to double-check the crystal structure. The center part of the device image in **Figure 4-3(a)** is shown in the inset of **Figure 4-5(b)**, in which the double-headed arrow indicates the FIB sample position. In the cross section image, the edge of SiO<sub>2</sub> layer tilts up due to the mismatched thermal expansion coefficient during annealing. For the right part without the SiO<sub>2</sub> protection, the dark area in the SiGe cap layer indicates the formation of Mn(Si<sub>0.7</sub>Ge<sub>0.3</sub>)<sub>x</sub>. Further zooming in the white square, a high-resolution TEM image in **Figure 4-5(c)** shows that Mn diffuses into the SiGe cap layer upon annealing, and the solid-state reaction is controlled to stop at the Si channel layer. More importantly, the crystalline structure of the Si channel layer is well preserved after the fabrication process.

To examine the material phase of the formed Mn(Si<sub>0.7</sub>Ge<sub>0.3</sub>)<sub>x</sub>, the high-resolution TEM images in **Figures 4-5(d)** and **(e)** correspond to the Mn<sub>5</sub>(Si<sub>0.7</sub>Ge<sub>0.3</sub>)<sub>x</sub> and Si regions, respectively. Further, **Figures 4-5(f)** and **(g)** are the FFT-diffraction patterns from two marked regions of



**Figure 4-5(c)**, revealing the epitaxial relationship to be:  $\text{Mn}_5(\text{Si}_{0.7}\text{Ge}_{0.3})_3 [02\bar{1}] // \text{Si} [\bar{1}12]$  and  $\text{Mn}_5(\text{Si}_{0.7}\text{Ge}_{0.3})_3 (212) // \text{Si} (\bar{1}\bar{3}1)$ . The formed  $\text{Mn}_5(\text{Si}_{0.7}\text{Ge}_{0.3})_3$  has a hexagonal structure<sup>100</sup> (space group  $P6_3/mcm$ ) with lattice constants:  $a_{\text{hex}} = 6.912 \text{ \AA}$  and  $c_{\text{hex}} = 4.812 \text{ \AA}$ . The lattice spacings for  $\text{Mn}_5(\text{Si}_{0.7}\text{Ge}_{0.3})_3 (212)$  and  $\text{Si} (\bar{1}\bar{3}1)$  planes are determined to be  $d_{212} = 1.64 \text{ \AA}$  and  $d_{\bar{1}\bar{3}1} = 1.64 \text{ \AA}$ , which results in a good epitaxial growth between  $\text{Mn}_5(\text{Si}_{0.7}\text{Ge}_{0.3})_3$  and Si.

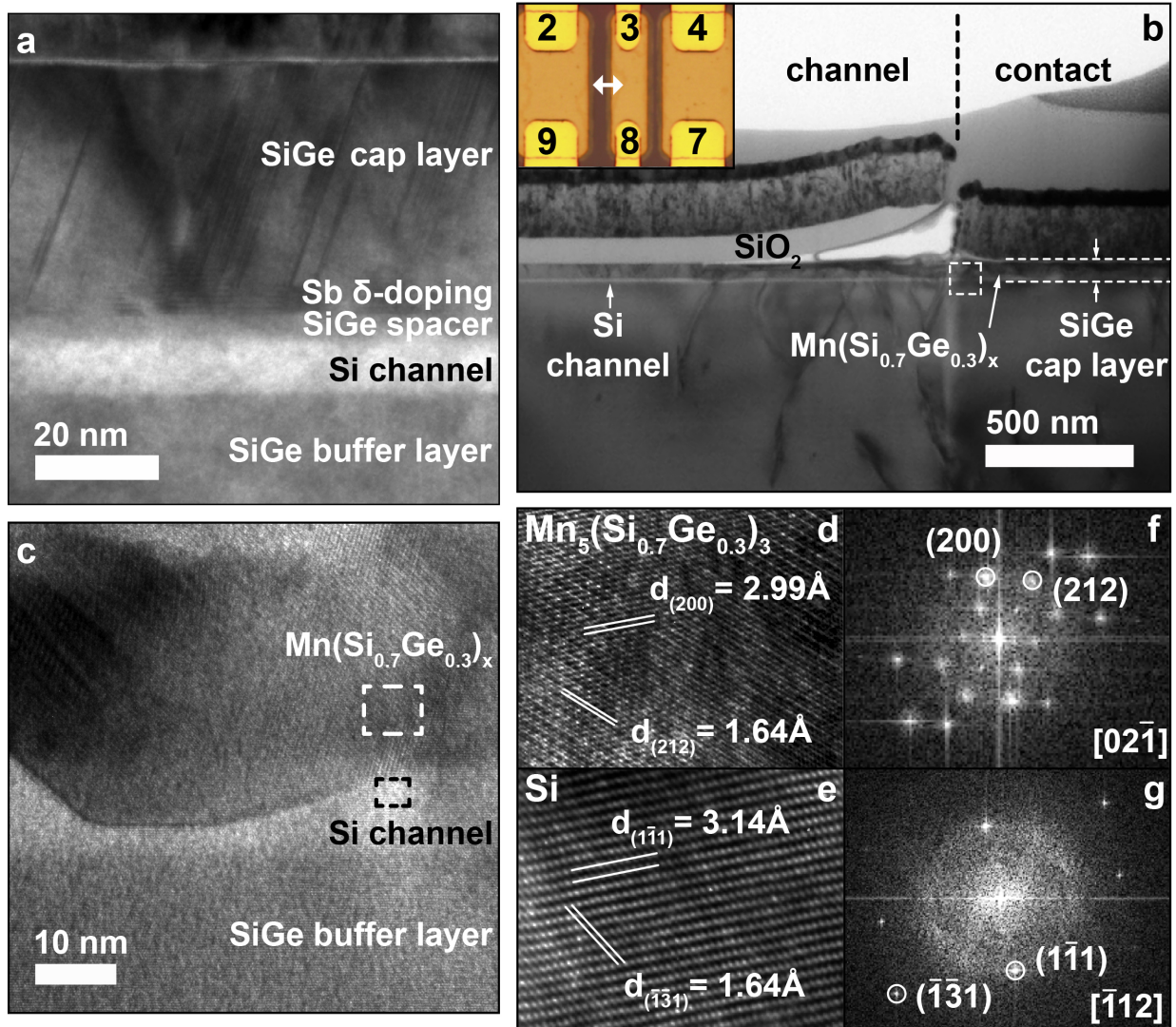


**Figure 4-5.** Structure characterization of Si/SiGe MODQW and  $\text{Mn}(\text{Si}_{0.7}\text{Ge}_{0.3})_x$ . (a) High-resolution TEM image of the as-grown Si/SiGe MODQW. The sharp contrast between each layers confirm the high quality heterostructure. (b) Low-magnification TEM image on the edge of a  $\text{Mn}(\text{Si}_{0.7}\text{Ge}_{0.3})_x$  contact. The inset shows the center part of the device image and the FIB sample position. (c) High-resolution TEM image of the  $\text{Mn}(\text{Si}_{0.7}\text{Ge}_{0.3})_x/\text{Si}$  channel interface, as indicated by the white square in (b). It shows that Mn vertically diffuses into the SiGe cap layer and stops at the Si channel layer. (d,e) High-resolution TEM images taken in the  $\text{Mn}(\text{Si}_{0.7}\text{Ge}_{0.3})_x$

and the Si regions, respectively. (f,g) The corresponding FFT-diffraction patterns of  $\text{Mn}(\text{Si}_{0.7}\text{Ge}_{0.3})_x$  (Si) along  $[02\bar{1}]$  ( $[\bar{1}12]$ ) zone axis, respectively.

#### 4.5 Ferromagnetic Property of the Mn(Si<sub>0.7</sub>Ge<sub>0.3</sub>)<sub>x</sub>

The following two sections (4.5 and 4.6) summarize the low temperature magneto-transport characterizations to check the typical device properties, which were carried out in a Quantum Design physical property measurements system (PPMS). First of all, we confirm the ferromagnetism of the Mn(Si<sub>0.7</sub>Ge<sub>0.3</sub>)<sub>x</sub> at 1.9 K by measuring the AHE<sup>101,102</sup> of a single Mn(Si<sub>0.7</sub>Ge<sub>0.3</sub>)<sub>x</sub> contact. As shown in **Fig. 4-6(a)**, the measurements were carried out on a typical spin injection device, by applying a lateral current ( $I_{25}$ ) between contacts 2 and 5 and measuring a transverse voltage ( $V_{38}$ ) between contacts 3 and 8 (see Fig. 1d). The Hall resistance ( $R_{Hall} \equiv V_{38}/I_{25}$ ) could be simplified as a combination of ordinary and anomalous Hall components:  $R_{Hall}d = R_OH + R_A m_z$ , where  $d$  is the channel thickness,  $m_z$  is the magnetization component in the  $Z$ -axis, and  $R_O$  ( $R_A$ ) are the ordinary (anomalous) Hall coefficient, respectively. The AHE resistance ( $R_{AHE}$ ) is obtained by subtracting the linear ordinary Hall component from the  $R_{Hall}$ , as shown in the inset of **Fig. 4-6(a)**, whose linear background yields a carrier density of  $n = 2.5 \times 10^{20} \text{ cm}^{-3}$ , suggesting that the formed Mn(Si<sub>0.7</sub>Ge<sub>0.3</sub>)<sub>x</sub> behaves like a ferromagnetic bad metal. The angle-dependent measurements in **Fig. 4-6(b)** confirms that the easy axis of magnetization of the formed Mn(Si<sub>0.7</sub>Ge<sub>0.3</sub>)<sub>x</sub> is in in-plane direction along the  $Y$ -axis. Furthermore, temperature dependent AHE measurements in **Fig. 4-6(c)** were carried out to estimate the Curie temperature ( $T_C$ ), in which the corresponding Arrot's plot<sup>102,103</sup> in **Fig. 4-6(d)** shows that the  $T_C$  of Mn(Si<sub>0.7</sub>Ge<sub>0.3</sub>)<sub>x</sub> is higher than 150 K.

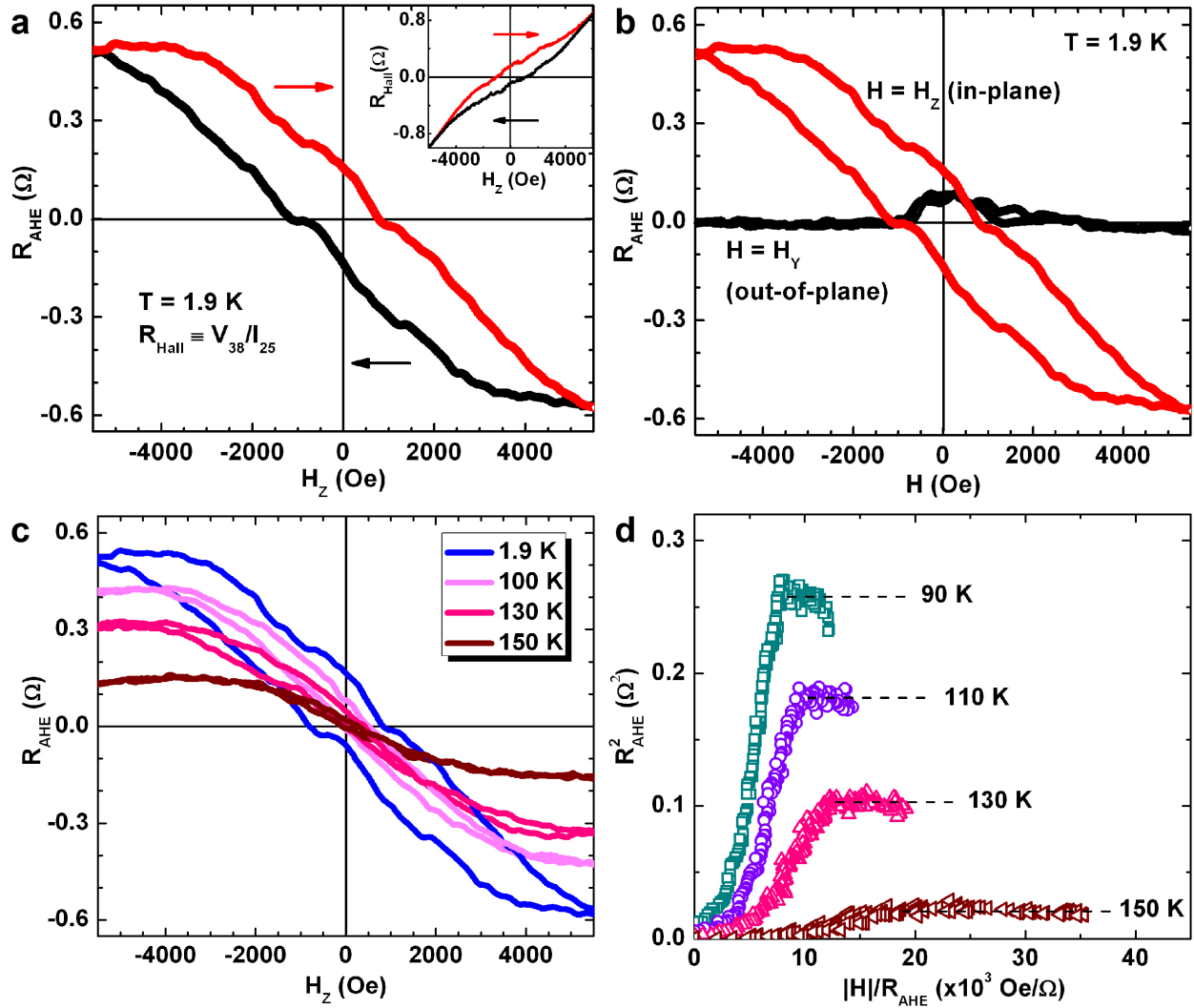


**Figure 4-6.** Anomalous Hall effect measurements of a single Mn(Si<sub>0.7</sub>Ge<sub>0.3</sub>)<sub>x</sub> contact. (a) The magnetization curves of  $R_{AHE}$  measured from a single FM Mn(Si<sub>0.7</sub>Ge<sub>0.3</sub>)<sub>x</sub> contact by sweeping an external magnetic field along the Z-axis ( $H_z$ ) at 1.9 K. The  $R_{AHE}$  is obtained by subtracting the ordinary Hall components from the  $R_{Hall}$ , as shown in the inset. (b) The magnetization curves of  $R_{AHE}$  under the magnetic field along the out-of-plane direction ( $H_z$ ) and in-plane direction ( $H_y$ ), respectively. In contrast to the slight  $R_{AHE}$  under  $H = H_y$ , the clear  $R_{AHE}$  loop under  $H = H_z$  shows that the easy axis of magnetization is along the in-plane direction. (c) The magnetization

curves of  $R_{AHE}$  of a single  $\text{Mn}(\text{Si}_{0.7}\text{Ge}_{0.3})_x$  contact at various temperatures  $T = 1.9\text{-}150$  K, in which the  $R_{AHE}$  is clearly observed up to 150 K. (d) The Arrot's plots under various temperatures  $T = 90\text{-}150$  K. Considering a simplified model that anomalous Hall coefficient ( $R_S$ ) is independent on the magnetic field, the  $R_{AHE}$  could be used to replace the  $M$  in the Arrott's plot<sup>102</sup> (that is  $M^2$  versus  $H/M$  plot). Because the dashed line at 150 K can not be extrapolated to intercept the origin point, it suggests that the  $T_C$  of  $\text{Mn}(\text{Si}_{0.7}\text{Ge}_{0.3})_x$  contact is higher than 150 K.<sup>103</sup>

## 4.6 Electrical Transport Characterization for the Si/SiGe MODQW Devices

To have a better understanding of the contact and 2DEG properties, a series of TLM and Hall bar devices were simultaneously fabricated with the spin injection devices on the same chip. Three kinds of TLM devices with spacing and area variants were used to examine the  $\text{Mn}(\text{Si}_{0.7}\text{Ge}_{0.3})_x$  end contact to the Si/SiGe MODQW. The dimension of the contact size was designed to be  $A_{top} = w \times w/2$ , where the width has three different values of  $w = 20, 60, \text{ and } 100 \mu\text{m}$ . Figure 3b shows the total resistance from two-terminal measurements ( $R_T$ ) as a function of channel length ( $d$ ) at 1.9 K. In the diffusive regime, while the channel length is much longer than the mean free path,  $R_T$  can be formulated as  $R_T = R_{sh}d/w + 2R_C$ , where  $R_{sh}$  is the sheet resistance of the channel,  $d/w$  is the aspect ratio of the channel, and  $R_C$  is the contact resistance. From the linear fitting of experimental data in **Fig. 4-7(a)**, we obtain  $R_{sh} = 3526, 4192, \text{ and } 4827 \Omega/\text{sq}$ ;  $R_C = 720, 281, \text{ and } 202 \Omega$  for  $w = 20, 60, \text{ and } 100 \mu\text{m}$  (green squares, red circles, and blue triangles), respectively. The extracted sheet resistances from three TLM devices with area variants show that the channel property is much better within smaller areas ( $R_{sh}$  reduces 27% by shrinking the width from 100 to 10  $\mu\text{m}$ ), which is consistent with the TEM image in **Fig. 4-5(b)** that there are some observable defects in the SiGe buffer layer.

On the other hand, because  $R_C$  is dependent on the contact size, in order to confirm the effective contact area and current path, we calculated the RA product from two different aspect ratios of contact area ( $A_{top}$  and  $A_{side}$ ), and plotted their temperature dependence in **Fig. 4-7(b)**. The top three sets (solid symbols) utilize top area  $A_{top} = w \times w/2$  and the bottom three sets (open

symbols) utilize side area  $A_{side} = w \times t$ , where  $t = t_{parasitic} + t_{2DEG} = 3.6 + 3.5 = 7.1$  nm is the sum of effective thickness of the parasitic ( $t_{parasitic}$ ) and 2DEG ( $t_{2DEG}$ ) channels estimated from the full width of half maximum of the carrier density in **Fig. 4-1(b)** (red dotted line). It is interesting to see that, from three different TLM devices, the RA products are normalized in the case of  $R_C \times A_{side}$ . Three bottom sets of RA product suggest that the  $Mn(Si_{0.7}Ge_{0.3})_x$  forms a end contact instead of surface contact to the Si/SiGe MODQW with the effective current path being illustrated in the inset of **Fig. 4-7(b)**. Meanwhile, since the RA product remains almost constant from  $T = 1.9$  to 300 K, the weak temperature dependence of the RA product also suggests that the formation of  $Mn(Si_{0.7}Ge_{0.3})_x$  yields an sharp Schottky end contact to the Si/SiGe MODQW.

In addition to TLM contact characterization, low-temperature Hall mobility is a crucial figure of merit to check overall quality of the Si/SiGe MODQW. **Figure 4-7(c)** shows the temperature dependence of the measured Hall mobility (left-axis) and sheet carrier density (right-axis), respectively. Although at room temperature the high-mobility 2DEG is screened by the parasitic channel due to phonon scattering,<sup>96</sup> the temperature dependence of mobility shows that the 2DEG starts to contribute when  $T < 100$  K, reaching the lowest sheet carrier density of  $n_H = 1.91 \times 10^{12}$  cm<sup>-2</sup> and the highest mobility of  $\mu_H = 865$  cm<sup>2</sup>/V·s at 1.9 K. However, the measured Hall mobility consists of a high mobility 2DEG channel as well as a parasitic channel introduced by the Sb  $\delta$ -doping, as can be seen from the simulation of the carrier density in **Fig. 4-1(b)**. For a better analysis, the contribution of the 2DEG channel could be extracted using a dual channel as follows:

$$\mu_H = \frac{n_1\mu_1^2 + n_2\mu_2^2}{n_1\mu_1 + n_2\mu_2}, \quad n_H = \frac{(n_1\mu_1 + n_2\mu_2)^2}{n_1\mu_1^2 + n_2\mu_2^2} \quad (4-1)$$



where  $n_1, \mu_1$  ( $n_2, \mu_2$ ) are sheet carrier density and mobility of the 2DEG (parasitic) channel, respectively. Accordingly, we extracted the mobility and sheet carrier density of the 2DEG as follows:

$$\mu_1 = \frac{n_H \mu_H^2 - n_2 \mu_2^2}{n_H \mu_H - n_2 \mu_2} \approx 1200 \text{ cm}^2/\text{V}\cdot\text{s}, \quad n_1 = \frac{(n_H \mu_H - n_2 \mu_2)^2}{n_H \mu_H^2 - n_2 \mu_2^2} \approx 9.6 \times 10^{11} \text{ cm}^{-2} \quad (4-2)$$

in which  $n_2 = 1 \times 10^{13} \text{ cm}^{-3}$  and  $\mu_2 = 49 \text{ cm}^2/\text{V}\cdot\text{s}$  is measured from a control sample that possesses the similar doping profile but without a 2DEG channel.

It is noted that the extracted 2DEG mobility ( $\mu_1 \approx 1200 \text{ cm}^2/\text{V}\cdot\text{s}$ ) is still two orders of magnitude smaller than that of a typical Si/SiGe MODQW reported by Ismail<sup>104</sup> ( $\mu \approx 4 \times 10^5 \text{ cm}^2/\text{V}\cdot\text{s}$ ). In addition to the substrate difference, the major mobility-limiting factor in our sample is probably due to remote impurity scattering<sup>94,105</sup> from the adjacent Sb dopants. It can be estimated using the model proposed by Monroe.<sup>105</sup>

$$\mu_{remote} \approx 16 \sqrt{\pi g_v g_s e n_s^3 d_{eff}} / \hbar N_{\square} = 4300 \text{ cm}^2/\text{V}\cdot\text{s} \quad (4-3)$$

in which  $g_v = 2$  is the valley degeneracy,  $g_s = 2$  is the spin degeneracy,  $\hbar = 6.58 \times 10^{-16} \text{ eV}\cdot\text{s}$  is the reduced Plank constant,  $d_{eff} = 8.1 \text{ nm}$  is the center-to-center distance between the impurity layer and the wave function in Si channel,  $n_s = n_1 = 9.6 \times 10^{11} \text{ cm}^{-2}$  is the sheet carrier density in the 2DEG channel, and  $N_{\square} = n_2 = 1.0 \times 10^{13} \text{ cm}^{-2}$  is the sheet carrier density of the impurity (parasitic channel). The mobility from remote impurity scattering model is slightly higher than that from the Hall measurements (4300 vs. 1200  $\text{cm}^2/\text{V}\cdot\text{s}$ ) because there are also other mobility-limiting mechanisms,<sup>105</sup> such as uniform background charges, alloy scattering, and

strain distribution. Importantly, this model suggests that the mobility could be further improved by carefully tuning the spacer thickness ( $d_{eff}$ ) and impurity concentration ( $N_{\square}$ ), which provides a useful guideline for future experiments.

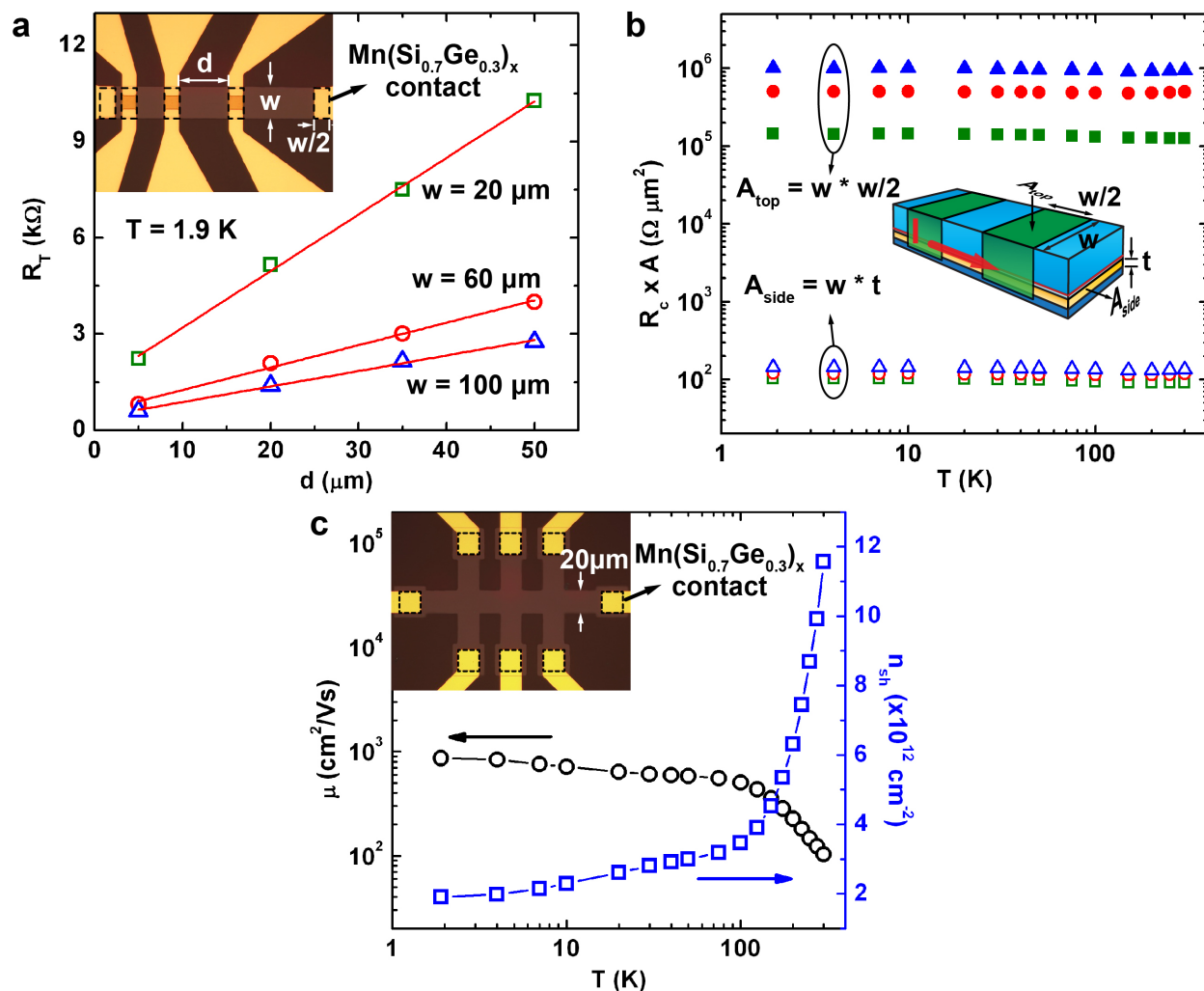


**Figure 4-7.** TLM and Hall measurements of the Si/SiGe MODQW. (a)  $R_T$  as a function of  $d$ . They are measured between every two adjacent Mn(Si<sub>0.7</sub>Ge<sub>0.3</sub>)<sub>x</sub> contacts from three TLM devices with different channel widths of  $w = 20, 60, 100 \mu\text{m}$  (green squares, red circles, and blue triangles). (b) Two series of the RA product as a function of temperature: the solid (empty) symbols utilize the  $A_{\text{top}}$  ( $A_{\text{side}}$ ) for calculation, respectively. (c) Temperature dependence of Hall mobility (left axis) and carrier density (right axis) measured from a Hall bar device.

## 4.7 Electrical Spin Injection, Transportation, and Detection in the Si 2DEG System

So far we have confirmed that (i) the  $T_c$  of the  $\text{Mn}(\text{Si}_{0.7}\text{Ge}_{0.3})_x$  contact is higher than 150 K, and the easy-axis is along the in-plane direction, (ii) the formation of  $\text{Mn}(\text{Si}_{0.7}\text{Ge}_{0.3})_x$  yields a sharp Schottky end contact to the 2DEG, and (iii) a high-mobility 2DEG is formed in the Si/SiGe MODQW. It should be noted that, compared to the high mobility of  $1200 \text{ cm}^2/\text{V}\cdot\text{s}$  in the 2DEG channel, the mobility in parasitic channel is much lower ( $49 \text{ cm}^2/\text{V}\cdot\text{s}$ ). Spin polarization in the parasitic channel could be significantly randomized by the high-density ionized impurity charges before reaching the contact 4, so its contribution to the spin detection signal could be neglected.

**Figure 4-8(a)** shows the setup for nonlocal measurements,<sup>25,31</sup> aiming to build up spin accumulation under the contact 3 and therefore generate spin diffusion current towards the contact 4. In this way, the spin transport in 2DEG could be detected by the relative magnetization orientations of the contact 3 and 4 while sweeping in-plane magnetic field. However, only a small resistance change ( $\Delta R_{NL} = 60 \text{ n}\Omega$ ) and coercive field ( $H_c = 500 \text{ Oe}$ ) are observed, as shown in **Figure 4-8(b)**, which could not provide a clear evidence as well as a detailed physical analysis. On the other hand, the MR of the FM/2DEG/FM spin valve could also be measured using the four-terminals setup shown in **Figure 4-8(c)**, and it is used to demonstrate the spin injection and transport<sup>2,106</sup> in the 2DEG. **Figure 4-8(d)** shows the MR curves of the FM/2DEG/FM spin valve with a channel length of  $L_{ch} = 1.5 \text{ }\mu\text{m}$  at 1.9 K. In the experiment, an AC modulation current ( $I_{25} = 1 \text{ }\mu\text{A}$ ) superimposing on a DC bias current ( $-13 \text{ }\mu\text{A}$ ) was applied through the FM/2DEG/FM spin valve, and an AC response ( $V_{34}$ ) voltage was measured by a

lock-in amplifier while sweeping the magnetic field along the in-plane direction ( $H_Y$ ). The fine peak around zero field ( $H_Y$ ) is due to hyperfine interaction with nuclear spins.<sup>107,108</sup> It is important to see that the symmetric resistance steps were clearly observed at the coercive fields of  $\pm \sim 300$  Oe. They are not only the typical characteristics of the spin valve switching between a parallel and an antiparallel configuration,<sup>106,109</sup> but also a strong evidence of the successful spin injection, transport, and detection in the 2DEG.

It is interesting to compare the local and nonlocal MR curves in **Figures 4-8 (b) and (d)** that they show similar coercive fields at  $\pm 300$ -500 Oe, which suggests that the spin injection/detection efficiency is improved by the applied field in the local setup. Although both curves indicate the switching behavior of the magnetization configuration, only the local MR curves give rise to the sharp resistance states between parallel and antiparallel configuration. The energy band diagram in **Figure 4-9** could probably explain the effect of the applied field. In our devices, the Si 2DEG channel is not continuous under the FM contacts, and a  $\text{Mn}(\text{SiGe})_x/\text{Si}/\text{Mn}(\text{SiGe})_x$  heterostructure is formed between contact 3 and 4 along the lateral direction, so that there are narrow Schottky barriers at the  $\text{Mn}(\text{SiGe})_x/\text{Si}$  interface, which blocks electron diffusion while the  $\text{Mn}(\text{Si}_{0.7}\text{Ge}_{0.3})_x/\text{Si}/\text{Mn}(\text{Si}_{0.7}\text{Ge}_{0.3})_x$  heterostructure is under zero bias voltage (nonlocal setup). Therefore, the applied  $\mathcal{E}$ -field in local setup causes band bending and helps spin polarized electrons tunnel through the barrier.

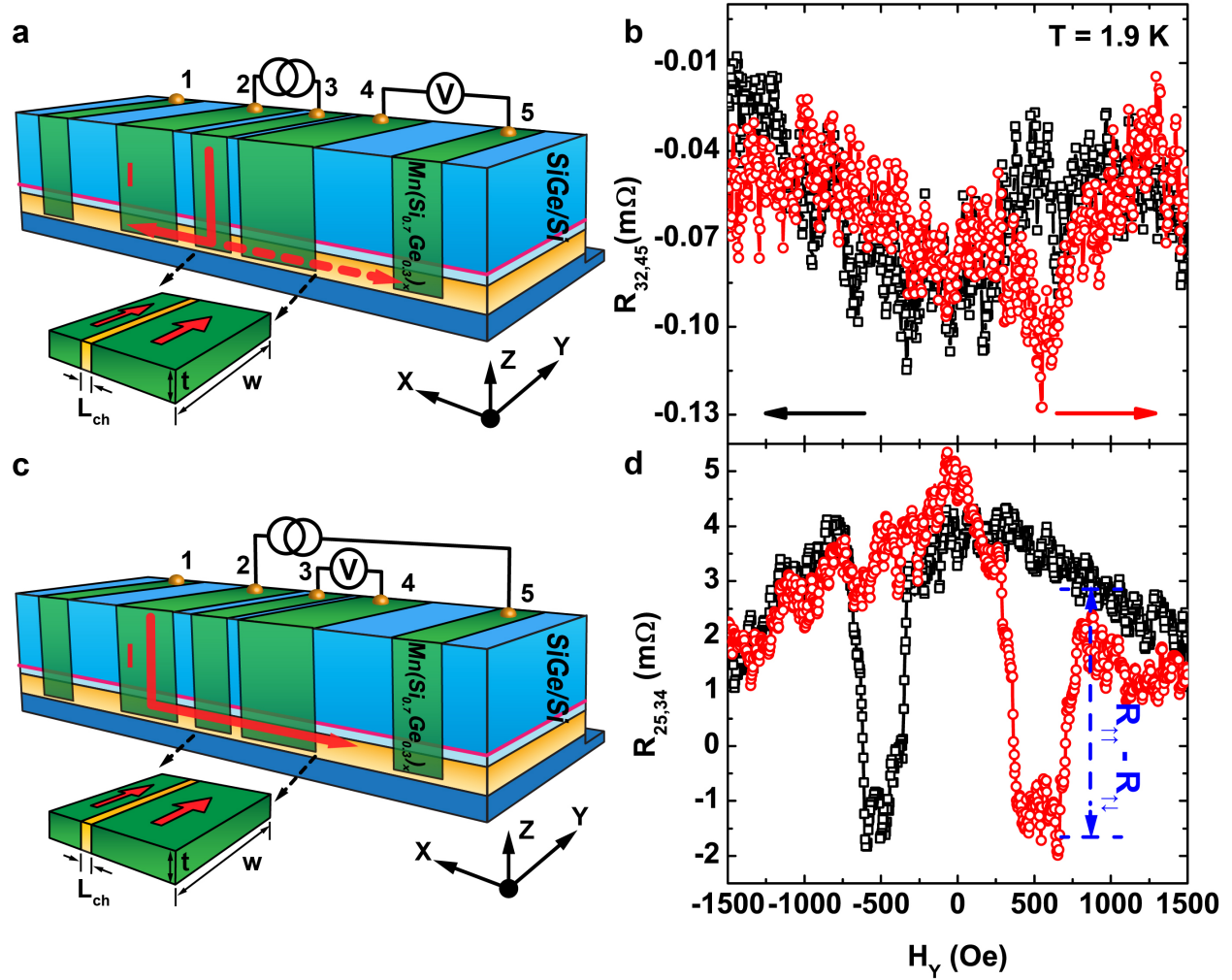


**Figure 4-8.** Nonlocal and local FM/2DEG/FM spin valve measurements. (a) The setup for the nonlocal measurements ( $R_{NL} = R_{32,45} \equiv V_{45}/I_{32}$ ). (b) The nonlocal MR curves of the FM/2DEG/FM spin valve with a channel length of  $L_{ch} = 1.5 \mu\text{m}$  at 1.9 K. (c) The setup for the four-terminal measurements ( $R_{4T} = R_{25,34} \equiv V_{34}/I_{25}$ ). (d) The four-terminal MR curves of the FM/2DEG/FM spin valve with a channel length of  $L_{ch} = 1.5 \mu\text{m}$  at 1.9 K. The background signals of both MR curves are subtracted from the raw data, and the black and red arrows indicate the backward and forward sweeping directions of magnetic field between -1500 and

1500 Oe. Particularly for the four-terminal MR curves, the blue arrow shows the spin-dependent resistance ( $R_{\uparrow\uparrow} - R_{\uparrow\downarrow}$ ) between the parallel and antiparallel configurations of the FM/2DEG/FM spin valve.

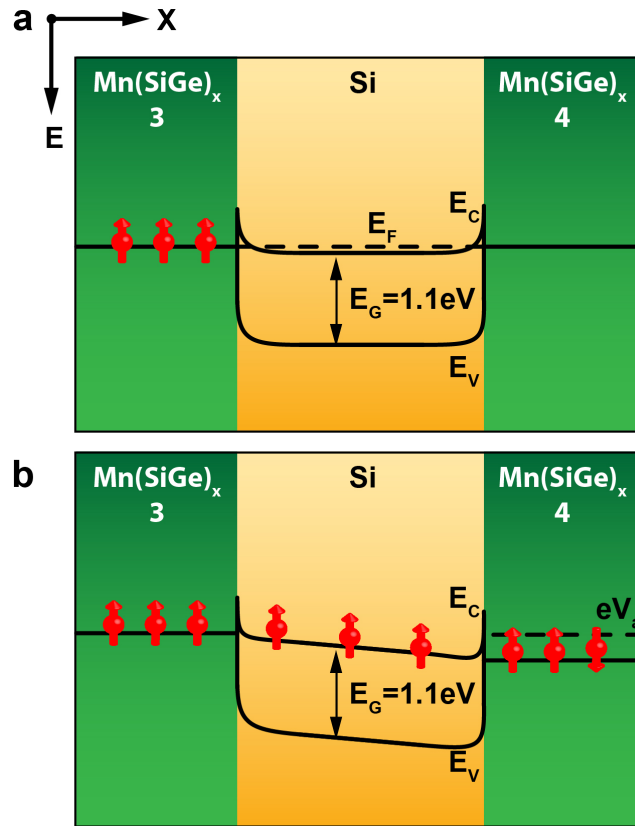


**Figure 4-9.** Energy band diagrams of the FM/2DEG/FM spin valve with (a) nonlocal and (b) four-terminal setups.

In the meanwhile, the spin-dependent resistances are extracted from three devices under the same bias condition at 1.9 K (see **Fig. 4-10(a)**). Because of spin relaxation in the 2DEG, the amplitude of the spin-dependent resistance ( $R_{\uparrow\uparrow} - R_{\uparrow\downarrow}$ ) exponentially decays as the electrode spacing increases from  $L_{ch} = 1.5$  to  $3.5 \mu\text{m}$ , as shown in **Fig. 4-11**. Last, **Fig. 4-10(b)** shows that the spin dependent resistance is observable up to  $T = 10$  K from the device with  $L_{ch} = 1.5 \mu\text{m}$ . Combining the MR of the FM/2DEG/FM spin valve as a function of channel length and temperature, we could rule out the concern of suspicious effects,<sup>35</sup> including local Hall effect and anomalous MR from the FM electrodes. If the spin-dependent resistance is due to the anomalous MR of a single FM electrode, its amplitude should not exponentially decays with the increased channel length, and the spin-dependent resistance should be observable to  $T > 10$  K, considering the  $T_c$  of the  $\text{Mn}(\text{Si}_{0.7}\text{Ge}_{0.3})_x$  contact is higher than 150 K.

To quantitatively estimate the spin diffusion length from the channel length-dependent MR data, we take into account the spin relaxation and modify the Julliere's model for the FM/2DEG/FM spin valve as follows:<sup>106,110</sup>  $R_{\uparrow\uparrow} - R_{\uparrow\downarrow} \propto 2P_{inj}P_{det}e^{-L_{ch}/l_{sf}}$ , where  $P_{inj}$  and  $P_{det}$  are the spin polarization of the FM electrodes, defined as  $P = (N_{\uparrow} - N_{\downarrow}) / (N_{\uparrow} + N_{\downarrow})$ , in which  $N_{\uparrow}$  ( $N_{\downarrow}$ ) are the DOS at the Fermi levels for the majority (minority) spins, respectively. The slope of a linear fitting in Fig. 4b yields a spin diffusion length of  $l_{sf} = 4.5 \mu\text{m}$  in 2DEG at 1.9 K. In addition, the spin lifetime can be estimated by  $\tau_s = l_{sf}^2 / D$ . We calculated the diffusion coefficient ( $D$ ) for a degenerate semiconductor particularly at low temperature using Eq. (3), which is different from the simplified Einstein relation ( $D/\mu = kT/q$ ) because only the electrons



having energies close to the Fermi level contribute to the conduction current at low temperature:<sup>8,111</sup>

$$D = \frac{1}{2} v_f^2 \tau_m = \frac{1}{2} \left( \frac{\hbar \sqrt{2\pi n_s}}{m^*} \right)^2 \frac{m^* \mu}{e} = 13 \text{ cm}^2/\text{s} \quad (4-4)$$

in which  $v_f = \hbar \sqrt{2\pi n_s} / m^*$  is the Fermi velocity,  $\tau_m = m^* \mu / e$  is the momentum relaxation time,  $m^* = 0.22 \times 9.11 \times 10^{-31} \text{ kg}$  is the effective electron mass in Si,  $n_s = n_1 = 9.6 \times 10^{11} \text{ cm}^{-2}$  is the sheet electron density in the 2DEG, and  $\mu = \mu_1 = 1200 \text{ cm}^2/\text{V} \cdot \text{s}$  is the electron mobility in the 2DEG. As a result, the corresponding spin lifetime at 1.9 K is estimated to be  $\tau_s = l_{sf}^2 / D = 16 \text{ ns}$ .

Comparing to Erve's work<sup>88</sup> using graphene as a tunnel barriers for spin injection into Si, in which the extracted spin lifetime is  $\tau_s \approx 0.2 \text{ ns}$  in Si ( $N_d = 1 \times 10^{19} \text{ cm}^{-3}$ ) at 4 K, the significant improvement of  $\tau_s = 16 \text{ ns}$  in the Si/SiGe MODQW at 1.9 K is mainly due to the spin transport in a high-mobility 2DEG channel, where the impurity density is as low as  $N_d \approx 1 \times 10^{14} \text{ cm}^{-3}$ . Our results are consistent with the fact that spin lifetime is strongly dependent on the impurity density.<sup>31,88,112</sup> In the experiments, it is usually difficult to achieve spin transport in Si with such a low impurity concentration because a heavily doped surface layer is typically required to form a narrow depletion width for optimized contact resistance,<sup>2,34</sup> which on the other hand could cause serious carrier scattering and spin relaxation. On the contrary, in our case the impurities are separated from the channel by a spacer layer in the Si/SiGe MODQW structures, which have the uniqueness to preserve a high carrier density but a low impurity density at the same time.

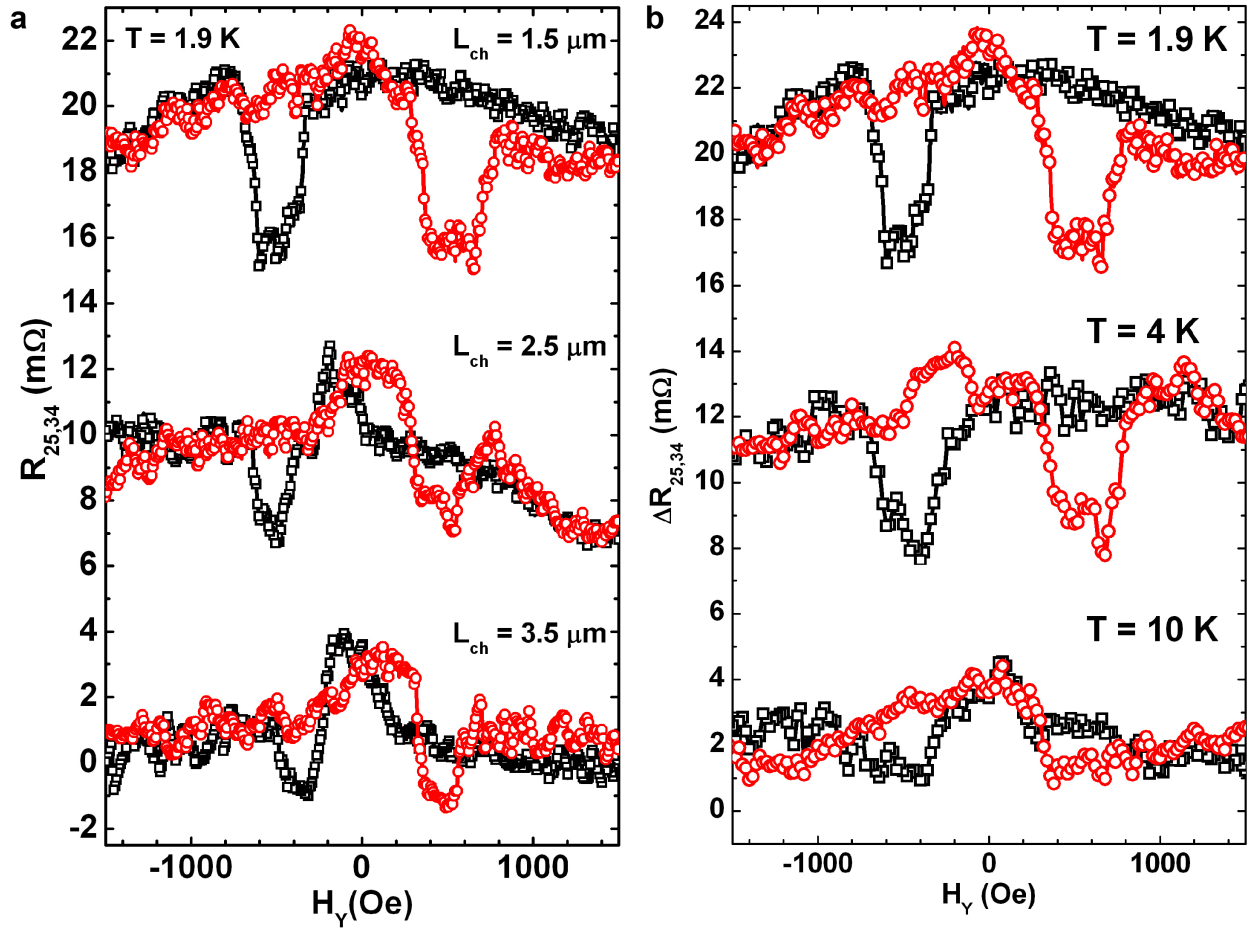


**Figure 4-10.** MR curves of the FM/2DEG/FM spin valves. (a) MR curves of three FM/2DEG/FM spin valves with different channel lengths ( $L_{ch} = 1.5, 2.5,$  and  $3.5 \mu\text{m}$ ) at  $1.9$  K. Even though the FM electrodes are designed to be the same size, the coercive fields for different devices could be slightly different from each other's.<sup>27</sup> The spin-dependent resistances of three devices are summarized in Figure 4-15 to extract the spin diffusion length. (b) MR curves of the FM/2DEG/FM spin valves with  $L_{ch} = 1.5 \mu\text{m}$  at different temperatures from  $1.9$  to  $10$  K. All the MR curves are intentionally offset for clarity.

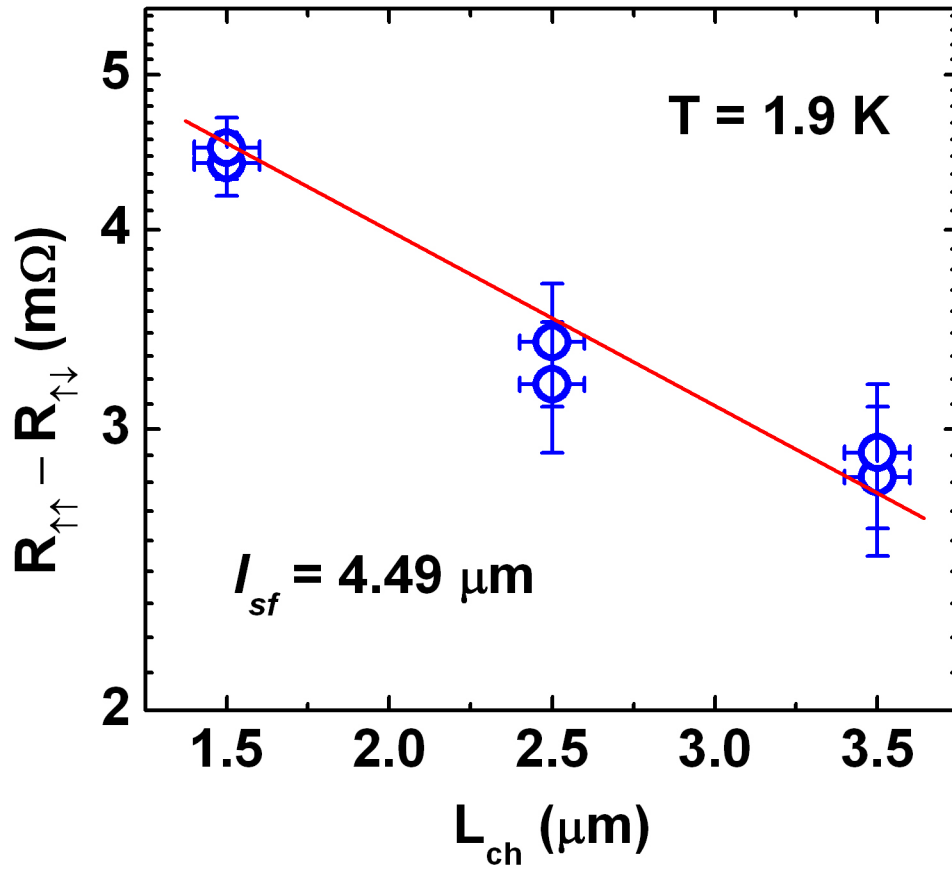


**Figure 4-11.** The spin-dependent resistance as a function of channel length at 1.9 K. The linear fitting yields a spin diffusion length of  $l_{sf} = 4.49 \mu\text{m}$  in the 2DEG channel at 1.9 K.

# Chapter 5 Summary

## 5.1 Conclusion

In conclusion, we have demonstrated electrical spin injection and transport in the 2DEG using FM/2DEG/FM structure, particularly for the first time in a Si/SiGe MODQW system. Being different from the traditional approaches, we developed high-quality  $\text{Mn}(\text{Si}_{0.7}\text{Ge}_{0.3})_x$  end contact to the buried 2DEG in a Si/SiGe MODQW using CMOS-compatible processes. In addition, we extracted the spin diffusion length and lifetime  $l_{sf} = 4.5 \mu\text{m}$  and  $\tau_s = 16 \text{ ns}$  at 1.9 K, respectively. In the future, the use of the high-mobility channel and the functionality of heterostructure systems for room-temperature applications will probably require further efforts to improve the material quality of the Si/SiGe MODQW: the Curie temperature of  $\text{Mn}(\text{Si}_{0.7}\text{Ge}_{0.3})_x$  could be further raised up by carbon-doping;<sup>71-73</sup> the SiGe spacer layer thickness and the Sb  $\delta$ -doping level could be further optimized to increase the mobility;<sup>94,113,114</sup> the implementation of front and back gating holds great potential for device application to effectively tune the wave functions in the MODQW.<sup>115</sup> Our findings in the Si/SiGe MODQW may spur further work on semiconductor-based heterostructures that integrate high-mobility channel with magnetic contacts, and may potentially lead to the innovation of novel spintronics devices.

## 5.2 Outlook

Only recently, we demonstrate the electrical detection of spin transport in Si 2DEG systems using FM Mn-germanosilicide ( $\text{Mn}(\text{Si}_{0.7}\text{Ge}_{0.3})_x$ ) side contacts,<sup>116</sup> which is the first report of spin transport in the 2DEG confined in a Si/SiGe modulation doped quantum well structure (MODQW). To make continuous progress of Si-based spintronics, the next step is to built up a logic device by integrating a 2DEG channel and five FM  $\text{Mn}(\text{Si}_{0.7}\text{Ge}_{0.3})_x$  contacts within the scale of spin diffusion length,<sup>46</sup> as shown in **Figure 5-1(a)**. We propose a different approach using a spin accumulation as the basis for a semiconductor logic device to realize the NAND(X,Y) operation, as schematically illustrated in **Figure 5-1(b)** and **(c)**. By connecting two spin valves with a common source terminal M, we create a system that is capable of amplifying the current of each spin valve.<sup>117</sup>

The motivation to achieve transformative improvements over previous work is to invoke the following four unique innovative features: (1) the use of a high-mobility Si 2DEG channel as interconnects between five FM contact for spin-dependent information processing; (2) high-quality  $\text{Mn}(\text{Si}_{0.7}\text{Ge}_{0.3})_x/2\text{DEG}$  contact with atomically clean interfaces to achieve effective spin injection/detection; (3) information stored as the magnetization orientations to ensure nonvolatile storage; (4) the use of spin polarization(collective spins) as a single identity to achieve low power dissipation. The proposed activity will bring in-depth understanding of the physics of spin transport in a Si 2DEG channel and the superimposition of spin accumulation.

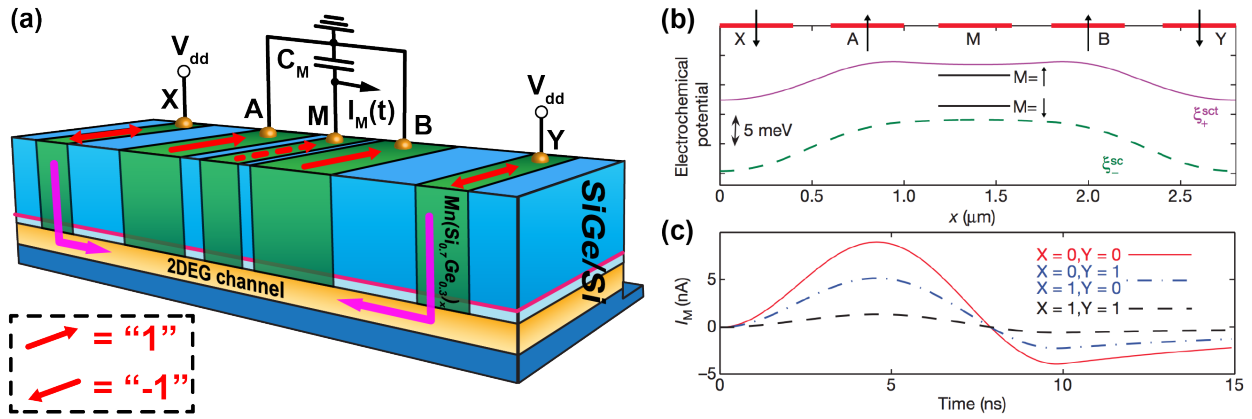


**Figure 5-1.** Proposal of Si 2DEG-based spin logic device. (a) Schematic illustration of the proposed Si 2DEG-based nonvolatile spin logic device. The red arrows indicate the magnetization orientation of each FM contact. The output is given by a transient current response,  $I_M(t)$ , caused by an in-plan rotation of M magnetization. The amplitude of  $I_M(t)$  is proportional to the spin accumulation in the 2DEG channel. (b) Typical steady state profiles of the spin-dependent chemical potential inside the Si 2DEG channel.<sup>46</sup> (c) Simulated transient currents ( $I_M$ ) in the M terminal induced by a 10-ns rotation of M magnetization.<sup>46</sup> The operands of the NAND(X,Y) are the magnetization directions of the contacts labeled by A, B, X, and Y.

# Appendices

## Appendix A. PPMS System Status Table

Description of General System Status Measure Code		
Bits	Value	Status, Temperature
0-3	0	Status unknown
	1	Normal stability at target temperature
	2	Stable
	5	Within tolerance, waiting for equilibrium
	6	Temperature not in tolerance, not valid
	7	Filling/Emptying reservoir
	10	Standby mode invoked
	13	Temperature control disabled
	14	Request cannot complete, impedance not functioning
	15	General failure in temperature system
Bits	Value	Status, Magnet
4-7	0	Status unknown
	1	Persistent mode, stable
	2	Persist switch warming
	3	Persist switch cooling
	4	Driven mode, stable at final field
	5	Driven mode, final approach

	6	Charging magnet at specified voltage
	7	Discharging magnet
	8	Current error, incorrect current in magnet
	15	General failure in magnet control system
<b>Bits</b>	<b>Value</b>	<b>Status, Chamber</b>
8-11	0	Status unknown
	1	Purged and sealed
	2	Vented and sealed
	3	Sealed, condition unknown
	4	Performing purge/seal routine
	5	Performing vent/seal sequence
	8	Pumping continuously
	9	Flooding continuously
	15	General failure in gas control system
<b>Bits</b>	<b>Value</b>	<b>Status, Sample Position</b>
12-15	0	Status unknown
	1	Sample stopped at target value
	5	Sample moving toward set point
	8	Sample hit limit switch
	9	Sample hit index switch
	15	General failure



## Appendix B. Fe/MgO/ $n^+$ -Ge Device Fabrication Process

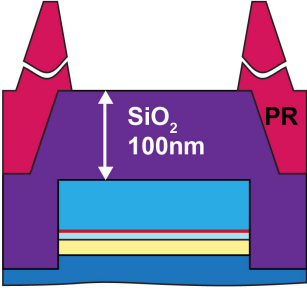
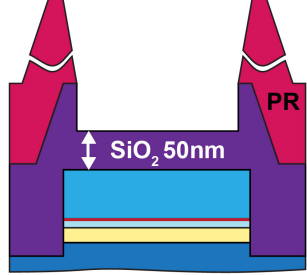
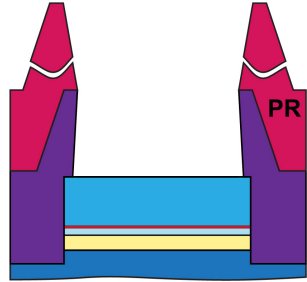
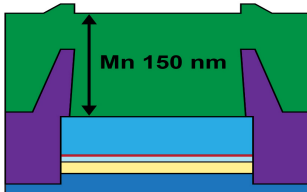
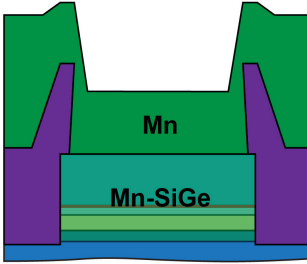
To fabricate the spin injection devices, an unintentionally doped Ge wafer ( $n \sim 10^{14} \text{ cm}^{-3}$ ) was used as a starting substrate. Low-temperature solid-source molecular beam epitaxy (MBE)<sup>118</sup> was used to grow a lightly doped ( $n = 1 \times 10^{16} \text{ cm}^{-3}$ ) Ge layer (300 nm thick), followed by a transition layer (15 nm thick) and then a degenerately doped ( $n = 2 \times 10^{19} \text{ cm}^{-3}$ ) surface layer (15 nm thick). For 3T devices, the MgO (1 nm) and Fe (20 nm) films were subsequently grown on Ge and capped by a 20 nm Al layer<sup>52</sup> in another MBE chamber. The electrodes were patterned with photolithography, followed by reactive ion etching and wet chemical etching. Ti/Au (10/100 nm) bonding pads were fabricated by electron beam evaporation and lift-off process. Finally, as the back contact, silver epoxy was applied to the backside of the whole wafer. A standard lock-in technique was used for spin injection measurements. For the 4T device, the doping profile of the Ge wafer is the same as in the 3T device, and the device structure is similar to the previous spin valve structure.<sup>30</sup> Briefly, a Ge channel was first defined by reactive ion etching with a mesa height of 60 nm. Then four electrodes were fabricated with standard e-beam lithography and lift-off process, where the outer two non-ferromagnetic electrodes (E1 and E4) were made of Au/Ti, and the inner two spin-dependent electrodes (E2 and E3) were made of MgO (1 nm) and Fe (100 nm) grown by MBE.<sup>52</sup> **Figure 3-1(d)** is the schematic diagram of the device structure and nonlocal measurements scheme.

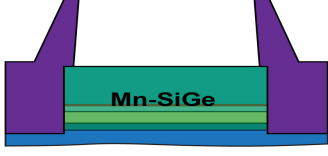
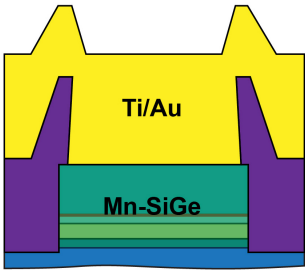
## Appendix C. $\text{Mn}_5\text{Ge}_3\text{C}_{0.8}/\text{Al}_2\text{O}_3/n^+$ -Ge Device Fabrication Process

Doped semiconductor layers were grown by solid-source molecular beam epitaxy (MBE). First, a Ge virtual substrate with a thickness of 50 nm was deposited on a Si (111) substrate. It accommodates the lattice mismatch between the Si substrate and the final Ge layer, and thus enables the subsequent growth of high-quality Ge layers. This was followed by the growth of a 300 nm  $n$ -Ge buffer layer with  $N_D = 1 \times 10^{18} \text{ cm}^{-3}$ . Finally, a thin layer (40 nm) of degenerately doped  $n^+$ -Ge ( $N_D = 1 \times 10^{20} \text{ cm}^{-3}$ ) was deposited as highly conductive channel layer. The device fabrication process started with structuring of the mesa by reactive ion etching (RIE). A  $\text{SiO}_2$  layer (100 nm) was deposited by plasma-enhanced chemical vapor deposition (PECVD) to passivate the surface. Contact holes (size  $98 \times 198 \mu\text{m}^2$ ) were defined by photolithography and structured by RIE as well as wet chemical etching. Prior to the deposition of  $\text{Mn}_5\text{Ge}_3\text{C}_{0.8}$ , a thin  $\text{Al}_2\text{O}_3$  layer (2 nm) was deposited by plasma-enhanced atomic layer deposition (PE-ALD) in order to prevent material intermixing. The 40 nm  $\text{Mn}_5\text{Ge}_3\text{C}_{0.8}$  contacts were deposited by simultaneous DC- and RF-magnetron sputtering from elemental targets of Mn, Ge, and C in a high-vacuum system under Ar atmosphere at a substrate temperature  $T_s = 400 \text{ }^\circ\text{C}$ . The  $\text{Mn}_5\text{Ge}_3\text{C}_{0.8}$  films were capped *in-situ* with 40 nm of Al at  $T_s = 40 \text{ }^\circ\text{C}$ . After a 5 s dip in buffered hydrofluoric acid (BHF), another 300-400 nm of Al were then deposited *ex-situ* by thermal evaporation as the final metallization layer. The Al/ $\text{Mn}_5\text{Ge}_3\text{C}_{0.8}$ -metallization was patterned by photolithography and structured in one etching step. A reference sample without the ferromagnetic  $\text{Mn}_5\text{Ge}_3\text{C}_{0.8}$  layer was also fabricated.

**Appendix D. Mn(Si<sub>0.7</sub>Ge<sub>0.3</sub>)<sub>x</sub> Device Fabrication Process**

STEPS	STRUCTURE	INSTRUCTION
1. Sample Clean	<p><b>Sb δ-doping (1/20 ML)</b></p>	<p>1-1. Acetone, ultrasonic, 5 min                      1-2. Methanol, ultrasonic, 5 min                      1-3. IPA, ultrasonic, 5 min</p>
2. 1 <sup>st</sup> PL: Mesa		<p>2-1. HMDS, 5 min                      2-2. Spin coating 5000 rpm, 30 sec                      2-3. Remove thick PR on four corners                      2-4. Soft bake, 100 C, 1 min (2<sup>nd</sup> 135 C)                      2-5. UV expose 8 sec, VAC-CONT                      2-6. Developer: AZ400K (1:4), 20-25 sec</p>
3. Mesa Etching		<p>3-1. Recipe: AOE, LJYDBOX, ~100 sec                      3-2. Check mesa height by profiler  <b>NOTE:</b></p> <ul style="list-style-type: none"> <li>• Prepare dummy samples around real devices to check etching rate</li> <li>• Si etching rate: 1-2 nm/sec</li> <li>• Make sure T<sub>sub</sub> &lt; 100 C</li> </ul>
4. Remove Residual	<p><b>O<sub>2</sub> plasma</b></p>	<p>4-1. Acetone, ultrasonic, 5 min                      4-2. Stripper (AZ300T), 80 °C, 30 min                      4-3. O<sub>2</sub> plasma (TEGAL Asher), 200 W, 5 min                      4-4. Perform clean process before PECVD  <b>NOTE: Check PR residual with SEM/AFM</b></p>
5. PECVD Growth		<p>5-1. Recipe: STS-PECVD, LFSIOST (low freq. SiO<sub>2</sub>), 3 min                      5-2. Check SiO<sub>2</sub> thickness using Nanospec (The color should be navy blue for 100nm SiO<sub>2</sub>)  <b>NOTE:</b></p> <ul style="list-style-type: none"> <li>• Refractive index, SiO<sub>2</sub> = 1.54427</li> <li>• Prepare dummy samples to check initial growth rate</li> </ul>

<p>6. 2<sup>nd</sup> PL: Active Contact Hole</p>		<p>6-1. IPA, ultrasonic, 5 min 6-2. HMDS, 5 min 6-3. Spin coating 5000 rpm, 30 sec 6-4. Remove thick PR on four corners 6-4. Soft bake, 100 C, 1 min (2<sup>nd</sup> 135C) 6-5. UV expose 8 sec, VAC-CONT 6-6. Developer: AZ400K (1:4), 10-15 sec <b>NOTE: MR_2-3um pattern are very sensitive to developer concentration and developing time.</b></p>								
<p>7. Dry Etching (STS-AOE)</p>		<p>7-1. Recipe: AOE, LJYDBOX, 25 sec 7-2. Check SiO<sub>2</sub> thickness with NanoSpec (color should be graphite for 40-50nm SiO<sub>2</sub>) <b>NOTE:</b></p> <ul style="list-style-type: none"> <li>Etching rate is not linear</li> </ul> <table border="1" data-bbox="857 747 1360 856"> <thead> <tr> <th>Time (sec)</th> <th>10</th> <th>20</th> <th>25</th> </tr> </thead> <tbody> <tr> <td>Etching depth (nm)</td> <td>6</td> <td>41</td> <td>68</td> </tr> </tbody> </table>	Time (sec)	10	20	25	Etching depth (nm)	6	41	68
Time (sec)	10	20	25							
Etching depth (nm)	6	41	68							
<p>8. Wet Etching (BOE)</p>		<p>8-1. Dip in BOE 30 sec <b>NOTE:</b> <b>BOE etching rate: 26.5 nm/10 sec</b> <b>Check SiO<sub>2</sub> residual by SEM/AFM</b></p> <p>Remove PR: 8-2. Acetone, ultrasonic, 5 min 8-3. IPA, ultrasonic, 5 min 8-4. BOE, 5 sec</p>								
<p>9. Metal Deposition</p>		<p>9-1. Deposit Mn for 150 nm process #: 35 Mn pocket: 4 <b>NOTE:</b> <b>Dip in BOE for 5 sec right before metal deposition.</b></p>								
<p>10. RTP Process</p>		<p>10-1. Anneal 400 C for 2 min <b>NOTE:</b></p> <ul style="list-style-type: none"> <li>Anneal sample right after metal deposition to minimize oxidation.</li> <li>Keep backside clean before annealing to improve thermal conducting.</li> <li>Keep T<sub>TC</sub> ~ 65 C before every run</li> <li>Factor setup: 1(1.0), 2(1.4), 3(0.3), 4(0.3), 5(1.4)</li> </ul>								

<p>11. Remove Leftover Mn</p>		<p>11-1 Dip in Al etchant @ 80 C for 1 min</p>
<p>12. Final PL and Metal Deposition</p>		<p>12-1. IPA, ultrasonic, 5 min  12-2. HMDS, 5 min  12-3. Spin coating 4000 rpm, 30 sec  12-4. Remove thick PR on four corners  12-4. Soft bake, 100 C, 1 min (2<sup>nd</sup> 135C)  12-5. UV expose 8 sec, VAC-CONT  12-6. Developer: AZ400K (1:4), 10-15 sec  12-7, O<sub>2</sub> plasma (TEGAL Asher), 200 W, 5 min  12-8, BOE dip for 5 sec before deposition  12-9, Deposit Ti/Au for 50/100 nm</p>

## References

- 1 Zutic, I., Fabian, J. & Das Sarma, S. Spintronics: Fundamentals and applications. *Reviews of Modern Physics* **76**, 323 (2004).
- 2 Schmidt, G. & Molenkamp, L. W. Spin injection into semiconductors, physics and experiments. *Semiconductor Science and Technology* **17**, 310 (2002).
- 3 Datta, S. & Das, B. Electronic analog of the electro-optic modulator. *Applied Physics Letters* **56**, 665 (1990).
- 4 Koo, H. C. *et al.* Control of Spin Precession in a Spin-Injected Field Effect Transistor. *Science* **325**, 1515 (2009).
- 5 Li, P. & Dery, H. Tunable spin junction. *Applied Physics Letters* **94**, 192108 (2009).
- 6 Jansen, R., Min, B.-C. & Dash, S. P. Oscillatory spin-polarized tunnelling from silicon quantum wells controlled by electric field. *Nat Mater* **9**, 133 (2009).
- 7 Hammar, P. R. & Johnson, M. Detection of Spin-Polarized Electrons Injected into a Two-Dimensional Electron Gas. *Physical Review Letters* **88**, 066806 (2002).
- 8 Oltcher, M. *et al.* Electrical Spin Injection into High Mobility 2D Systems. *Physical Review Letters* **113**, 236602 (2014).
- 9 Zutic, I. & Fabian, J. Spintronics: Silicon twists. *Nature* **447**, 268 (2007).
- 10 Jansen, R. Silicon spintronics. *Nat Mater* **11**, 400 (2012).
- 11 Moore, G. E. Cramming more components onto integrated circuits. *Electronics* **38**, 8 (1965).
- 12 Hoyt, J. L. *et al.* in *Electron Devices Meeting, 2002. IEDM '02. International.* 23.

- 13 Mistry, K. *et al.* in *Electron Devices Meeting, 2007. IEDM 2007. IEEE International*. 247.
- 14 Kingon, A. I., Maria, J.-P. & Streiffer, S. K. Alternative dielectrics to silicon dioxide for memory and logic devices. *Nature* **406**, 1032 (2000).
- 15 Gusev, E. P. *et al.* in *Electron Devices Meeting, 2001. IEDM '01. Technical Digest. International*. 20.21.21.
- 16 Xuejue, H. *et al.* in *Electron Devices Meeting, 1999. IEDM '99. Technical Digest. International*. 67.
- 17 Hisamoto, D. *et al.* FinFET-a self-aligned double-gate MOSFET scalable to 20 nm. *Electron Devices, IEEE Transactions on* **47**, 2320 (2000).
- 18 International Technology Roadmap for Semiconductors. (2013).
- 19 Wang, K. L., Alzate, J. G. & Amiri, P. K. Low-power non-volatile spintronic memory: STT-RAM and beyond. *Journal of Physics D: Applied Physics* **46**, 074003 (2013).
- 20 Johnson, M. & Silsbee, R. H. Interfacial charge-spin coupling: Injection and detection of spin magnetization in metals. *Physical Review Letters* **55**, 1790 (1985).
- 21 Johnson, M. & Silsbee, R. H. Spin-injection experiment. *Physical Review B* **37**, 5326 (1987).
- 22 Johnson, M. & Silsbee, R. H. Nonlocal resistance and magnetoresistance in bulk metals. *Physical Review B* **39**, 8169 (1989).
- 23 Johnson, M. Spin accumulation in gold films. *Physical Review Letters* **70**, 2142 (1993).
- 24 Zhu, H. J. *et al.* Room-Temperature Spin Injection from Fe into GaAs. *Physical Review Letters* **87**, 016601 (2001).

- 25 Lou, X. *et al.* Electrical detection of spin transport in lateral ferromagnet-semiconductor devices. *Nat Phys* **3**, 197 (2007).
- 26 Jonker, B. T., Kioseoglou, G., Hanbicki, A. T., Li, C. H. & Thompson, P. E. Electrical spin-injection into silicon from a ferromagnetic metal/tunnel barrier contact. *Nat Phys* **3**, 542 (2007).
- 27 van 't Erve, O. M. J. *et al.* Electrical injection and detection of spin-polarized carriers in silicon in a lateral transport geometry. *Applied Physics Letters* **91**, 212109 (2007).
- 28 Dash, S. P., Sharma, S., Patel, R. S., de Jong, M. P. & Jansen, R. Electrical creation of spin polarization in silicon at room temperature. *Nature* **462**, 491 (2009).
- 29 Sasaki, T. *et al.* Electrical Spin Injection into Silicon Using MgO Tunnel Barrier. *Applied Physics Express* **2**, 053003 (2009).
- 30 Zhou, Y. *et al.* Electrical spin injection and transport in germanium. *Physical Review B* **84**, 125323 (2011).
- 31 Chang, L. T. *et al.* Comparison of spin lifetimes in n-Ge characterized between three-terminal and four-terminal nonlocal Hanle measurements. *Semiconductor Science and Technology* **28**, 015018 (2013).
- 32 Fischer, I. A. *et al.* Hanle-effect measurements of spin injection from Mn<sub>5</sub>Ge<sub>3</sub>C<sub>0.8</sub>/Al<sub>2</sub>O<sub>3</sub>-contacts into degenerately doped Ge channels on Si. *Applied Physics Letters* **105**, 222408 (2014).
- 33 Schmidt, G., Ferrand, D., Molenkamp, L. W., Filip, A. T. & van Wees, B. J. Fundamental obstacle for electrical spin injection from a ferromagnetic metal into a diffusive semiconductor. *Physical Review B* **62**, R4790 (2000).



- 34 Fert, A., Jaffr, egrave & s, H. Conditions for efficient spin injection from a ferromagnetic metal into a semiconductor. *Physical Review B* **64**, 184420 (2001).
- 35 Filip, A. T. *et al.* Experimental search for the electrical spin injection in a semiconductor. *Physical Review B* **62**, 9996 (2000).
- 36 Bube, R. H. *Electronic Properties of Crystalline Solids*. (Academic Press Inc., 1974).
- 37 Singh, J. *Electronic and Optoelectronic Properties of Semiconductor Structures*. (Cambridge University Press, 2003).
- 38 O'Connor, D. J., Sexton, B. A. & Smart, R. S. C. *Surface Analysis Methods in Material Science*. (Springer-Verlag Berlin Heidelberg, 1992).
- 39 Schroder, D. K. *Semiconductor Material and Device Characterization*. 3rd edn, (John Wiley & Sons Inc, 2006).
- 40 Quantum, D. Interfacing LabVIEW Programs with PPMS, DynaCool, Versalab and MPMS 3 Systems. <http://www.qdusa.com/sitedocs/appNotes/general/1070-210.pdf> (2014).
- 41 Jedema, F. J., Heersche, H. B., Filip, A. T., Baselmans, J. J. A. & van Wees, B. J. Electrical detection of spin precession in a metallic mesoscopic spin valve. *Nature* **416**, 713 (2002).
- 42 Dash, S. P. *et al.* Spin precession and inverted Hanle effect in a semiconductor near a finite-roughness ferromagnetic interface. *Physical Review B* **84**, 054410 (2011).
- 43 Tran, M. *et al.* Enhancement of the Spin Accumulation at the Interface between a Spin-Polarized Tunnel Junction and a Semiconductor. *Physical Review Letters* **102**, 036601 (2009).

- 44 Sugahara, S. & Tanaka, M. A spin metal--oxide--semiconductor field-effect transistor using half-metallic-ferromagnet contacts for the source and drain. *Applied Physics Letters* **84**, 2307 (2004).
- 45 Fabian, J., Žutić, I. & Das Sarma, S. Magnetic bipolar transistor. *Applied Physics Letters* **84**, 85 (2004).
- 46 Dery, H., Dalal, P., Cywinski, L. & Sham, L. J. Spin-based logic in semiconductors for reconfigurable large-scale circuits. *Nature* **447**, 573 (2007).
- 47 Behin-Aein, B., Datta, D., Salahuddin, S. & Datta, S. Proposal for an all-spin logic device with built-in memory. *Nat Nano* **5**, 266 (2010).
- 48 Rojas-Sánchez, J. C. *et al.* Spin pumping and inverse spin Hall effect in germanium. *Physical Review B* **88**, 064403 (2013).
- 49 Dushenko, S. *et al.* Experimental Demonstration of Room-Temperature Spin Transport in n-Type Germanium Epilayers. *Physical Review Letters* **114**, 196602 (2015).
- 50 Sasaki, T. *et al.* Evidence of Electrical Spin Injection Into Silicon Using MgO Tunnel Barrier. *Magnetics, IEEE Transactions on* **46**, 1436 (2010).
- 51 Han, W. *et al.* Electrical detection of spin precession in single layer graphene spin valves with transparent contacts. *Applied Physics Letters* **94**, 222109 (2009).
- 52 Han, W. *et al.* Growth of single-crystalline, atomically smooth MgO films on Ge(001) by molecular beam epitaxy. *Journal of Crystal Growth* **312**, 44 (2009).
- 53 Han, W. *et al.* Electron-Hole Asymmetry of Spin Injection and Transport in Single-Layer Graphene. *Physical Review Letters* **102**, 137205 (2009).

- 54 Han, W. *et al.* Tunneling Spin Injection into Single Layer Graphene. *Physical Review Letters* **105**, 167202 (2010).
- 55 Han, W. & Kawakami, R. K. Spin Relaxation in Single-Layer and Bilayer Graphene. *Physical Review Letters* **107**, 047207 (2011).
- 56 Tran, M. *et al.* Erratum: Enhancement of the Spin Accumulation at the Interface between a Spin-Polarized Tunnel Junction and a Semiconductor [Phys. Rev. Lett. 102, 036601 (2009)]. *Physical Review Letters* **107**, 249901 (2011).
- 57 Li, C. H., van 't Erve, O. M. J. & Jonker, B. T. Electrical injection and detection of spin accumulation in silicon at 500 K with magnetic metal/silicon dioxide contacts. *Nat Commun* **2**, 245 (2011).
- 58 Fert, A., George, J. M., Jaffres, H. & Mattana, R. Semiconductors Between Spin-Polarized Sources and Drains. *Electron Devices, IEEE Transactions on* **54**, 921 (2007).
- 59 Parkin, S. S. P. *et al.* Giant tunnelling magnetoresistance at room temperature with MgO (100) tunnel barriers. *Nat Mater* **3**, 862 (2004).
- 60 Sasaki, T., Oikawa, T., Shiraishi, M., Suzuki, Y. & Noguchi, K. Comparison of spin signals in silicon between nonlocal four-terminal and three-terminal methods. *Applied Physics Letters* **98**, 012508 (2011).
- 61 Pershin, Y. V. & Privman, V. Focusing of Spin Polarization in Semiconductors by Inhomogeneous Doping. *Physical Review Letters* **90**, 256602 (2003).
- 62 Kameno, M. *et al.* Effect of spin drift on spin accumulation voltages in highly doped silicon. *Applied Physics Letters* **101**, 122413 (2012).

- 63 Jeon, K.-R. *et al.* Effect of spin relaxation rate on the interfacial spin depolarization in ferromagnet/oxide/semiconductor contacts. *Applied Physics Letters* **101**, 022401 (2012).
- 64 Li, J., Qing, L., Dery, H. & Appelbaum, I. Field-Induced Negative Differential Spin Lifetime in Silicon. *Physical Review Letters* **108**, 157201 (2012).
- 65 Debye, P. P. & Conwell, E. M. Electrical Properties of N-Type Germanium. *Physical Review* **93**, 693 (1954).
- 66 Lundstrom, M. *Fundamentals of carrier transport*. second edn, (Cambridge University Press, 2009).
- 67 Jeon, K.-R. *et al.* Electrical spin injection and accumulation in CoFe/MgO/Ge contacts at room temperature. *Physical Review B* **84**, 165315 (2011).
- 68 Kenji, K. *et al.* Greatly enhanced generation efficiency of pure spin currents in Ge using Heusler compound Co<sub>2</sub>FeSi electrodes. *Applied Physics Express* **7**, 033002 (2014).
- 69 Zeng, C. *et al.* Epitaxial ferromagnetic Mn<sub>5</sub>Ge<sub>3</sub> on Ge(111). *Applied Physics Letters* **83**, 5002 (2003).
- 70 Gajdzik, M., Sürgers, C., Kelemen, M. T. & Löhneysen, H. v. Strongly enhanced Curie temperature in carbon-doped Mn<sub>5</sub>Ge<sub>3</sub> films. *Journal of Magnetism and Magnetic Materials* **221**, 248 (2000).
- 71 Sürgers, C. *et al.* Magnetic order by C-ion implantation into Mn<sub>5</sub>Si<sub>3</sub> and Mn<sub>5</sub>Ge<sub>3</sub> and its lateral modification. *Applied Physics Letters* **93**, 062503 (2008).
- 72 Spiesser, A. *et al.* Control of magnetic properties of epitaxial Mn<sub>5</sub>Ge<sub>3</sub>C<sub>x</sub> films induced by carbon doping. *Physical Review B* **84**, 165203 (2011).

- 73 Fischer, I. A. *et al.* Ferromagnetic Mn 5 Ge 3 C 0.8 contacts on Ge: work function and specific contact resistivity. *Semiconductor Science and Technology* **28**, 125002 (2013).
- 74 Snider, G. 1D Poisson (PC version beta 8j1) <http://www3.nd.edu/~gsnider/> (2013).
- 75 Hu, Q. O., Garlid, E. S., Crowell, P. A. & Palmström, C. J. Spin accumulation near Fe/GaAs (001) interfaces: The role of semiconductor band structure. *Physical Review B* **84**, 085306 (2011).
- 76 Kioseoglou, G. *et al.* Electrical spin injection into Si: A comparison between Fe/Si Schottky and Fe/Al<sub>2</sub>O<sub>3</sub> tunnel contacts. *Applied Physics Letters* **94**, 122106 (2009).
- 77 Kun-Rok, J. *et al.* Unconventional Hanle effect in a highly ordered CoFe/MgO/ n -Si contact: non-monotonic bias and temperature dependence and sign inversion of the spin signal. *New Journal of Physics* **14**, 023014 (2012).
- 78 Fujita, Y. *et al.* Room-temperature sign reversed spin accumulation signals in silicon-based devices using an atomically smooth Fe<sub>3</sub>Si/Si(111) contact. *Journal of Applied Physics* **113**, 013916 (2013).
- 79 Dankert, A., Dulal, R. S. & Dash, S. P. Efficient Spin Injection into Silicon and the Role of the Schottky Barrier. *Sci. Rep.* **3**, 319 (2013).
- 80 Chantis, A. N. *et al.* Reversal of Spin Polarization in Fe/GaAs (001) Driven by Resonant Surface States: First-Principles Calculations. *Physical Review Letters* **99**, 196603 (2007).
- 81 Honda, S. *et al.* Spin polarization control through resonant states in an Fe/GaAs Schottky barrier. *Physical Review B* **78**, 245316 (2008).
- 82 Wada, E. *et al.* Inversion of Spin Photocurrent due to Resonant Transmission. *Physical Review Letters* **105**, 156601 (2010).

- 83 Dery, H. & Sham, L. J. Spin Extraction Theory and Its Relevance to Spintronics. *Physical Review Letters* **98**, 046602 (2007).
- 84 Jain, A. *et al.* Electrical spin injection and detection at Al<sub>2</sub>O<sub>3</sub>/n-journal article germanium interface using three terminal geometry. *Applied Physics Letters* **99**, 162102 (2011).
- 85 Iba, S. *et al.* Spin Accumulation and Spin Lifetime in p-Type Germanium at Room Temperature. *Applied Physics Express* **5**, 053004 (2012).
- 86 Zhou, Y., Ogawa, M., Han, X. & Wang, K. L. Alleviation of Fermi-level pinning effect on metal/germanium interface by insertion of an ultrathin aluminum oxide. *Applied Physics Letters* **93**, 202105 (2008).
- 87 Zhou, Y. *et al.* Engineering of tunnel junctions for prospective spin injection in germanium. *Applied Physics Letters* **94**, 242104 (2009).
- 88 van 't Erve, O. M. J. *et al.* Low-resistance spin injection into silicon using graphene tunnel barriers. *Nat Nano* **7**, 737 (2012).
- 89 Hanbicki, A. T., Jonker, B. T., Itskos, G., Kioseoglou, G. & Petrou, A. Efficient electrical spin injection from a magnetic metal/tunnel barrier contact into a semiconductor. *Applied Physics Letters* **80**, 1240 (2002).
- 90 Hanbicki, A. T. *et al.* Analysis of the transport process providing spin injection through an Fe/AlGaAs Schottky barrier. *Applied Physics Letters* **82**, 4092 (2003).
- 91 Kasahara, K. *et al.* Spin accumulation created electrically in an n-type germanium channel using Schottky tunnel contacts. *Journal of Applied Physics* **111**, 07C503 (2012).

- 92 Rashba, E. I. Theory of electrical spin injection: Tunnel contacts as a solution of the conductivity mismatch problem. *Physical Review B* **62**, R16267 (2000).
- 93 Carns, T. K., Zheng, X. & Wang, K. L. Enhancement of Si hole mobility in coupled delta-doped wells. *Applied Physics Letters* **62**, 3455 (1993).
- 94 Werner, J., Oehme, M., Kasper, E. & Schulze, J. Influence of the modulation doping to the mobility of two-dimensional electron gases in Si/SiGe. *Thin Solid Films* **518**, S234 (2010).
- 95 Schubert, E. F., Fischer, A. & Ploog, K. The delta-doped field-effect transistor (deltaFET). *Electron Devices, IEEE Transactions on* **33**, 625 (1986).
- 96 Friedrich, S. High-mobility Si and Ge structures. *Semiconductor Science and Technology* **12**, 1515 (1997).
- 97 Murarka, S. P. Silicide thin films and their applications in microelectronics. *Intermetallics* **3**, 173 (1995).
- 98 Tang, J. *et al.* Ferromagnetic Germanide in Ge Nanowire Transistors for Spintronics Application. *ACS Nano* **6**, 5710 (2012).
- 99 Spiesser, A. *et al.* Magnetic anisotropy in epitaxial Mn<sub>5</sub>Ge<sub>3</sub> films. *Physical Review B* **86**, 035211 (2012).
- 100 Lander, G. H., Brown, P. J. & Forsyth, J. B. The antiferromagnetic structure of Mn<sub>5</sub>Si<sub>3</sub>. *Proceedings of the Physical Society* **91**, 332 (1967).
- 101 Aronzon, B. A. *et al.* Room-temperature ferromagnetism and anomalous Hall effect in Si<sub>1-x</sub>Mn<sub>x</sub> (x~0.35) alloys. *Physical Review B* **84**, 075209 (2011).

- 102 Chiba, D. *et al.* Electrical control of the ferromagnetic phase transition in cobalt at room temperature. *Nat Mater* **10**, 853 (2011).
- 103 Chang, L.-T. *et al.* Electric-Field Control of Ferromagnetism in Mn-Doped ZnO Nanowires. *Nano Letters* **14**, 1823 (2014).
- 104 Ismail, K. *et al.* Identification of a Mobility-Limiting Scattering Mechanism in Modulation-Doped Si/SiGe Heterostructures. *Physical Review Letters* **73**, 3447 (1994).
- 105 Monroe, D., Xie, Y. H., Fitzgerald, E. A., Silverman, P. J. & Watson, G. P. Comparison of mobility-limiting mechanisms in high-mobility Si<sub>1-x</sub>Ge<sub>x</sub> heterostructures. *Papers from the 26th conference on the physics and chemistry of semiconductor interfaces* **11**, 1731 (1993).
- 106 Tang, J. *et al.* Electrical Spin Injection and Detection in Mn<sub>5</sub>Ge<sub>3</sub>/Ge/Mn<sub>5</sub>Ge<sub>3</sub> Nanowire Transistors. *Nano Letters* **13**, 4036 (2013).
- 107 Salis, G., Fuhrer, A. & Alvarado, S. F. Signatures of dynamically polarized nuclear spins in all-electrical lateral spin transport devices. *Physical Review B* **80**, 115332 (2009).
- 108 Chan, M. K. *et al.* Hyperfine interactions and spin transport in ferromagnet-semiconductor heterostructures. *Physical Review B* **80**, 161206 (2009).
- 109 Xiong, Z. H., Wu, D., Vally Vardeny, Z. & Shi, J. Giant magnetoresistance in organic spin-valves. *Nature* **427**, 821 (2004).
- 110 Julliere, M. Tunneling between ferromagnetic films. *Physics Letters A* **54**, 225 (1975).
- 111 Datta, S. *Electronic Transport in Mesoscopic Systems*. (Cambridge University Press, 1997).



- 112 Žutić, I., Fabian, J. & Erwin, S. C. Spin Injection and Detection in Silicon. *Physical Review Letters* **97**, 026602 (2006).
- 113 Stern, F. & Laux, S. E. Charge transfer and low-temperature electron mobility in a strained Si layer in relaxed Si<sub>1-x</sub>Ge<sub>x</sub>. *Applied Physics Letters* **61**, 1110 (1992).
- 114 Monroe, D., Xie, Y. H., Fitzgerald, E. A., Silverman, P. J. & Watson, G. P. Comparison of mobility-limiting mechanisms in high-mobility Si<sub>1-x</sub>Ge<sub>x</sub> heterostructures. *Papers from the 26th conference on the physics and chemistry of semiconductor interfaces* **11**, 1731 (1993).
- 115 Ismail, K., Arafa, M., Saenger, K. L., Chu, J. O. & Meyerson, B. S. Extremely high electron mobility in Si/SiGe modulation-doped heterostructures. *Applied Physics Letters* **66**, 1077 (1995).
- 116 Chang, L.-T. *et al.* Electrical detection of spin transport in Si two-dimensional electron gas systems. *in preparation* (2015).
- 117 Dery, H., Cywiński, Ł. & Sham, L. J. Spin transference and magnetoresistance amplification in a transistor. *Physical Review B* **73**, 161307 (2006).
- 118 Oehme, M., Werner, J. & Kasper, E. Molecular beam epitaxy of highly antimony doped germanium on silicon. *Journal of Crystal Growth* **310**, 4531 (2008).